UNIVERSITY OF SOUTHAMPTON

FACULTY OF PHYSICAL AND APPLIED SCIENCES

OPTOELECTRONICS RESEARCH CENTRE

Optical Cooling of Solids

and

Laguerre-Gaussian Mode Generation

by

Kristian Philip Thaller

A thesis submitted in partial fulfilment for the degree of Doctor of Philosophy

June 2011

UNIVERSITY OF SOUTHAMPTON

ABSTRACT

FACULTY OF PHYSICAL AND APPLIED SCIENCES
OPTOELECTRONICS RESEARCH CENTRE

Doctor of Philosophy

OPTICAL COOLING OF SOLIDS *AND* LAGUERRE-GAUSSIAN MODE GENERATION

by Kristian Philip Thaller

This thesis covers two areas of laser physics: optical cooling of rare-earth-doped solids by anti-Stokes fluorescence and the generation of pure Laguerre-Gaussian laser modes using a ring-shaped pump beam.

A novel laser-based approach to determining local variations in the temperature of transparent samples is developed. This technique is based on monitoring the frequency-shift of the axial modes of a simple, diode-pumped solid-state laser resonator in which the sample is placed. A theoretical resolution of <4.5mK is calculated for a perfectly isolated probe resonator. The technique is validated by comparison to thermocouple measurements of a control sample. The advantages of this diagnostic technique have been demonstrated for the discrimination of local optical cooling from parasitic heating effects. Local cooling of 1.4±0.1K has for the first time been observed in Yb^{3+}:CaF_2 using this measurement technique.

During the course of the optical cooling experiments regular pulse packets have been observed for sustained self-pulsing in a fibre laser operating significantly above the lasing threshold. This regular pulsing behaviour is observed to break down to irregular pulsing behaviour close to threshold. Extending the resonator length has been demonstrated as a technique for the suppression of self-pulsing.

A hollow-core-fibre beam-shaping technique has been developed to selectively generate pure Laguerre-Gaussian laser modes. An astigmatic mode-converter analysis of these modes has proven that an axial mode cannot simultaneously possess both senses of azimuthal phase. The sense of the azimuthal phase has been observed to flip around the peak of the gain spectrum.

Contents

List of Figures

Part 1 – Optical Cooling of Solids

Part 2 – Laguerre-Gaussian Mode Generation

List of Tables

Part 1 – Optical Cooling of Solids

Academic Thesis: Declaration Of Authorship

I, Kristian Philip Thaller, declare that this thesis and the work presented in it are my own and has been generated by me as the result of my own original research.

Optical Cooling of Solids and Laguerre-Gaussian Mode Generation

I confirm that:

1. This work was done wholly or mainly while in candidature for a research degree at this University;
2. Where any part of this thesis has previously been submitted for a degree or any other qualification at this University or any other institution, this has been clearly stated;
3. Where I have consulted the published work of others, this is always clearly attributed;
4. Where I have quoted from the work of others, the source is always given. With the exception of such quotations, this thesis is entirely my own work;
5. I have acknowledged all main sources of help;
6. Where the thesis is based on work done by myself jointly with others, I have made clear exactly what was done by others and what I have contributed myself.

Signed: ...……

Date: ...……

Acknowledgements

I would firstly like to thank my supervisor Prof. W. Andy Clarkson for his guidance, advice and ideas that were so important to me during this PhD. I would also like to thank Pu Wang, Ji Won Kim and Jacob Mackenzie for their support in the more practical aspects of this work.

My four years at the ORC have been a most enjoyable time and I would like to thank everyone – students, academic and support staff alike – who has contributed to my experience. I would particularly like to thank the other 'younger' members of the Advanced Solid State Sources group: Jaclyn, Lee, Mark, Rafał, Jae and Matt, both for their practical and moral support. Also worthy of a mention is Ruth, whose morning conversations over the ORC sink and supplies of freshly washed cups greased the wheels of lab work considerably.

I am very grateful to our technician Simon Butler whose advice and manufacturing skills have been plundered throughout this project.

I would also like to extend my gratitude to Prof. R. Moncorgé at the University of Caen for providing me with the Yb^{3+}:CaF_2 crystal that was used in the optical cooling experiments. I would further like to thank Jayanta Sahu and John Hayes at the ORC for their support in fabricating the non-standard optical fibres used in this research.

Finally I would like to thank EPSRC for funding this work.

Introduction

In the rapid generation of cryogenic gases, the delicate manipulation of biological molecules, vibrationless experiments and micromachining: science and engineering advance hand-in-hand, opening paths to new understanding and next generation technologies. This work is divided into two parts that apply laser physics in very different ways to make separate contributions to scientific knowledge and the future of technology.

Part 1 of this thesis covers optical (laser) cooling of rare-earth-doped solids by anti-Stokes fluorescence. This is the principle that a sample that is optically pumped above its mean fluorescence wavelength will radiate more energy than it absorbs, the difference coming from thermal lattice vibrations. The motivation for developing a novel temperature measurement technique to allow the spatial investigation of optical cooling in a crystal is explained. Existing research in the field of optical cooling is reviewed and the theory derived for the Yb^{3+}:YAG and Yb^{3+}:CaF_2 samples used in this work. To enable cooling experiments and open avenues of future research, a tuneable Yb-doped fibre laser was developed for operation at wavelengths below the 1.02μm mean fluorescence wavelength of Yb^{3+}:YAG. During this design process interesting self-pulsing features were observed. A method for the suppression of self-pulsing was validated. A novel laser-based temperature measurement technique enabling the identification of local cooling in solids was then developed. This employs a Fabry-Pérot interferometer to monitor a shift in the longitudinal modes of a bulk laser inside which is placed the sample. A theoretical resolution of <4.5mK is calculated for a perfectly isolated probe resonator. The usefulness of this approach was demonstrated with the first reported observation of local optical cooling by 0.15±0.05K from the initial temperature and 1.4±0.1K relative to the bulk sample temperature in an Yb^{3+}:CaF_2 sample. A spatial investigation of the optical cooling effect in this Yb^{3+}:CaF_2 crystal highlighted the

difficulties encountered when optically cooling solids and the advantages that the developed temperature measurement technique can offer were thus proven.

Part 2 of this thesis covers a novel beam-shaping technique for selective intracavity generation of pure Laguerre-Gaussian laser modes. Existing methods for generating Laguerre-Gaussian modes are reviewed. The theory is derived for controlling the overlap of a ring-shaped pump beam to select individual modes. The singularity at the centre of a Laguerre-Gaussian mode is due to a $2\pi l$ phase shift around the beam, where l is an integer describing the mode order. Thus the Poynting vector in a Laguerre-Gaussian beam spirals around the axis of propagation with either a left-handed or right-handed sense. This azimuthal 'sense of phase' was investigated for a generated LG_{01} mode by means of a purpose-built astigmatic mode-converter. It was observed in this work that the sense of phase was opposite on different sides of the gain spectrum.

This thesis ends with a brief conclusion that summarizes both aspects of this work. The combined contributions of the novel techniques for temperature measurement and Laguerre-Gaussian mode generation open new avenues of scientific research and technological development.

Part 1

Optical Cooling of Solids

Chapter 1

Introduction to Optical Cooling

Section 1.1 of this chapter discusses the motivation for studying optical cooling in rare-earth-doped solids and the reasons for developing a laser-based technique for temperature measurement along an arbitrary path within in a transparent sample are outlined. Section 1.2 summarizes the aims of Part 1 of this thesis and Section 1.3 outlines its structure. Section 1.4 reviews the historical background to optical cooling and recent advances in this field.

1.1 Motivation

Climate change is one of the greatest current threats to the survival of humanity. The damage to our ecosystem is being accelerated by ever increasing quantities of carbon dioxide that are released into the atmosphere, not least by slow and inefficient processes for producing and maintaining liquefied gases. Rapid optical cooling by anti-Stokes fluorescence (laser induced refrigeration) has recently allowed a decrease in temperature to 155K from ambient to be realized [1]. Reliable optical cryocoolers could reach cryogenic temperatures over short enough timescales to allow experimental set-ups and super-cooled devices to be shut down without wastage of the coolant fluid whenever they were not in use. Although this approach would never be economically or ecologically viable for home refrigeration units, the energy that could be saved in attaining cryogenic temperatures could make a valuable contribution towards the preservation of our world.

Apart from such 'real world' applications, the performance characteristics of optical cryocoolers could also indirectly contribute to other scientific advances. As

non-vibrational, rapid refrigeration devices they may be applied in a wide variety of experiments requiring noise-minimized fine temperature control.

New record temperatures are constantly being set in the field of optical cooling of rare-earth-doped crystals, however the sample specific cooling effect is not reliable enough to become a commercially viable technique. The main stumbling block still facing the optical cooling community is the sourcing of samples that are of suitably high purity and quality to avoid parasitic heating effects. A simple technique that can spatially discriminate any optical cooling effect within a crystal from variations in the ambient temperature and fluorescence reabsorption would be an indispensable tool for initial crystal selection.

1.2 Part 1 Aims

No experiments for improving the optical cooling power can be performed unless rare-earth-doped crystals that exhibit cooling are first identified. Rare-earth-doped crystals are known to be highly sensitive to impurities and defects; different parts of a single crystal may not respond in the same way to pumping. The aim of this work was to develop a simple, robust temperature measurement technique that could discriminate optical cooling from parasitic heating effects by investigating spatial variations in the cooling effect.

1.3 Part 1 Outline

The background and theory to optical cooling is covered in two parts.

Section 1.4 begins the discussion of optical cooling with a review of the historical background to the field. Recent advances in cooling rare-earth-doped crystals are summarized and the method is placed in context with other refrigeration techniques.

Chapter 2 of this thesis discusses the basic theory of optical cooling by anti-Stokes fluorescence, including the fundamental and practical limits to the technique. The two Yb-doped host crystals investigated in this work – Yb^{3+}:YAG and Yb^{3+}:CaF_2 – are evaluated spectroscopically as cooling candidates. Chapter 2 concludes by considering the parasitic heating effects of fluorescence reabsorption and nonradiative decay.

The experimental component of this work is divided into three parts.

Chapter 3 covers the development of pump sources that are suitable for optical cooling applications both in the context of this work and for future research. During the course of this work an insight was also gained into the poorly understood phenomenon of self-pulsing in fibre lasers. The discussion in Chapter 3 identifies a distinctive 'pulse packet' as a characteristic feature of sustained self-pulsing in the fibre lasers used in this work.

Chapter 4 covers the design, development and validation of the laser-based thermometer that formed the central aim of this project. Alternative laser-based approaches to temperature measurement are discussed and an empirical comparison to photothermal deflection presented.

Chapter 5 reports the investigation of optical cooling in Yb^{3+}:YAG and Yb^{3+}:CaF samples. The practicality and usefulness of the developed temperature measurement technique is clearly demonstrated in a spatial investigation of cooling in Yb^{3+}:CaF_2. No significant net cooling was measured, but this work does present the first report of local cooling in an Yb^{3+}:CaF_2 crystal by 0.15±0.05K from the initial temperature and 1.4±0.1K relative to the bulk sample temperature.

Chapter 6 concludes Part 1 with a review of the benefits that the temperature measurement technique developed in this work brings to the measurement of optical cooling. The conclusions that may be drawn from this work are discussed and potential avenues of future research outlined.

1.4 Background to Optical Cooling

This section reviews the field of optical cooling by anti-Stokes fluorescence. It is important to note that this laser-based cooling technique should not to be confused with laser-Doppler cooling (see Section 1.4.3). Recent advances in optical cooling of rare-earth-doped crystals are placed in context with other established refrigeration techniques.

1.4.1 Historical Background

Shortly after the discovery by Raman & Krishnan in 1928 that scattered light contains lines of lower (Stokes) and higher (anti-Stokes [2]) frequencies than the incident light [3], Pringsheim first postulated a theory of optical cooling in sodium vapour [4]. He proposed pumping the $1^2S_{1/2} \rightarrow 2^2P_{1/2}$ transition (D_1 line) using the filtered D_1 0.5896μm transition from a separate sodium lamp source. The pressure of the vapour would be kept low enough to ensure that nonradiative decay processes were minimized while remaining sufficient to allow thermalization of the $2^2P_{1/2}$ and $2^2P_{3/2}$ energy levels. Decay would predominantly be fluorescence on the $2^2P_{3/2} \rightarrow 1^2S_{1/2}$ transition (D_2 line) at the shorter wavelength of 0.5890μm. Pringsheim's groundbreaking theory extended Raman & Krishnan's observations to a pumped system, but faced much controversy. While it was accepted that individual photons could be anti-Stokes shifted due to atomic thermal energy, there was disagreement as to whether the average scattered/emitted energy could be greater than the pump energy. Pringsheim argued that as the cooling system is not closed (there is a pump source doing work) cooling of the gas does not violate the Second Law of Thermodynamics. The prevalent opposing view was that for the conservation of entropy on a macroscopic scale, any anti-Stokes emission has to be balanced by Stokes-emission and thus a net cooling effect could not occur.

A direct public challenge to Prinsgheim's position did not appear until the end of the Second World War when in the space of one year a quartet of papers were

published on the 'thermodynamics of the photoluminescence yield' (ratio of the fluorescent energy to the pump energy). In 1945 Vavilov [5] argued that an excitation-fluorescence cycle had to be reversible. If the energy yield were greater than unity, when operated in reverse there would be complete transfer of heat into work. Pringsheim immediately responded [6] to Vavilov's case by arguing that as a unidirectional monochromatic pump beam is being converted into isotropic broad-band fluorescence, the process cannot be reversible. In his 1945 paper Pringsheim also briefly outlined the fundamental conditions required for cooling, namely that the system must have sufficient time to reach thermal equilibrium (short thermalization timescale) and that the quantum efficiency[1] should be as close to unity as possible. Vavilov countered [7] Pringsheim's defence by citing an apparatus designed in 1743 that could collect and re-collimate fluorescence (converting it back into a unidirectional beam as is the pump). In his rebuttal Vavilov also described an optical cooling experiment that included both a Stokes-shifting sample and an anti-Stokes shifting sample in the same cavity. His analysis of this system was that there would be work-free transfer of energy from the hotter to the colder reservoir, again in violation of Carnot's theorem. Later in 1946 Landau finally presented a sound thermodynamic proof that the photoluminescence energy yield can exceed unity [8]. Integrating over the spectral range and solid angle for a photon gas described using Bose statistics, he showed in terms of an 'effective (pump) temperature' that the cooling effect is proportional to the difference in mean energy between the pump and the fluorescence. Although Landau (and subsequently Vavilov) dismissed this effect as being insignificant, it nevertheless proved that optical cooling was theoretically possible.

At this time the absence of sources for pumping atoms at reasonable powers above their mean fluorescence wavelength prevented any substantial progress in the field of optical cooling. The experiments with sodium and iodine vapours proposed by Pringsheim [4, 6] were, however, refined by Kastler [9] who in 1950 proposed the use of an inert 'buffer' gas such as helium or argon to minimize 'collisional quenching' (nonradiative decay) and the thermalization timescales. Practical constraints meant that Kastler never performed these experiments and even

[1] Not to be confused with the photoluminescent/fluorescent energy yield.

concluded his theoretical work by saying, "*this effect is likely to remain a scientific curiosity rather than a practical technique for obtaining low temperatures.*" The revolutionary advent of the laser in 1959, however, meant that all that was about to change.

In the interim, the absence of adequate optical pump sources led to scientific interest turning to the use of electroluminescence for cooling. First observed during the early 1950s [10-12], electroluminescence cooling is theoretically very similar to optical cooling by anti-Stokes fluorescence. In 1953 Lehovec noticed that the shortest wavelength photons emitted by a semiconductor exceeded the applied electrical energy [13] and proposed that this is due to the withdrawal of internal (thermal) energy from the lattice. In 1957 Tauc developed this idea, discussing the possibility of harnessing the phenomenon to achieve luminescence cooling in a semiconductor [14]. Dousmanis *et al.* subsequently proved experimentally that the average electroluminescent photon energy from a GaAs diode can exceed the energy supplied by the bias voltage [15].

The similarity between electroluminescence and photoluminescence was first recognized by Weinstein who in 1960 published a generalized approach to the thermodynamic issue of converting heat to light [16]. The theory continued to be developed and in 1961 Yatsiv presented the definitive prototypical optical cooling cycle for solid-state cooling [17] based on a rate-equation analysis for Gd^{3+}. As early as 1959 Scovil & Schulz-DuBois had discussed the theoretical limiting factors to cooling in a 3-level system [18]. This analysis was taken further by Kafri & Levine who in 1974 emphasized entropy considerations in this model and the benefits of 4-level over 3-level systems [19]. More recently the theory has been developed in the context of high intensity pumping by Geva & Kosloff [20] and Palao *et al.* [21].

In the years following the successful demonstration and rapid development of the laser, attention shifted back to using anti-Stokes fluorescence for cooling. A range of experiments were designed using available lasers for the cooling of heteronuclear diatomic gases such as carbon monoxide [22-24], organic dye solutions and rare-earth-doped crystals. By 1968 Kushida & Geusic had demonstrated the potential for optical cooling achieving 'reduced heating' in a Nd:YAG crystal placed within a

Nd:YAG laser cavity [25]. In this experiment a 0.1inch × 2inch Nd:YAG rod was supported *in vacuo* on three needles to minimize thermal contact with the surroundings. The temperature was measured using a thermocouple and compared to the temperature measured in an undoped YAG rod. The authors attributed their inability to achieve cooling to sample impurities. Although not noted as a cause by the authors, the vacuum chamber in this experiment was gold plated and fluorescence trapping probably contributed a significant heating effect. Although not reported by the authors this may have been the cause of the heating. In 1981 Djeu & Whitney finally tested a scheme for pumping carbon dioxide that achieved cooling of 1K from 600K [26]. In this experiment a mixture of CO_2 (partial pressure 64mtorr) and buffer xenon (partial pressure 0.2mtorr) gas was placed in a sample cylinder whose walls were maintained at 600K. The walls of the cylinder were a matt black to prevent trapping of the fluorescence. A 300W CO_2 pump laser was used to excite the gas on the 10.6μm *100* → *001* vibrational combination transition. Decay was then on the 4.3μm *001* → *000* transition. This was the first reported observation of optical cooling. Despite this achievement and later reports of microwatt-level cooling in rhodime 6G dye solutions [27, 28], the field of optical cooling did not really advance until optical cooling of Yb^{3+}-doped glass was reported by Epstein *et al.* in 1995 [29].

1.4.2 Optical Cooling of Rare-Earth-Doped Solids

The use of rare-earth-doped crystals for optical cooling was first proposed by Kastler in 1950 [9]. He suggested that a rare-earth-doped salt crystal could be pumped in the anti-Stokes region to achieve cooling. The principle advantage of rare-earth dopants – specifically the lanthanide series – is that they have optically active *4f* levels that are shielded from other atoms by filled outer *5s* and 5*p* shells.

In the Yb^{3+}:YAG and Yb^{3+}:CaF_2 crystals used in this work, one electron from the $6s^2$ level and another from either the *5d* or *4f* level bond with neighbouring oxygen or fluorine atoms. Normally a single *4f* electron is involved in the bonding and the dopant ions have a 3+ electric charge. It is possible, however, to have other bonds for which the ions have a 2+ or 4+ charge. This can lead to parasitic heating effects. The

result of *4f* level bonding is that the *5s* and *5p* outer shells remain filled, thus decreasing the probability of the atom interacting with the lattice. This reduces the potential for multiphonon nonradiative decay. Importantly the spherical symmetry of the filled outer shells means that they do not have a significant impact on the optically active *4f* electrons. As the optical transitions occur within a manifold, there are narrow spectral lines corresponding to Stark split sublevels. The result is a higher pump absorption than could be achieved with other dopants. These three properties make rare-earth-dopants ideal for optical cooling applications.

Apart from the single report of reduced heating by Kushida & Geusic [25], no progress was made in the optical cooling of rare-earth-doped solids until Epstein *et al.* reported cooling of 0.3K in a 2.5×2.5×6.9 mm^3 1%-doped Yb^{3+}:ZBLANP glass sample in 1995 [29]. The sample was cooled *in vacuo* from room temperature using a tuneable Ti:sapphire pump source and the temperature measured using spectral imaging of gold foil in thermal contact with the sample. Edwards *et al.* improved on this work achieving cooling of 48K from room temperature [30]. In wavelength-controlled experiments they pumped a 12mm × 10mm Yb^{3+}:ZBLAN cylinder using a Ti:sapphire laser. Cooling of 48K was achieved with 1.6W of 1.030μm. The experiment was performed in a vacuum chamber coated for high fluorescence absorption and low thermal emissivity to minimize parasitic heating. Mungan *et al.* extended the work reported in [29] to a fibre sample geometry. This geometry increased pump absorption and with 770mW of 1.015μm pump cooling of 16K from 298K in a 1%-doped Yb^{3+}:ZBLAN fibre was reported [31]. Increasing the pump power to 1360mW in a similar experimental set-up, Luo *et al.* improved on these results achieving cooling in a Yb^{3+}:ZBLAN fibre of 21K [32]. Employing a high reflector to double pass the substantial residual pump light through the fibre and reducing thermal contact by use of fibre supports, Gosnell measured a temperature drop of 65K from room temperature using a thermocouple [33]. This demonstrated the importance of isolating the cooling sample when performing low power cooling experiments. In his paper Gosnell reported that the external heat load is the only limiting factor in this case. Although only achieving a temperature drop of 13K using 0.85W of 1.015μm pump, the work done by Rayner *et al.* [34] confirms the above findings of the team at Los Alamos National Laboratory (LANL) into the optical

cooling of Yb^{3+}:ZBLAN(P). At LANL Thiede *et al.* since demonstrated the record reported cooling for Yb^{3+}:ZBLAN of 88K in from room temperature [35]. In this experiment a 2%-doped 12mm × 10mm cylinder was pumped with ~10W of 1.026μm light and monitored using a thermocouple. The sample was pumped for one hour before reaching its minimum equilibrium temperature. An alternative pump scheme has been reported by Heeg *et al*. [36] who used intracavity pumping to cool Yb^{3+}:ZBLAN by 6K. This experiment involved the use of a rectangular sample placed inside an Yb^{3+}:KYW bulk laser cavity operating at 1.039μm. Yb^{3+}:ZBLAN(P) has been the most widely used cooling material to date and holds the distinction of having been the cooling medium in the first optical refrigerator [37].

In the 1μm-regime attention has shifted from Yb^{3+}-doped glasses to crystals. Yb^{3+}:YLF has recently been used by Seletskiy *et al.* as the cooling sample in record cooling to a temperature of 155K [1, 38]. A theoretical analysis shows that by increasing the absorbed pump power at 1.020μm it is theoretically possible to reach temperatures as low as 100K using their set-up [39]. Yb^{3+}:YLF has also been used to build an optical refrigerator for cooling a semiconductor sample to 165K [40]. It should be noted that the semiconductor sample in this experiment had a thickness of only 2μm and thus the practical application of this optical refrigerator has not been proven.

The experiments reviewed in this section focus on achieving cooling for the ultimate objective of building optical refrigeration devices. Another application is to offset heat generation in lasers thereby mitigating the thermal degradation effects discussed in Section 1.2.4. This was first considered by Bowman [41] and has since been discussed in a more practical context by Nemova & Kashyap [42] who propose co-doping a fibre with separate lasing (Yb^{3+}) and cooling (Tm^{3+}) rare-earth ions.

A range of other Yb^{3+}-doped glasses and crystals have been investigated for cooling [43-46] and a substantial body of work discusses the difficulties in finding suitable samples [34, 47, 48]. In cases when optical cooling is identified in a sample it is often observed only as a local effect and net temperature decreases are not reported [44, 46, 49].

Although Yb^{3+}-doped solids have been the most widely investigated due to the ready availability of pump sources and diagnostic equipment in the 1μm-regime, the benefits of other rare-earth-dopants have also been studied. Fernandez *et al.* have demonstrated cooling of 0.7K in Er^{3+}-doped KPb_2Cl_5 crystal and 0.5K in Er^{3+}:CNBZn glass [50]. The authors account for their discrepancy between the empirical and theoretical cooling powers by the reabsorption of fluorescence in the sample and upconversion effects that are more pronounced than for Yb^{3+}. Also in the 1.5μm-regime Nemova & Kashyup have presented detailed theoretical models for the cooling of Er^{3+}-doped solids [51]. They do not discuss the role of impurity reabsorption. In the 2μm-regime Tm^{3+}:ZBLANP glass has been cooled by over 30K [52, 53] and $Tm3^{+}$:BaY_2F_8 has been used to measure cooling of 3.2K [54, 55].

1.4.3 Context of Optical Cooling

The successful optical cooling experiments reviewed in Section 1.4.2 above are all performed *in vacuo* to avoid convective heating effects and the two reported refrigerators [37, 39] use very thin samples to prevent fluorescence heating of the samples dominating the cooling effect. Thus optical cooling does not currently have practical applications as a refrigeration technique. To assess the potential benefits that an optical refrigerator could provide, this section compares qualitatively the cooling powers and minimum temperatures that can be attained by optically cooling samples to other refrigeration techniques. The distinction between laser cooling by anti-Stokes fluorescence and laser-Doppler cooling is clarified.

The most widely used method of refrigeration is the Joule-Thomson process (sometimes known as the Joule-Kelvin process) [56]. This involves applying work to force a gas through a valve from a region of small to large volume. As the gas expands to fill the volume it cools and, provided that the system is isolated, the net temperature of the gas will decrease. Repeating this process leads to an incremental cooling cycle. The minimum temperature that can be achieved using the Joule-Thomson process is theoretically limited only by the Third Law of Thermodynamics.

The other common refrigeration technique uses the thermoelectric effect, more specifically the Peltier effect. If a voltage is applied across the junction of two different conductors, the charge carriers will transfer thermal energy from one material to the other in an attempt to re-establish equilibrium. This results in the continuous transfer of heat from one surface to the other, the flow of which will depend on direction of the voltage applied. The maximum temperature change that can be achieved using a Peltier controller is limited (depending on the specific design) to approximately ±80K [57].

The principal drawbacks of the Joule-Thomson process are its slow and mechanical nature. The temperature of such a refrigerator cannot be rapidly adjusted and vibrations due to the active components can seriously impact on sensitive scientific experiments. The current solution is to use semiconductor Peltier coolers for such applications. Although these offer rapid, controllable, non-vibrational cooling, the achievable temperature changes are limited. Optical refrigerators would offer all the advantages of Peltier coolers, but with the added benefit that they cover a much broader temperature range. The theoretical analysis presented in Chapter 2 shows, however, that while cryogenic temperatures may be reached with an optical refrigerator, the fundamental cooling limit is not governed by the Third Law of Thermodynamics. Thus for reaching ultra-low temperatures the Joule-Thomson process and related regenerative/recuperative cycles are the only available refrigeration techniques.

The term ‘laser cooling’ is most commonly applied to the technique of laser-Doppler cooling of gases [58]. This uses a pump beam that is slightly offset from the absorption line of the cooling atoms. The offset is adjusted such that the Doppler-shifted wavelength for atoms travelling towards the pump beam is then matched to the absorption line. Thus only atoms moving directly towards the pump beam will experience photon absorption and momentum transfer. The result is a gradual decrease in the momentum/energy of the atoms and the gas will cool. In ‘optical cooling’ as covered in this thesis, fluorescence removes energy from the system rather than a directional momentum transfer process.

Chapter 2

Theory of Optical Cooling

This chapter covers the theory of optical cooling. In Section 2.1 the general theoretical background to optical cooling is discussed in the context of Yb^{3+}:YAG ($Yb^{3+}:Y_3Al_5O_{12}$). The fundamental principles of optical cooling are reviewed alongside the spectral analysis required for sample selection. Section 2.2 extends the theory as derived for Yb^{3+}:YAG to consider $Yb^{3+}:CaF_2$ as an alternative candidate for cooling in the 1μm-regime. Section 2.3 concludes this chapter with a discussion of the parasitic heating effects in optically cooled crystals: fluorescence reabsorption and nonradiative transitions due to ion-ion interactions. Parasitic heating is discussed in the context of both dopant and impurity ions.

2.1 Optical Cooling in Yb^{3+}:YAG

The theoretical analysis of cooling in Yb^{3+}:YAG is divided into two parts. Section 2.1.1 covers the fundamental principles of optical cooling and the relevant spectral analysis of Yb^{3+}:YAG as a candidate for cooling. Section 2.1.2 reviews the two principal constraints on the attainable cooling. The fundamental absorption limit to cooling is first discussed and then the practical constraint of bleaching is derived.

2.1.1 Fundamental Principles

Optical cooling by anti-Stokes fluorescence is founded upon the principle that at a given temperature the fluorescence spectrum from a sample remains unchanged regardless of the wavelength that is used to initially excite the electrons (Vavilov's Law [5]). This statement is true if:

$$\tau_{fl} \gg \tau_{th} \tag{2.1}$$

where τ_{fl} is the fluorescence lifetime of excited electrons and τ_{th} is the thermalization timescale of upper manifold. For Yb^{3+}:YAG the fluorescence lifetime is 951μs, significantly greater than the typical ~1μs thermalization timescale of the crystal manifolds. Thus it is a suitable candidate for optical cooling.

The fluorescence spectrum $F(\lambda)$ may be modelled as pure emission at some mean wavelength λ_m that can be calculated by:

$$\lambda_m = \frac{\int (F(\lambda) \times \lambda)\, d\lambda}{\int F(\lambda) d\lambda} \tag{2.2}$$

In the first work on optical cooling in dye suspensions, Erickson [59] used this equation to calculate the mean fluorescence energy. In his model Erickson showed that if a sample were pumped above this wavelength (i.e. at a lower energy), the net effect would be the removal of energy from the sample by the fluorescence. Conservation of energy requires that this energy difference is provided by phonons in the cooling medium (i.e. thermal energy). Thus a pure sample that is pumped above this mean fluorescence wavelength should exhibit cooling. Erickson's model was, however, incorrectly based on the assumption that the mean fluorescence wavelength calculated in Equation 2.1 corresponded to the mean photon energy. A more rigorous analysis shows that to find the mean wavelength λ_{fl} above which cooling occurs, the fluorescence spectrum must be normalized by photon energy:

$$\lambda_{fl} = \frac{\int \left(\frac{F(\lambda)}{hc} \times \lambda^2\right) d\lambda}{\int \left(\frac{F(\lambda)}{hc} \times \lambda\right) d\lambda} \tag{2.3}$$

For many samples this difference is relatively insignificant (e.g. for Yb^{3+}:CaF λ_m = 1.008μm, λ_{fl} = 1.009μm), however for Yb^{3+}:YAG (λ_m = 1.019μm, λ_{fl} = 1.024μm) the difference significantly shifts the optimum pump wavelength. Assuming that for each absorbed pump photon one photon is emitted at λ_{fl} the theoretical cooling efficiency[1] η_{cool} that can be achieved is then determined by the difference in energy between the pump wavelength λ_p and this mean fluorescence wavelength:

$$\eta_{cool} = \frac{\lambda_{fl} - \lambda_p}{\lambda_p} = \frac{\lambda_{fl}}{\lambda_p} - 1 \tag{2.4}$$

Although rare-earth-dopants are well shielded from the lattice, in reality a certain fraction of the decay will be due to nonradiative multi-phonon decay and ion-ion cross-relaxation (see Section 2.4). To account for this Equation 2.4 must be modified to include a quantum efficiency factor η_Q describing the fraction of radiative decay[2]:

$$\eta_{cool} = \eta_Q \cdot \left(\frac{\lambda_{fl}}{\lambda_p} - 1 \right) \tag{2.5}$$

Modelling of the Emission Cross-Section

A rate equation analysis for a crystal requires that values for the absorption $\sigma_a(\lambda)$ and emission $\sigma_e(\lambda)$ cross-sections are known. Absorption data is readily available either in terms of cross-section or absorption coefficient $\alpha(\lambda)$ which are related by the simple equation [60]:

$$\alpha = \sigma_a N \tag{2.6}$$

where N is the atomic number density.

[1] In this definition a negative value for η_{cool} corresponds to cooling.

[2] i.e. Q = 1 corresponds to purely radiative decay.

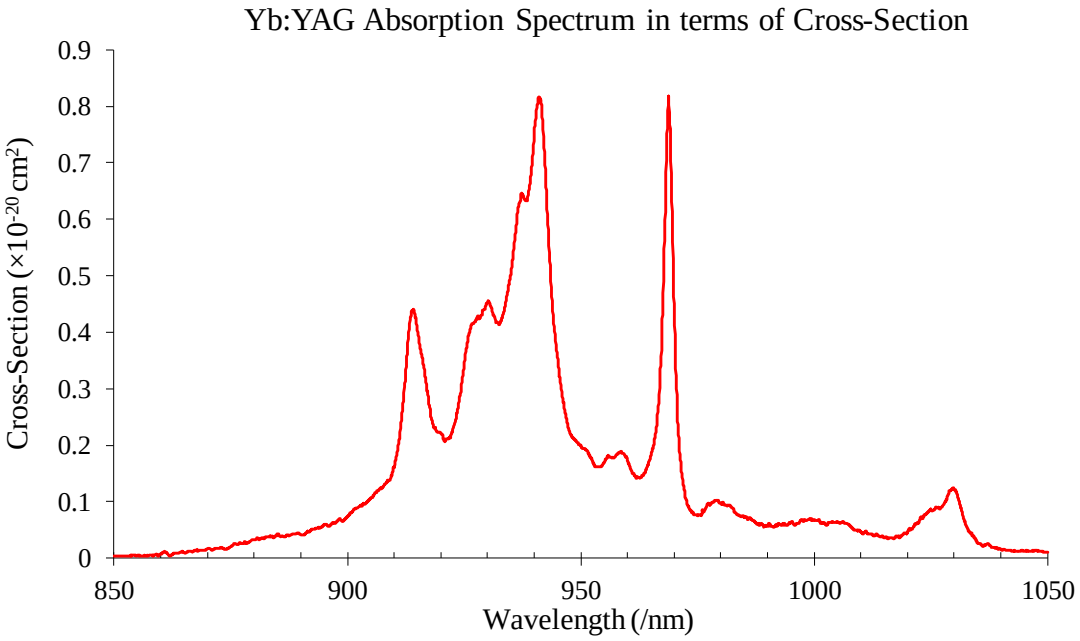

Figure 2.1 – *Yb^{3+}:YAG absorption spectrum in terms of absorption cross-section, found from absorption coefficients after* [60].

Emission data, however, is usually presented in terms of fluorescence intensity. It is therefore useful to be able to calculate the emission cross-section from measured absorption cross-sections. This is most commonly performed using the McCumber relation [61, 62] (also known as the reciprocity method) discussed below. Alternative techniques are: the Füchtbauer-Ladenburg equation [63], the β-τ method [64], small signal analysis [65] and direct measurement of saturated gain [66].

The absorption cross-section from the lower *n* manifold and emission cross-section from the upper *m* manifold may be expressed in terms of the individual cross-sections within each Stark-split manifold. In this case:

$$\sigma_a = \frac{\sum_{nm} d_n d_m \sigma_{nm} exp\left(\frac{-E_n}{k_B T}\right)}{Z_L} \tag{2.7}$$

$$\sigma_e = \frac{\sum_{nm} d_n d_m \sigma_{mn} exp\left(\frac{-E_m}{k_B T}\right)}{Z_U} \tag{2.8}$$

where d_n and d_m are the level degeneracies, E_n and E_m are the energy levels measured from the lowest level in each manifold, k_B is the Boltzmann constant, T is temperature and the partition functions of the lower Z_L and upper Z_U manifolds respectively are given by:

$$Z = \sum_i d_i exp\left(\frac{E_i}{k_B T}\right) \tag{2.9}$$

Employing the reciprocity relation:

$$\sigma_{nm} = \sigma_{mn} \tag{2.10}$$

and defining the 'zero-line energy' E_{00} as the spacing between the lowest energy level in each manifold, the spacing between any two energy levels is related to the energy of the photon involved in the transition by:

$$\Delta E_{mn} = E_m - E_n = \frac{hc}{\lambda_{nm}} - E_{00} \tag{2.11}$$

Dividing Equation 2.8 by 2.7, substituting 2.11 and rearranging to give σ_e in terms of σ_a the McCumber relation is derived:

$$\sigma_e(\lambda) = \sigma_a(\lambda) \frac{Z_L}{Z_U} exp\left(\frac{E_{00} - \frac{hc}{\lambda}}{k_B T}\right) \tag{2.12}$$

The Stark-split energy levels of the Yb^{3+}:YAG lower $^2F_{7/2}$ and upper $^2F_{5/2}$ manifolds found by Öberg & Lundberg [67] are shown in Table 2.1 and Figure 2.2.

Level	Energies *(cm^{-1})*	No. Levels
$^2F_{7/2}$	0, 566, 613, 786	4
$^2F_{5/2}$	10328, 10625, 10680	3

Table 2.1 – *Stark-split energy levels in Yb^{3+}:YAG after* [67].

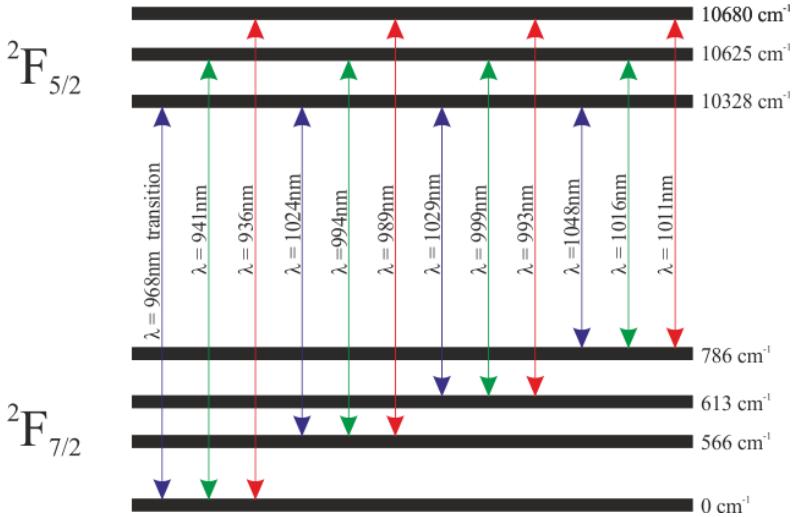

Figure 2.2 – *Stark-split energy levels for the $^2F_{7/2}$ and $^2F_{5/2}$ manifolds in Yb^{3+}:YAG after* [67] *showing the wavelengths of the various transitions. Level energies shown in units of cm^{-1} with respect to the lowest level of the $^2F_{7/2}$ manifold.*

Applying Equation 2.9, the partition functions of the $^2F_{7/2}$ and $^2F_{5/2}$ levels can be calculated to be 1.137 and 1.418 respectively. This is in agreement with the values calculated by Straesser & Ostermeyer [68]. Thus the McCumber relation can be applied to the Yb^{3+}:YAG absorption values in Figure 2.1 to give the emission cross-section (Figure 2.3).

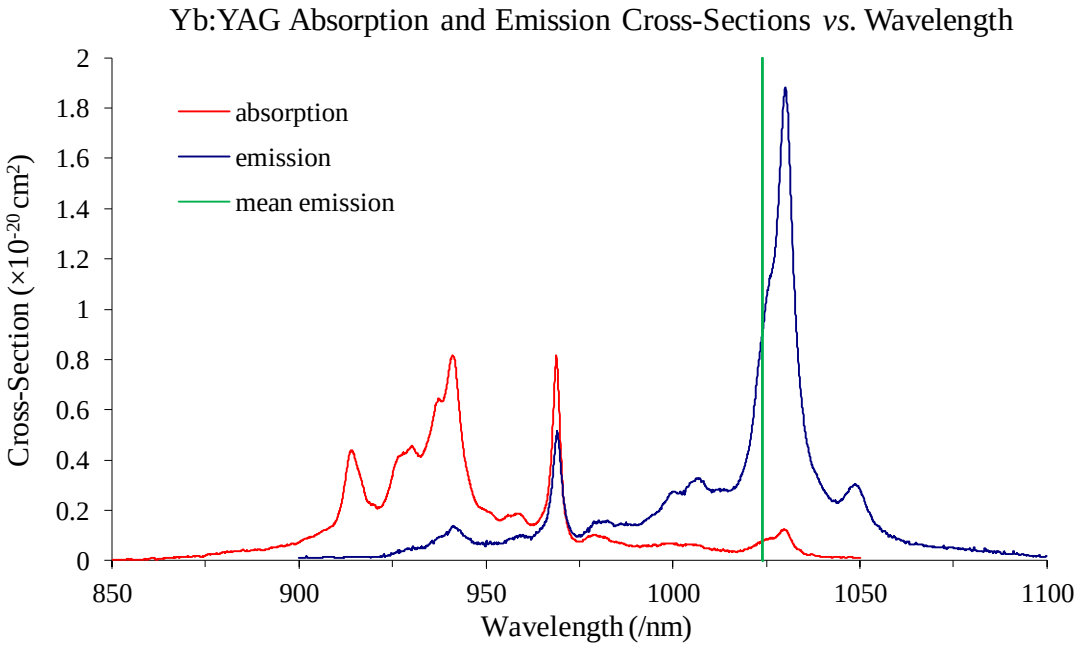

Figure 2.3 – *Yb^{3+}:YAG absorption (red) and emission (blue) cross-sections and the mean emission wavelength (green) at 1.024μm. Emission cross-section calculated using the McCumber relation using absorption values after* [60].

Optimum Pump Wavelength

Equation 2.5 shows that the cooling efficiency increases with pump wavelength. However, as the pump wavelength increases the pump absorption coefficient in a sample falls off. Thus there is an absorption limited effective cooling efficiency η_{cool}` (Equation 2.13) and there will be an optimum wavelength λ_{op} (found from Equation 2.14) at which the attainable cooling power that can be achieved, assuming no parasitic heating effects other than the multiphonon transitions described by parameter η_Q, will be maximized.

$$\eta_{cool}` = \eta_{cool} \times \eta_{abs} = \eta_Q \times \left(\frac{\lambda_{fl}}{\lambda_p} - 1\right) \times \left(1 - e^{-\alpha(\lambda_p)l}\right) \tag{2.13}$$

$$\frac{d}{d\lambda_p}(\eta_{cool}`) = \frac{d}{d\lambda_p}\left[\eta_Q \times \left(\frac{\lambda_{fl}}{\lambda_p} - 1\right) \times \left(1 - e^{-\alpha(\lambda_p)l}\right)\right] = 0 \tag{2.14}$$

where l is the pumped sample length and η_{abs} is the absorption efficiency. Selecting pump sources that can reach and maintain the temperature dependent optimum pump wavelength is important for achieving high cooling powers.

It can be seen in Figure 2.4 that the optimum pump wavelength for optical cooling in a thin Yb^{3+}:YAG sample (i.e. no fluorescence trapping) that undergoes pure radiative decay at 300K is 1.030μm. This is in agreement with the value presented by Epstein [69]. The plateau effect at observed at 1.040μm is due to the limited precision of available absorption data at these wavelengths and should drop to zero. If accurate analysis of the effective cooling efficiency at longer wavelengths is required, applying the McCumber relation to values for the emission cross-section would give the absorption coefficient with a lesser degree of experimental uncertainty.

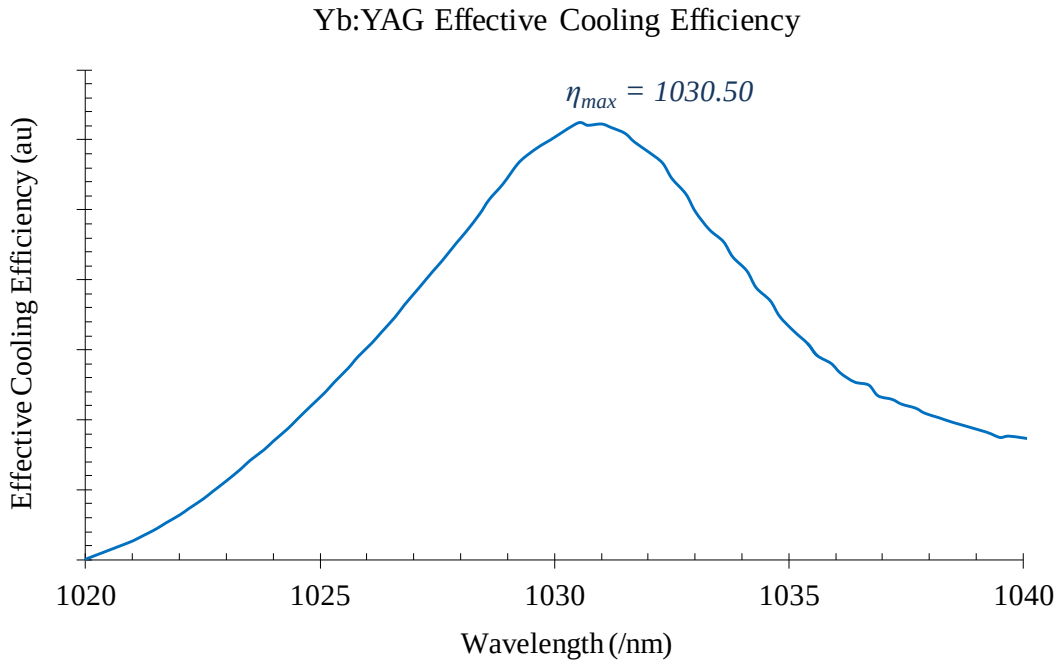

Figure 2.4 – *Room temperature effective cooling efficiency* η_{cool}` *of* Yb^{3+}*:YAG with an optimum pump wavelength at 1.030μm. 'Plateau' at long wavelengths due to increasing uncertainty in values for the absorption coefficient (approaching noise limit).*

2.1.2 Limits To Optical Cooling

There are two principle limits to the minimum temperature that can be reached with an optical refrigeration set-up. Firstly there is a fundamental absorption/emission limit for cooling due to the temperature dependence of the absorption/emission cross-sections. Bleaching also places a practical limit on the cooling powers and thus, in a system that is not perfectly isolated, the temperatures that can be achieved. This section discusses in detail each of these limits and concludes with a review of their relative impact in practical cooling applications. Sample isolation and the availability of pump sources will place other practical limits on the cooling that can be achieved.

Absorption/Emission Limited Cooling

The absorption and emission spectra of a sample depend on the Boltzmann distribution of electrons within the lower and upper manifolds and thus have temperature dependence. As discussed by Kafri & Levine [19], in a quasi-3-level system (Figure 2.5a) as the sample cools an increasing fraction of the excited electrons lie in the lower sub-levels of the manifold until the probability of Stokes-emission dominates the cooling[3] [18]. This is 'emission limited cooling'. In a 4-level system (Figure 2.5b), however, as the fluorescence transitions terminate in a lower level than that from which they are excited, anti-Stokes emission can be observed for as long as there is pump absorption. If the pump wavelength is fixed, at low temperatures quasi-3-level operation is reached (i.e. the lower sub-level for the pump transition is depleted) and there will no longer be any pump absorption. Calculation of this temperature thus defines a fundamental limit to the maximum achievable cooling. This is 'absorption limited cooling'. From this discussion it can be seen that crystals having a pronounced 4-level energy structure are favourable for cooling.

[3] i.e. an increasing mean fluorescence wavelength.

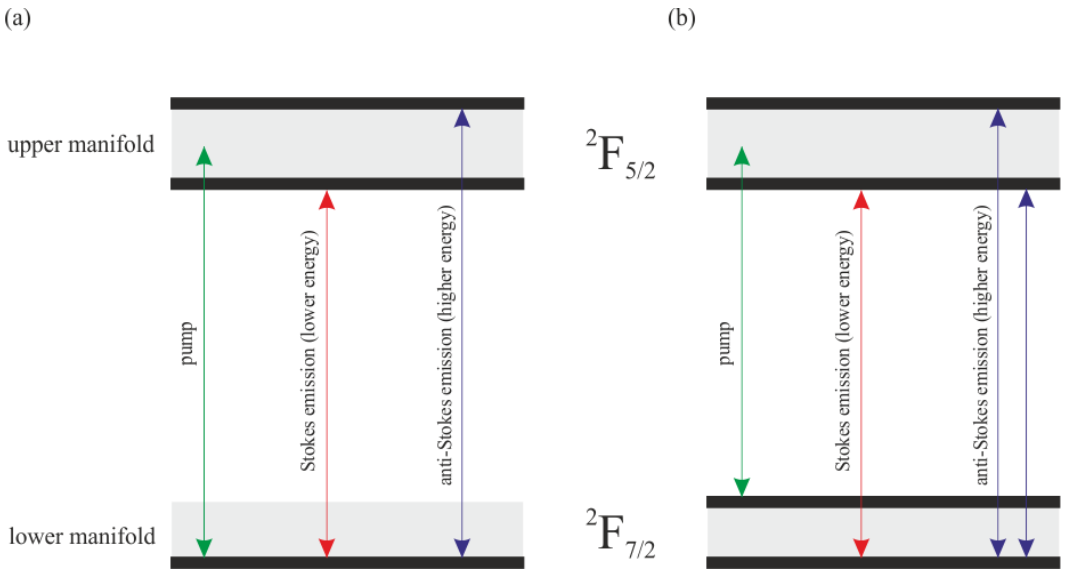

Figure 2.5 – *Pump, anti-Stokes and Stokes transitions in (a) quasi-three-level and (b) four-level optical cooling systems showing the $^2F_{7/2}$ and $^2F_{5/2}$ manifolds of Ytterbium.*

Unless the pump transition starts in a particularly high sub-level of the lower manifold (rapid depletion with temperature decrease), in practical optical cooling experiments as the temperature drops the increasing mean fluorescence wavelength is initially the dominant effect [70, 71] in reducing the cooling efficiency. Equation 2.14 shows that this shifts the optimum pump wavelength to longer values, reducing the cooling efficiency. In the work reviewed in Section 1.4.2, for which substantial temperature drops were observed, fixed pump wavelengths were used. The abilities developed in this project for tuning the pump source allow the optimum pump wavelength to be maintained as temperature decreases thereby improving the theoretically attainable cooling efficiencies.

As substantial temperature drops are achieved, the decreasing absorption cross-section becomes the principal limiting factor in Equation 2.14. This decreasing absorption has the effect of reducing the optimum pump wavelength. At some temperature T_{min} the optimum pump wavelength approaches the mean fluorescence wavelength. A pump wavelength at which the absorption is no longer sufficient to

offset any parasitic heating effects will in practice limit cooling before the fundamental absorption limit is reached.

A complete and useful model for the evaluation of T_{min} due to emission/absorption limited cooling requires detailed spectroscopic measurements of the individual cooling samples with temperature. This project did not have the scope to perform such an analysis. The theory does, however, show that the tuneable pump sources developed in this project allow for more efficient cooling to lower minimum temperatures than have been attained in previously reported work.

Bleaching Limited Cooling

Bleaching is defined as the point at which the probability of emission is equal to the probability of absorption. Above the bleaching threshold no additional pump photons can be absorbed and a material becomes transparent to any further increase in pump intensity I_p. The absorption/emission limit discussed above gives a fundamental limit to cooling in the ideal case, however the effect of bleaching will constrain the minimum temperature that can usefully be attained. It also limits the maximum achievable cooling rate. As the absorption cross-section has a significant dependence on temperature, the bleaching threshold intensity I_{bl} derived below decreases with temperature.

Considering that at the bleaching threshold the total probability of absorption must be equal to the total probability of emission:

$$N_L n\sigma_a = N_U n\sigma_e + N_U \frac{1}{\tau_{fl}} \tag{2.15}$$

where N_L and N_U are the populations of the lower and upper manifolds respectively and n is the common photon number (/photon flux).

As the total population N_T of electrons must be:

$$N_T = N_L + N_U \tag{2.16}$$

combining equations 2.15 and 2.16 the population of electrons in the lower manifold can be expressed as:

$$N_L = \frac{N_T\left(n\sigma_e + \frac{1}{\tau_{fl}}\right)}{n(\sigma_a + \sigma_e) + \frac{1}{\tau_{fl}}} = \frac{N_T(\tau_{fl} n\sigma_e + 1)}{\tau_{fl} n(\sigma_a + \sigma_e) + 1} \tag{2.17}$$

Defining a more practical criterion for the bleaching condition, that the absorption has dropped to half the weak-signal absorption:

$$N_L n\sigma_a = \frac{N_T n\sigma_a}{2} \tag{2.18}$$

Substituting Equation 2.18 for N_L and rearranging to give an equation for n at the bleaching condition:

$$n = \frac{1}{\tau_{fl}(\sigma_e - \sigma_a)} \tag{2.19}$$

The common photon number is related to the pump intensity by:

$$n = \frac{I_p}{\left(\frac{hc}{\lambda_p}\right)} \tag{2.20}$$

Substituting Equation 2.20 into 2.19, the bleaching threshold intensity is given by:

$$I_{bl} = \frac{hc}{\tau_{fl}\lambda_P(\sigma_e - \sigma_a)} \tag{2.21}$$

This is equivalent to a bleaching threshold power of:

$$P_{bl} = \frac{hc\pi w_P^2}{\tau_{fl}\lambda_P(\sigma_e - \sigma_a)} \tag{2.22}$$

where w_p is the mean radius of the pump beam in the sample.

Increasing the total number of dopant ions will not affect the bleaching intensity as it is the ratio of excited to ground-state ions N_U / N_L that determines the bleaching threshold. Increasing the number of dopants will, however, increase the pump absorption bringing the pump below the bleaching threshold over a shorter sample length.

For the typical case of a 1.032μm pump beam having mean radius 0.75mm incident on a 5%-doped Yb^{3+}:YAG rod of length 15mm at room temperature: τ_{fl} = 951μs, σ_a = 8.43×10^{-22}cm^2, σ_e = 1.21×10^{-20}cm^2; the maximum useful pump intensity is 1.8×10^4W cm^{-2} and the maximum useful pump power is 318W. This shows that at room temperature for lightly-doped Yb^{3+}:YAG the bleaching threshold does not need to be considered as a possible limiting effect to the useful cooling power that can be achieved with a simple single or multi-pass pump scheme. In the case of resonant pumping schemes, however, for which substantial pump powers will be absorbed, it must be taken into account when calculating the maximum cooling power.

Comparison of Cooling Limits

The temperature dependent absorption and emission spectra place the only fundamental limit on the minimum temperature that can be achieved by optical cooling. The effect of bleaching, however, must also be considered when calculating the cooling power as this may place a limit on the useful cooling that can be achieved at a higher temperature than the fundamental limit. A detailed spectroscopic analysis to find the absorption and emission cross-sections as a function of temperature of the samples used is required to accurately calculate both the fundamental and useful temperature limits.

2.2 Yb^{3+}:CaF_2 for Optical Cooling

The absorption and emission spectra for Yb^{3+}:CaF_2 (Figure 2.6) show the higher pump absorption above the mean fluorescence wavelength compared to Yb^{3+}:YAG. The photon energy normalized fluorescence spectrum yields a mean fluorescence wavelength of 1.009μm a decrease of 0.015μm with respect to Yb^{3+}:YAG. Thus Yb^{3+}:CaF_2 improves the effective cooling efficiency by having both increased absorption and an increased cooling efficiency (for the same pump wavelength). Performance is further improved by the lower phonon energies in CaF_2 decreasing the probability of nonradiative decay due to multiphonon transitions. Another advantage of Yb^{3+}:CaF_2 is the longer fluorescence lifetime of 2200μs, lowering the quasi-3 level thermalization limit to cooling.

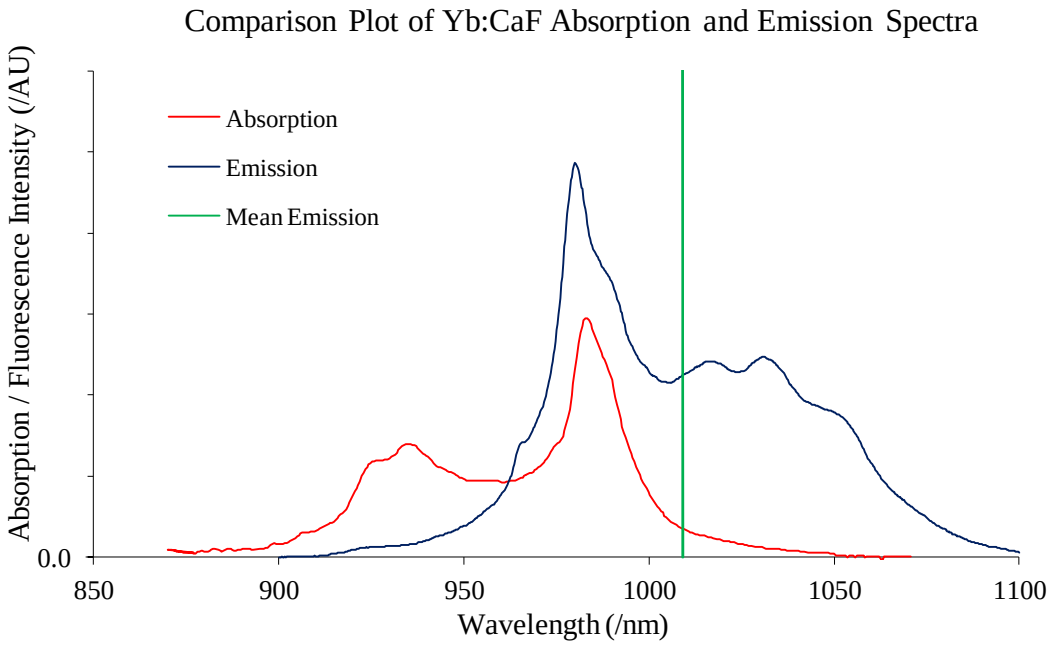

Figure 2.6 – *A comparison plot (in arbitrary units) of the absorption (red) and emission (blue) spectra of Yb^{3+}:CaF_2 showing the mean emission (green) at 1.009μm*. [72]

The relevant energy levels in Yb^{3+}:CaF_2 are shown in Table 2.2 and Figure 2.7 [72, 73].

Level	Energies (cm^{-1})	No. Levels
$^2F_{7/2}$	0, 456, 520, 588	4
$^2F_{5/2}$	10332, 10410, 10766	3

Table 2.2 – *Stark-split energy levels in Yb^{3+}:CaF_2 after* [72, 73].

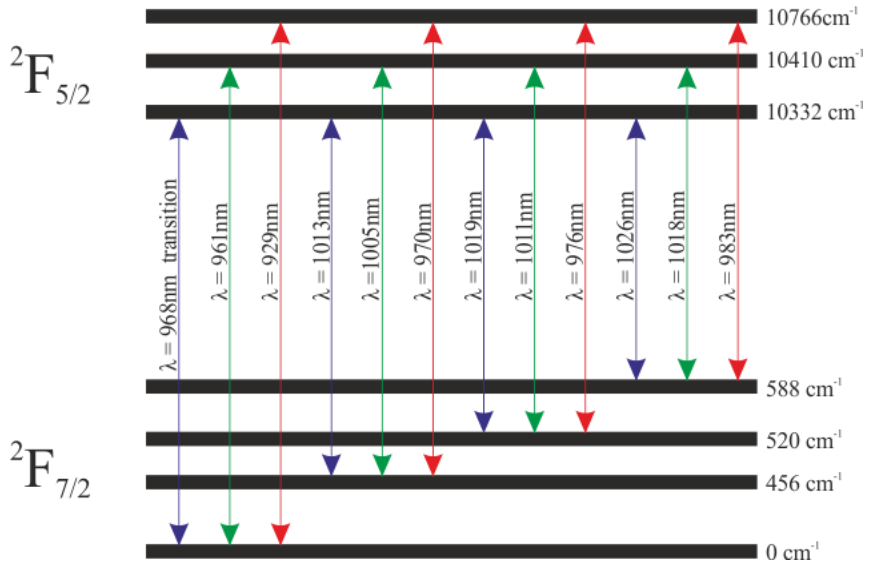

Figure 2.7 – *Stark-split energy levels for the $^2F_{7/2}$ and $^2F_{5/2}$ manifolds in Yb^{3+}:CaF_2 after* [72, 73] *showing the wavelengths of the various transitions. Level energies shown in units of cm^{-1} with respect to the lowest level of the $^2F_{7/2}$ manifold.*

Thus the partition functions of the lower $^2F_{7/2}$ and upper $^2F_{5/2}$ manifolds at 300K may be calculated to be 1.249 and 1.418 respectively. The McCumber relation (Equation 2.12) can then be applied for calculating the emission cross-section. From Equation 2.14 the optimum pump wavelength for a thin Yb^{3+}:CaF_2 sample

undergoing pure radiative emission at room temperature (Figure 2.8) can be found to be 1.035μm. There is only a minimum loss in performance down to a pump wavelength of 1.020μm.

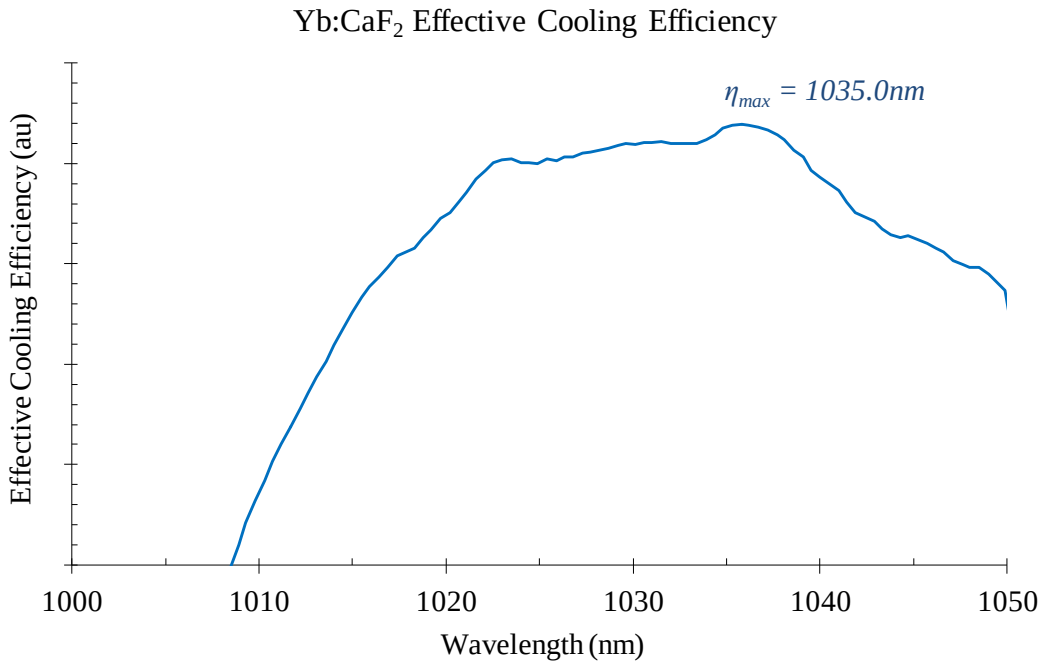

Figure 2.8 – *Effective cooling efficiency η_{cool}` of Yb^{3+}:CaF_2 with the optimum pump wavelength at 1.035μm. Irregularities in the curve with increasing wavelength due to rising uncertainty in values for the absorption coefficient.*

For the typical case of a 1.035μm pump beam having mean radius 0.75mm incident on a 3%-doped Yb^{3+}:CaF_2 rod of length 15mm at room temperature: τ_{fl} = 2200μs, $\sigma_a = 4.27\times10^{-21}cm^2$, $\sigma_e = 1.07\times10^{-19}cm^2$; the maximum useful pump intensity is 850W cm^{-2} and the maximum useful pump power is 15W. This shows that due to the longer fluorescence lifetime, at room temperature lightly-doped Yb^{3+}:CaF_2 is much more sensitive to bleaching than Yb^{3+}:YAG. Thus the bleaching threshold must be considered as a possible limiting effect to the useful cooling power for Yb^{3+}:CaF_2. The advantages of Yb^{3+}:CaF_2 over Yb^{3+}:YAG outlined above mean, however, that in most cases it would still be the preferred choice for an optical cooling sample.

2.3 Parasitic Heating Effects in Optical Cooling Samples

Sections 2.1 and 2.2 have discussed the background theory to optical cooling and the respective advantages offered by two different Yb-doped host crystals. In this section the parasitic heating effects that may limit or prevent cooling are discussed: reabsorption of fluorescence by rare-earth dopants (Section 2.3.1) and dopant-dopant or dopant-impurity interactions resulting in nonradiative decay transitions (Section 2.3.2).

2.3.1 Fluorescence Reabsorption

As the pump wavelength must lie above the mean fluorescence wavelength, a certain fraction of the dopant fluorescence spectrum overlaps with the absorption spectrum. Thus part of the fluorescence will undergo single or multiple reabsorption events before it can escape the sample. This reabsorption may be modelled as absorption at a pure mean reabsorption wavelength λ_{rabs} that can be defined by:

$$\lambda_{rabs} = \frac{\int \sigma_a(\lambda) \cdot \sigma_e(\lambda) \cdot \lambda \, d\lambda}{\int \sigma_a(\lambda) \cdot \sigma_e(\lambda) \, d\lambda} \tag{2.23}$$

As this overlap is mainly in a band below the mean fluorescence wavelength the mean reabsorption wavelength will be shorter than the mean fluorescence wavelength and radiative decay results in a heating effect η_{heat}:

$$\eta_{heat} = \frac{\lambda_{fl} - \lambda_{rabs}}{\lambda_{rabs}} = \frac{\lambda_{fl}}{\lambda_{rabs}} - 1 \tag{2.24}$$

As in the case of cooling, a certain fraction of the transitions will be nonradiative and the quantum efficiency factor η_Q must be included:

$$\eta_{heat} = \eta_Q \cdot \left(\frac{\lambda_{fl}}{\lambda_{rabs}} - 1 \right) \tag{2.25}$$

Including a term for the total probability of fluorescence reabsorption η_{rabs} Equation 2.25 can be combined with Equation 2.13 to give an expression for the effective cooling efficiency accounting for fluorescence reabsorption by rare-earth dopants:

$$\eta_{cool}` = \eta_{abs}\left(\eta_Q \cdot \frac{\lambda_{fl}}{\lambda_p} - 1\right) + \eta_{rabs}\left(\eta_Q \cdot \frac{\lambda_{fl}}{\lambda_{rabs}} - 1\right) \tag{2.26}$$

The heating effect will generally be of similar order to the cooling efficiency (e.g. Yb^{3+}:CaF_2 has λ_{rabs} = 0.986μm, η_{heat} = 2.3% c.f. η_{cool} = 2.5%), Equation 2.26 shows therefore that it is critical to quantify the reabsorption η_{rabs}. This may be calculated by applying a geometrical analysis that defines the mean path length that a fluorescent photon takes through the sample to the absorption coefficient at the mean reabsorption wavelength. Considering the case that the cooling and heating efficiencies are exactly balanced, if this mean pathlength is greater than the pumped sample length, the net effect will be heating in the sample. Thus it is important that the unpumped region of the sample is minimized requiring small sample dimensions or complex pump geometries [69].

The analysis of the mean path length must account for total internal reflection (TIR) and Fresnel reflection at the sample-air interface that leads to fluorescence trapping. The effect of multiple-reabsorption events, at each of which fluorescence may be considered to be emitted isotropically, must also be included. Several studies of deleterious fluorescence reabsorption have been performed in different fields [74, 75]. The incorrect TIR analysis in the two dimensional approximation developed by Heeg *et al.* [76] for the investigation of cooling in Yb^{3+}:ZBLAN glass has since been shown by Bigotta [54] to differ significantly from the three dimensional model. The Monte Carlo simulations presented by Bigotta demonstrate the requirement for case-specific complex mathematical modelling if the fluorescence reabsorption effect is to be accurately evaluated.

As this work did not involve growing the crystals used in the optical cooling experiments or an independent spectroscopic analysis of these crystals, a detailed theoretical analysis for fluorescence reabsorption in these samples is not performed.

Precisely to avoid the necessity for such complex modelling, the novel diagnostic developed in this work allows heating due to fluorescence to be discriminated from any cooling.

Fluorescence that escapes the sample will be incident on the surroundings (e.g. vacuum chamber, mounts etc.) and result in ambient heating. This will result in radiative and, depending on the experimental conditions, convective heating of the sample. Measures to limit this secondary source of fluorescence heating must be considered when designing an experimental set-up.

2.3.2 Ion-Ion Interactions

The other parasitic heating process that may be observed is nonradiative decay in which the transition energy is absorbed in the crystal as phonons. In the discussion in Section 1.4.2 it was shown how individual rare-earth dopant ions are shielded from the lattice. However, closely spaced dopant or dopant-impurity pairs/clusters with similar energy levels offer the potential for phonon-assisted transitions in which energy can be deposited in the crystal.

The relaxation rate S of the upper manifold in a pure crystal may be expressed as

$$S = -N_U\left(\frac{1}{\tau_{fl}} + \xi N_T\right) \tag{2.27}$$

where ξ is the cross-relaxation parameter, a term describing the probability of nonradiative decay due to dopant-dopant interactions. In this equation no term has been included for upconversion as this effect is an order of magnitude lower than the cross-relaxation in Yb^{3+}-doped samples [77].

A thorough model for cross-relaxation in a sample requires an empirical analysis of the nonradiative decay time with dopant concentration C. In the event that cross-relaxation increases linearly with the dopant concentration, it may be

concluded that a single type of energy transfer – probably due to a static process – is responsible for the effect [78]. Further, if the relationship:

$$\xi(C) = \xi_0 \left(\frac{C}{C_0}\right)^2 \tag{2.28}$$

holds [79], where ξ_o is the cross-relaxation parameter at concentration C_o, it may be concluded that dopant-dopant interactions are the dominant nonradiative decay process.

This work did not have the scope to grow and test crystals of different doping concentrations. Based on the work of other authors, however, the simple energy level structure of Yb^{3+}-doped materials means that dopant-dopant cross-relaxation is not a problem for the low doping concentrations in the Yb^{3+}:YAG and Yb^{3+}:CaF_2 samples used [72, 77].

Equation 2.27 must be modified for an imperfect crystal by the inclusion of a cross-relaxation term ζ describing the probability of dopant-impurity interactions.

$$S = -N_U \left(\frac{1}{\tau_{fl}} + \xi N_T + \zeta N_T\right) \tag{2.29}$$

Once again a full analysis of the effect of impurity decay requires an empirical characterization of the crystal in which the decay time is measured. Comparing any discrepancy between the measured and theoretical decay and having characterized the nonradiative decay rate due to dopant-dopant interactions ξ, the contribution due to impurities can then be evaluated. As in the case of dopant-dopant interactions, this work did not have the scope to empirically investigate the nonradiative decay rate. The novel diagnostic that is developed in Chapter 4 does, however, allow the effect of ion-ion interactions to be discriminated from fluorescence reabsorption heating.

Chapter 3

Developing Pump Sources for Optical Cooling

To verify the longitudinal mode-shift relative thermometry (LMRT) technique as a useful diagnostic for identifying optical cooling, a 1μm pump source was required for pumping Yb-doped samples. A suitable laser was developed to be both tuneable and power scalable in order to facilitate its use in future optical cooling research. Section 3.1 of this chapter provides a brief introduction to the benefits of fibre lasers and the reasons that a fibre rather than a bulk laser geometry was initially selected. Section 3.2 covers the developmental process of the fibre laser pump source and an incidental investigation into the phenomenon of self-pulsing. In Section 3.3 an alternative Nd:YLF bulk laser that was used for maximizing pump absorption by intracavity-pumping of samples is described.

3.1 From Bulk to Fibre Lasers

Although not as compact or of as high efficiency, diode-pumped rare-earth-doped solid-state lasers offer major advantages over simple diode lasers. Flexibility in the choice of resonator design and the mode of operation extends the range of operating wavelengths, introduces tunability and offers the potential to scale to much greater average powers than could otherwise be achieved whilst preserving high brightness.

Dominant quantum defect heating, alongside lesser energy transfer upconversion [80] and concentration quenching [81] processes, contributes to significant heating [82, 83] of a gain medium. This leads to issues of thermal lensing [84], stress-induced birefringence [85] and ultimately catastrophic failure of the gain medium itself. Various cavity configurations and external beam-shapers may be used to

partially compensate for lensing and birefringence effects [86, 87], but thermal management of the gain medium is preferred for minimizing beam degradation. The importance of diode-pumped solid-state lasers in every aspect of modern life can be seen from the volume of published research into various approaches for thermal management. Apart from advanced heat-sinking set-ups [88, 89] the documented work focuses on gain medium geometry (Figure 3.1) and even distribution of the pump beam.

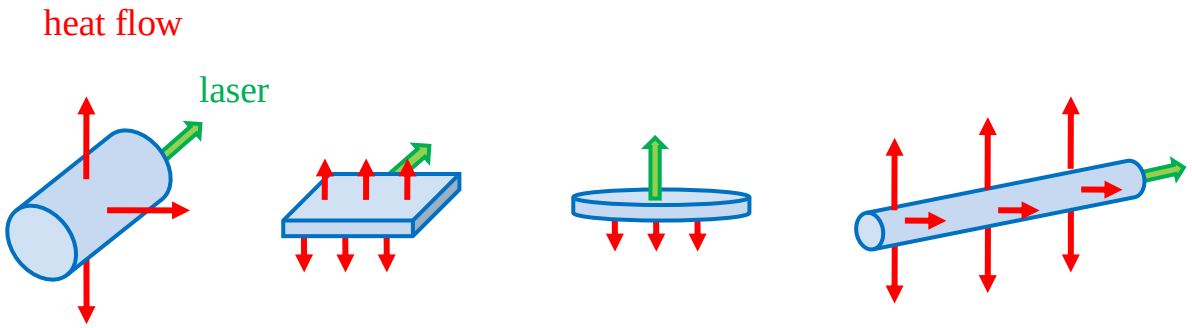

Figure 3.1 – *Various solid-state laser geometries.*

The optimum geometry for thermal management in a solid-state laser will maximize the surface area through which heat can be lost and the pumped area (i.e. giving a uniform temperature deposition profile) with minimum degradation of beam quality. This optimum is offered by the narrow-core optical fibre laser [90, 91]. The comparatively long length of the fibre distributes the heating throughout the gain medium while the small radius means that this heat is generated close to a surface of large relative area. The narrow core will discriminate against higher order transverse modes leading to a high brightness, high quality output.

A pumped rare-earth-doped optical fibre will emit a broad spectrum. Choosing a suitable dopant(/s) to cover the region(/s) of interest (e.g. Yb^{3+} at ~1μm, Er^{3+} at ~1.5μm and Tm^{3+} at ~2μm) the operating wavelength of a fibre laser may be selected anywhere within this spectral range. An external diffraction grating or volume Bragg grating (VBG) [92, 93] may be used build a widely tuneable source. Alternatively a fibre Bragg grating (FBG) [94] may integrated for narrow linewidth

single-wavelength selection in an all-fibre design. Changing the fibre length, Raman scattering of the emission spectrum can be used to reach a wider range of wavelengths than can be achieved with a short (e.g. rod) gain medium.

Depending on the required fibre length and the absorption at the available pump wavelength, a fibre laser may either be core-pumped to maximize the absorption per unit length or cladding-pumped to maximize the free-space coupling efficiency. In addition there is a degree of flexibility in designing the fibre cross-section thereby allowing asymmetry to be employed for maximizing the pump absorption in a cladding-pumped configuration.

The high beam quality, broad tunability and good thermal performance discussed above make fibre lasers ideal power scalable pump sources for optical cooling experiments.

3.2 Tuneable 1μm Fibre Lasers

The design process for the cooling pump source was undertaken with the aim of having a power scalable tuneable laser that could pump a crystal both above and below its mean fluorescence wavelength. Such a pump source could be used to extend optical cooling research using samples identified by means of the newly developed LMRT technique. To satisfy the power scaling and tunability requirements a fibre rather than bulk laser geometry was preferred. The challenges that this raised in achieving the required minimum operating wavelength are discussed within the context of the laser development process.

The principal reason that the 1μm-regime rather than the 2μm-regime was selected for the study of optical cooling was a greater availability of samples, optics and diagnostic equipment. Firstly an Yb-doped crystal was required that would have its mean fluorescence wavelength within the tuning range of a practical 1μm pump laser. At 1.024μm, Yb^{3+}:YAG has a longer mean fluorescence wavelength than most other Yb-doped crystals; a wavelength that is achievable using an Yb-doped fibre

laser. The first part of this project centred on developing a high beam quality, robust cooling pump source that could be tuned down to at least 1.020μm. Although the same source was ultimately used to pump Yb^{3+}:CaF_2, the initial aim of this design process was to satisfy the requirements for Yb^{3+}:YAG pumping.

3.2.1 Simple Tuneable 1.02μm Fibre Lasers

To generate a high quality cooling beam (the quality could be important in future research) with substantial output power, an in-house[1] D-shaped double-clad 9.6μm-core[2], 150μm-inner-cladding Yb-doped fibre with a numerical aperture (NA) of 0.075 was selected for the gain medium. This was pumped at 0.976μm with an *Apollo Instruments Inc.* 125μm-core, 0.15 NA fibre-coupled diode source[3]. The output from the pump source was collimated using an 8mm focal length aspheric lens and focused into the gain medium with an identical lens. The front (/pumped) end of the fibre was plane cleaved while the back end had a 12^o angle-polished face to prevent feedback from the facet. The back end output from the fibre was collimated using an 8mm focal length aspheric lens. Using a dichroic mirror with high transmission at 0.976μm and high reflectivity at 1.030μm to separate the pump light from any amplified spontaneous emission (ASE) signal, the pump power transmitted through the fibre was measured using a thermal power meter as a function of length *l* (Figure 3.2). For these measurements the pump source was operated at 8W. Accounting for Fresnel reflections the coupling efficiency was 97% and the fibre had a measured absorption loss of 0.21 dB m^{-1}.

[1] This fibre was fabricated at the ORC prior to the author joining the department. The spool number and fabricator are unknown.

[2] core/cladding sizes are specified in terms of diameter

[3] model: F40-976-1

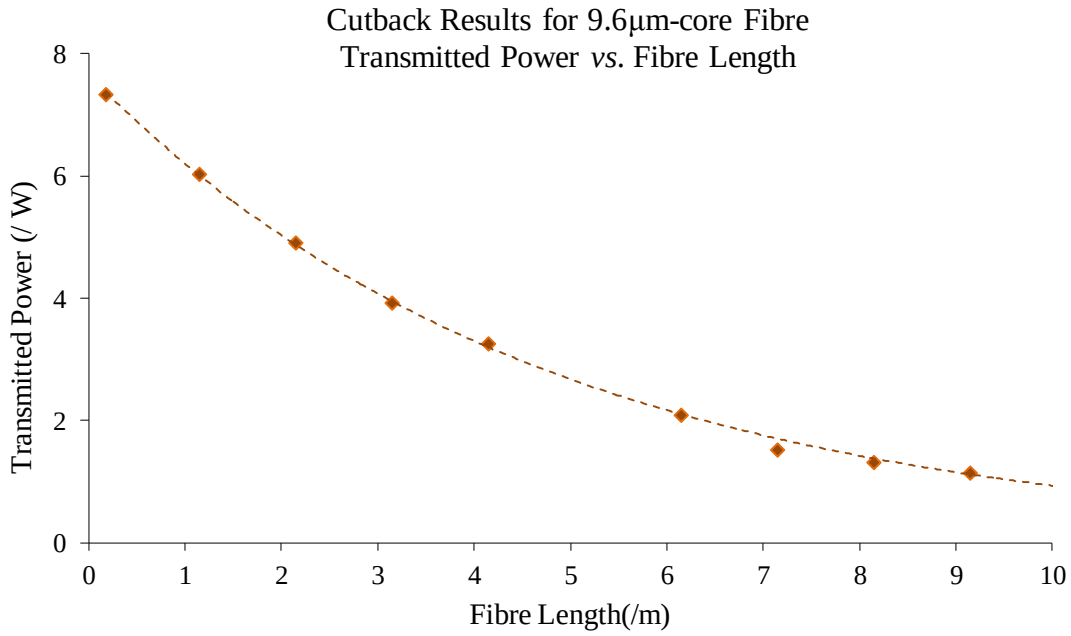

Figure 3.2 – *A plot of power transmitted through the 9.6µm-core fibre having an absorption loss of 0.21 dB* m^{-1} *as a function of length for 8W of coupled 0.976µm pump.*

Lasing was achieved using the 4% Fresnel reflection at the pumped end of the fibre and a retro-reflecting (i.e. single-pass per round trip) diffraction grating for wavelength selection at the other (Figure 3.3). A slightly angled dichroic mirror with high transmission at 0.976µm and high reflectivity at 1.030µm was situated between the front end lenses to separate the output from the pump beam. Using an initial length of 6.15m of active fibre, 4.75W of 1.039µm output[4] was achieved with a slope efficiency of 82% (Figure 3.4). In this work laser thresholds are not found from the intercept of plots of slope efficiency but by monitoring the resonator output using a *Thorlabs DET10A/M* nanosecond rise time silicon photodiode with a *Tektronix TDS5053B* digital oscilloscope. The threshold is defined as the pump power at which relaxation oscillations are first observed. The threshold in this laser was measured to be 50mW.

[4] All measured values for wavelength are found using an *ANDO AQ6Q17B* optical spectrum analyzer with a 200µm-core collection/input fibre.

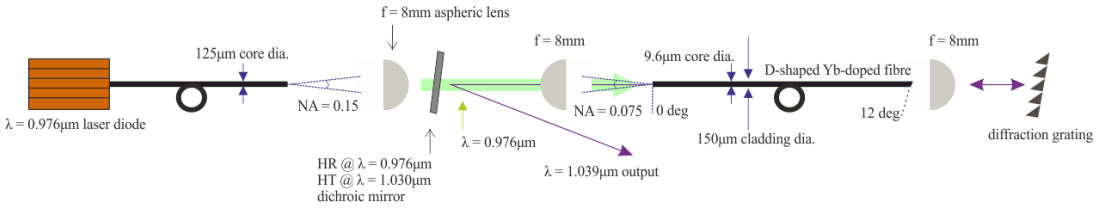

Figure 3.3 – *Schematic of a tuneable 1µm fibre laser based on a 9.6µm-core, 150µm-inner-cladding D-shaped Yb-doped fibre gain medium with an external feedback cavity including a retro-reflecting diffraction grating for wavelength selection.*

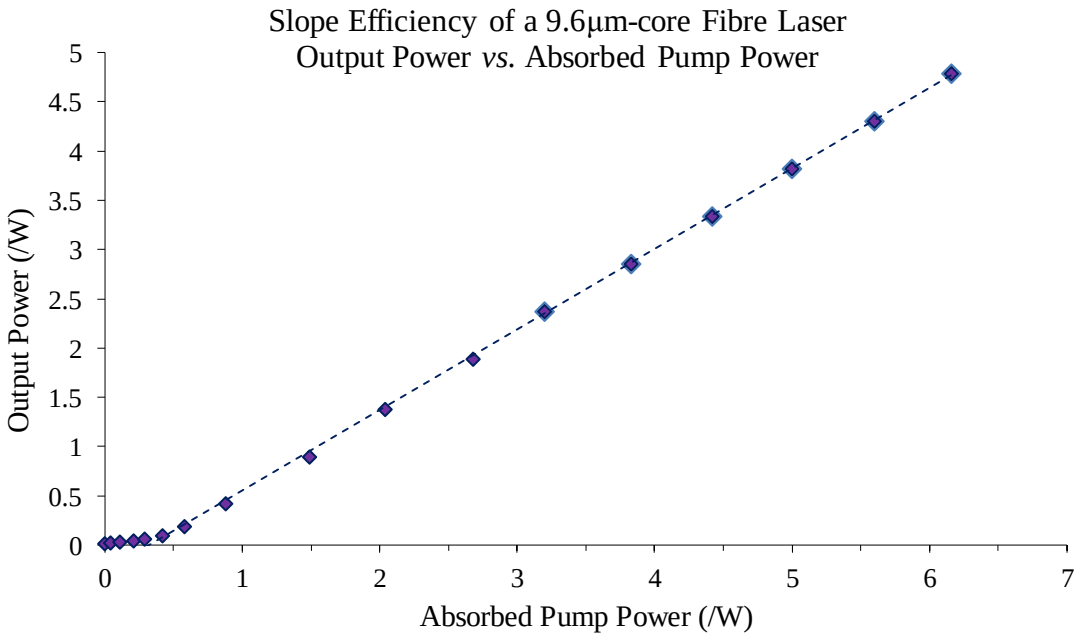

Figure 3.4 – *A plot of laser output power as a function of absorbed pump power for the 9.6µm-core fibre laser operated at 1.039µm with a slope efficiency of 82%. A slight discontinuity in gradient is observed due to the loss of one decimal place in measurements of power above 3W.*

After attenuating the laser output by a series of three 10% reflecting mirrors, the collimated beam was focused using a 200mm focal length lens. The beam diameter was measured as a function of position through the focus using a *DataRay Inc. Beamscope*^{TM}*-P7* silicon two-slit beam profiler. Making the paraxial approximation within the Rayleigh range Z_R, values for the spot size w_o (radius) and Z_R may be found from a plot of beam diameter *vs.* position (Figure 3.5) and Equation 3.1 applied to calculate the M^2 parameter of the measured beam.

$$M^2 = \frac{n\pi w_o^2}{Z_R \lambda} \tag{3.1}$$

where n is refractive index (i.e. unity in air) and λ is wavelength. Performing this analysis the 9.6µm-core fibre laser was measured to have an M^2 parameter of 1.2 when operated at 1.039µm.

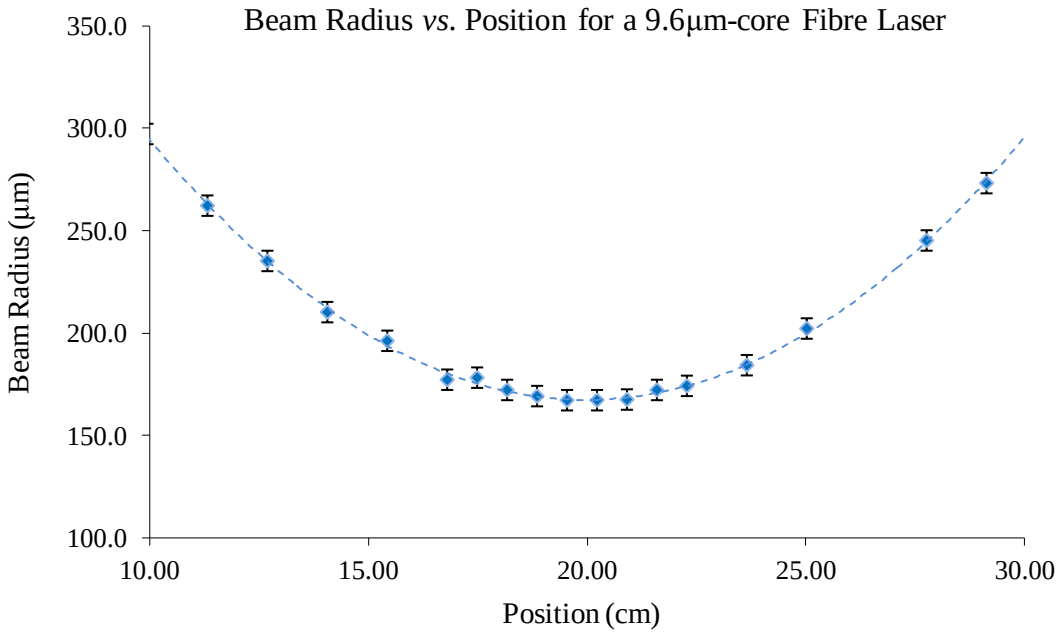

Figure 3.5 – *A plot of beam radius vs. position within the Rayleigh range for the 9.6µm-core fibre laser with* M^2 *= 1.2. The ±5µm uncertainty corresponds to fluctuations in the beam radius measured using a two-slit beam profiler.*

Over the 6.15m active fibre length, the minimum achievable wavelength was limited to 1.035μm. In order to reach lower wavelengths the relationship between the tuning range (minimum attainable wavelength) and fibre length was studied (Figure 3.6). The objective of 1.020μm operation could be reached with 1.7m of fibre, however limited pump absorption over this length meant that only 200mW of output power could be achieved.

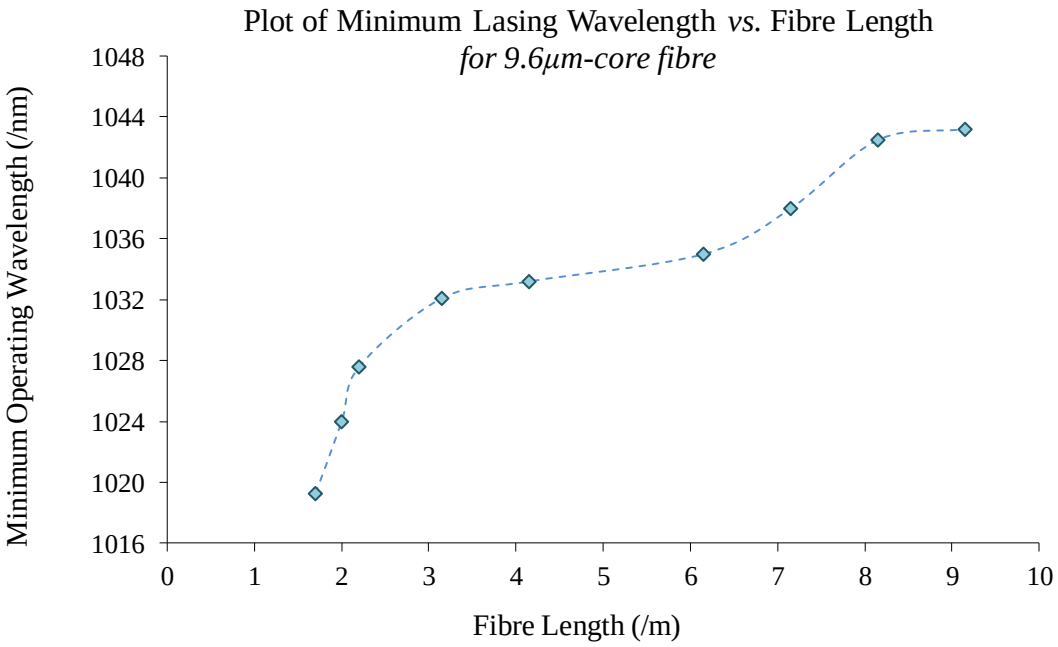

Figure 3.6 – *A plot showing the minimum lasing wavelengths achieved as a function of fibre length for the 9.6μm-core fibre laser. 1.020μm operation can be achieved with a fibre length of 1.7m. The 'step' effect in this data may be ascribed to peaks in the gain spectrum for Yb-doped silica.*

To resolve the power constraints incurred by using short active fibre lengths, a 27μm-core, 150μm-inner-cladding, 0.22 NA double-clad fibre was designed and fabricated[5] to replace the gain medium. The scaling of the core-cladding area ratio was determined to allow 90% of the pump power to be absorbed over 1.2m. Performing cutback experiments as for the 9.6μm-core fibre, this corresponds to a measured absorption loss of 2.05 dB m^{-1} (Figure 3.7).

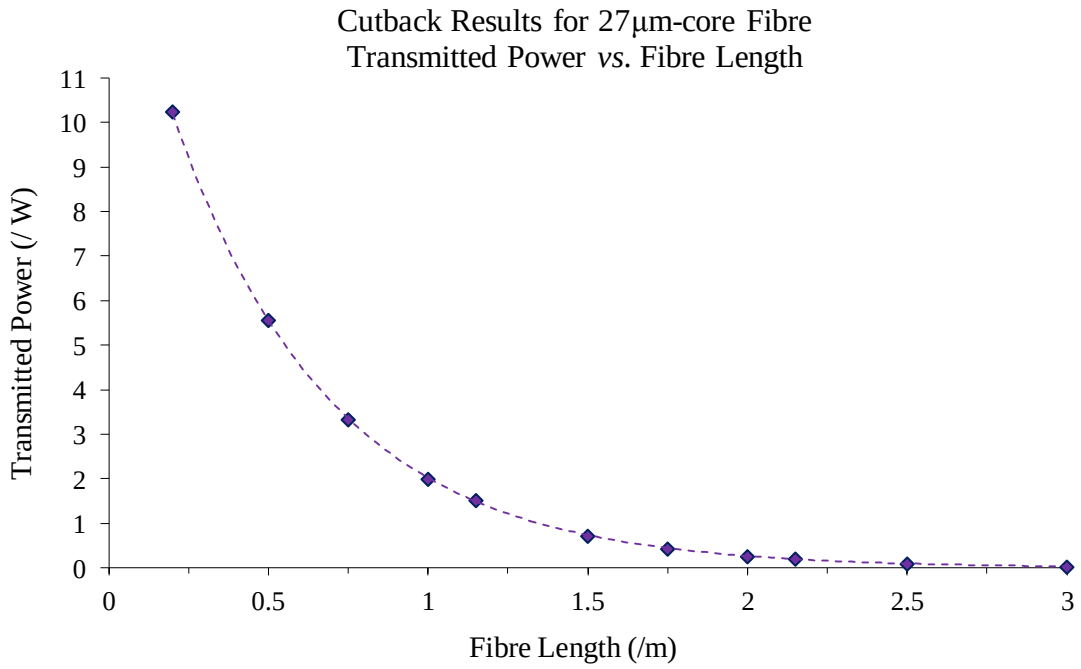

Figure 3.7 – *A plot of transmitted power as a function of length for the 27μm-core fibre with an absorption loss of 2.05 dB* m^{-1}.

The 9.6μm-core fibre was replaced in the set-up shown in Figure 3.3 by the 27μm-core fibre and the experimental procedures repeated. Sacrificing beam quality – measured M^2 parameter of 3.2 (Figure 3.8) – a minimum operating wavelength of 1.014μm could be achieved (Figure 3.9) using 1.23m of active fibre. At this extremity to the tuning range the output power was limited to only 2.1W. At the

[5] The author gratefully acknowledges Jayanta Sahu for fabricating this fibre to the author's specifications at the Optoelectronics Research Centre. Fibre code.

objective operating wavelength of 1.020µm, however, 11.9W of output was achieved with a slope efficiency of 86% (Figure 3.10). The threshold was measured to be 50mW. Although resulting in a loss of beam quality, increasing the core-cladding ratio was preferred to core-pumping a short single-mode fibre as it is less sensitive to misalignment.

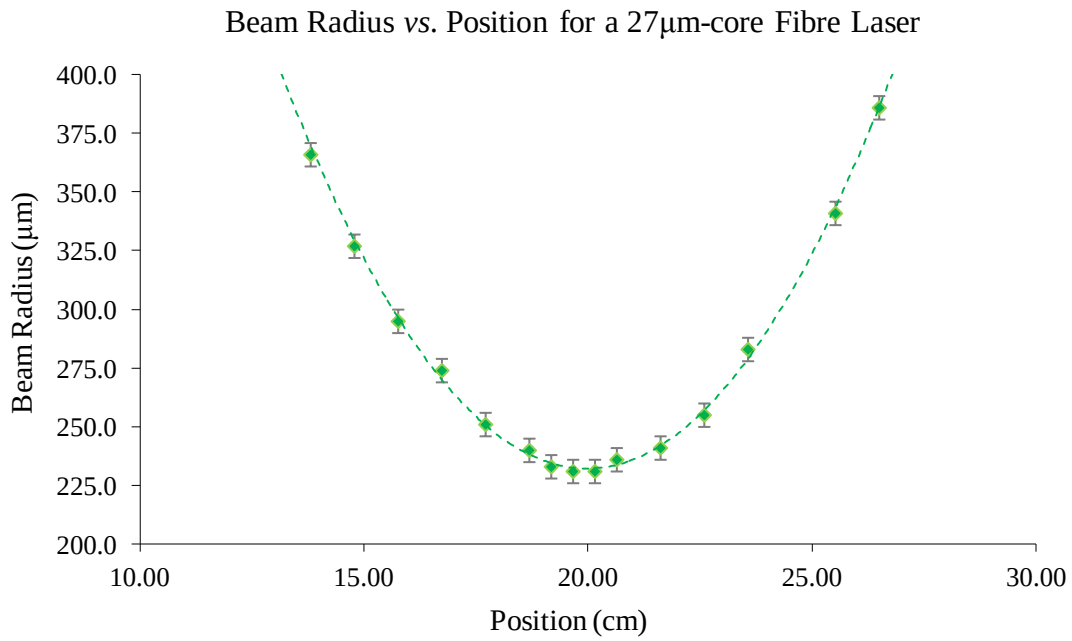

Figure 3.8 – *A plot of beam radius vs. position within the Rayleigh range for the 27µm-core fibre laser with* $M^2 = 3.2$. *The ±5µm uncertainty corresponds to fluctuations in the beam radius measured using a two-slit beam profiler.*

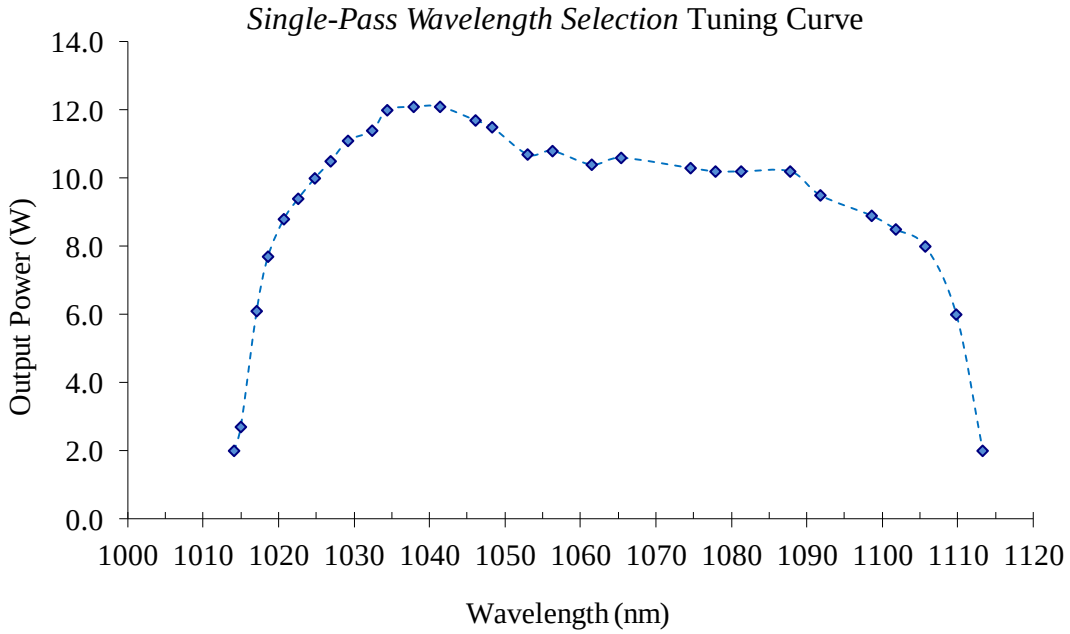

Figure 3.9 – *Tuning curve for a 1.23m, 27μm-core fibre laser with single-pass diffraction grating wavelength selection.*

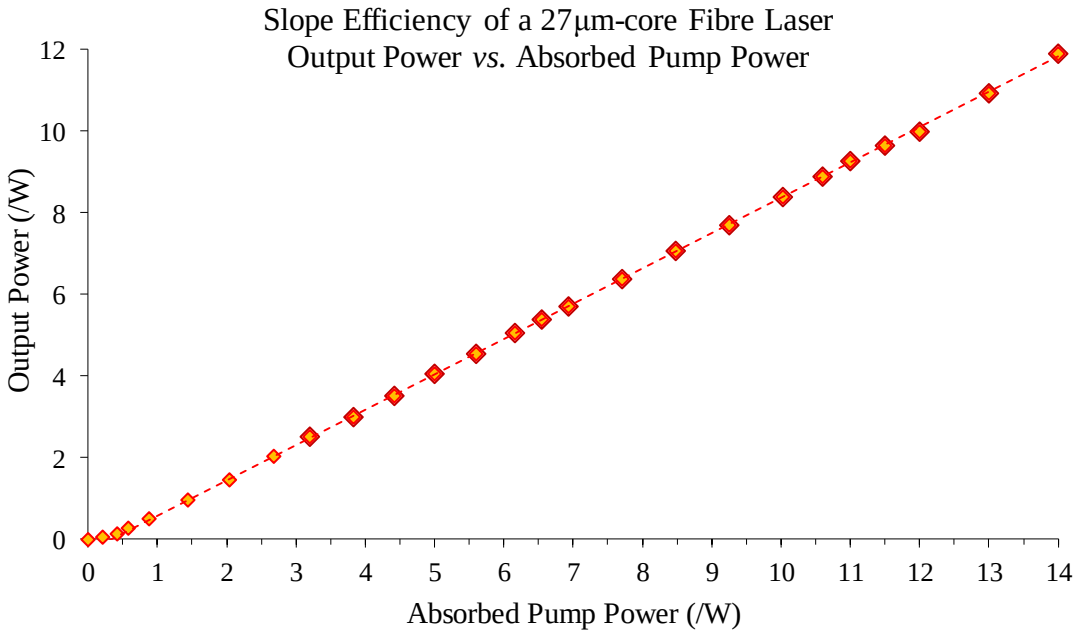

Figure 3.10 – *A plot of laser output power as a function of absorbed pump power for the 27μm-core fibre laser with a slope efficiency of 86%.*

Two attempts were made to improve the measured 99nm tuning range. The first was to introduce a high reflector at the back end of the resonator to double-pass the diffraction grating per round trip (Figure 3.11). The double-pass configuration narrowed the laser linewidth, however the tuning range was slightly reduced. This was attributed to the increased cavity losses. The second approach was to replace the diffraction grating in the double-pass configuration with a volume Bragg grating (VBG) specified[6] at 1.032µm purchased from *Optigrate*. The double-pass configuration was required as a VBG will only retro-reflect at the specified wavelength. The combination of narrow linewidth selection and high reflectivity offered by VBGs allowed wavelengths as low as 1.010µm to be reached, however the VBG was specified at 1.032µm severely restricting the maximum operating wavelength.

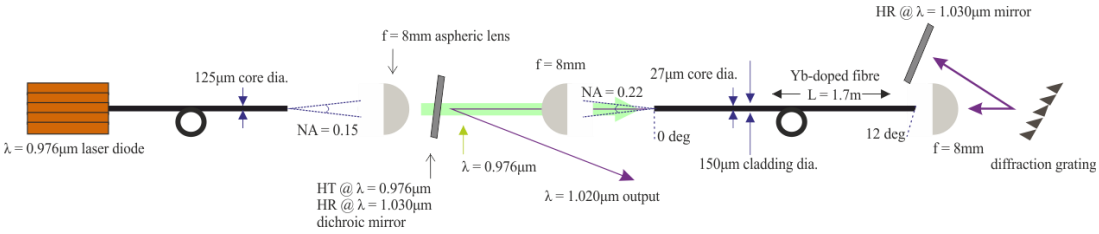

Figure 3.11 – *Schematic of a tuneable 1µm fibre laser based on a 27µm-core, 150µm-inner-cladding Yb-doped fibre gain medium with an external feedback cavity including a diffraction grating for wavelength selection in a 'double-pass' configuration.*

Although the various resonator configurations using the 27µm-core fibre satisfied the 1.020µm wavelength requirement for pumping Yb^{3+}:YAG, this fibre was highly prone to catastrophic damage by self-pulsing. Given the nature of self-pulsing it is difficult to define the stability of the lasers built using this fibre. Catastrophic damage could occur within seconds or useful operation could be maintained for up to

[6] The specified wavelength for a VBG is the reflected wavelength at normal incidence, i.e. the longest wavelength that can be reflected by a VBG.

3 hours. To perform repeatable cooling experiments without losing considerable time re-polishing fibres and characterizing the laser, the self-pulsing issues had to be resolved. As self-pulsing is very specific to individual optical fibres – sometimes to the extent that it varies over a single spool – an expedient approach was to use a fibre shown not to demonstrate significant self-pulsing behaviour for seeding an amplifier; this approach is discussed in Section 3.2.2. Alternatively self-pulsing could be directly suppressed with the cavity designs discussed in Section 3.2.3.

3.2.2 Seed-Amplifier Pump Source

As an interim solution to self-pulsing, a laser based on the 9.6μm-core fibre was used to build a low power 1.032μm[7] seed source (Figure 3.12). Limiting the seed power was intended to reduce the probability of catastrophic pulsing. The pump configuration and output coupling remained as described in Section 3.2.1, however a VBG at normal incidence was used to maximize feedback and provide narrow linewidth wavelength selection at the back end. This set-up was not tuneable in an attempt to remove possible causes of instability (i.e. potential triggers for self-pulsing). A 1.75m length of the 27μm-core fibre was used as a single-pass amplifier. Both ends of the 27μm-core had 12^{o} angle-polished facets in order to ensure that it could not act as a resonator (thereby introducing the risk of self-pulsing). The seed, separated from the pump source by means of the dichroic mirror, was focused into the 27μm-core fibre using an 8mm focal length aspheric lens. The higher NA and larger area of the 27μm-core fibre (0.22 cf. 0.075) would allow a good coupling efficiency to be achieved between the seed and the amplifier. The amplifier was pumped from the opposite end to the seed input using a *Unique Mode* 0.976μm 200μm-core, 0.15 NA fibre-coupled diode[8]. The output from the diode pump source was collimated using an 8mm focal length aspheric lens and focused into the gain medium with an identical lens. A dichroic mirror with high transmission at 0.976μm

[7] The optimum pumping wavelength for Yb^{3+}:YAG is 1.030μm.

[8] model: UM254-200-20-976

and high reflectivity at 1.030µm was situated between these lenses for separation of the amplified signal from the counter-propagating pump light.

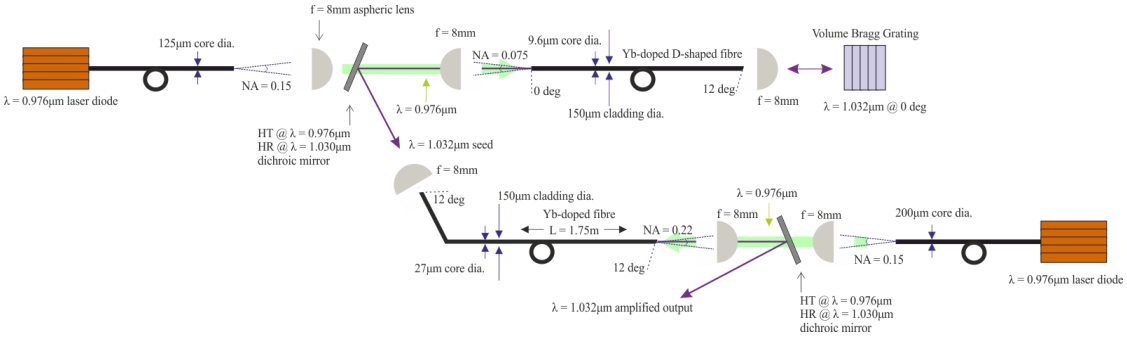

Figure 3.12 – *Schematic of a seed-amplifier pump source based on a 9.6µm-core low power seed laser with an external feedback cavity including a VBG for 1.032µm wavelength selection coupled into a 27µm-core single-pass fibre amplifier.*

For 273mW of 1.032µm seed coupled with 81% efficiency into the amplifier, 7.4W of 1.032µm output could be achieved with a slope efficiency of 87% (Figure 3.13). Applying the same methodology as described in Section 3.2.1, the M^2 parameter of the seed-amplifier pump source was measured to be 3.5 (Figure 3.14). The 0.8nm linewidth of the seed source was preserved through the amplifier with little ASE background being introduced (Figure 3.15) in a temporally stable output. This output was suitable for use a pump source in optical cooling experiments.

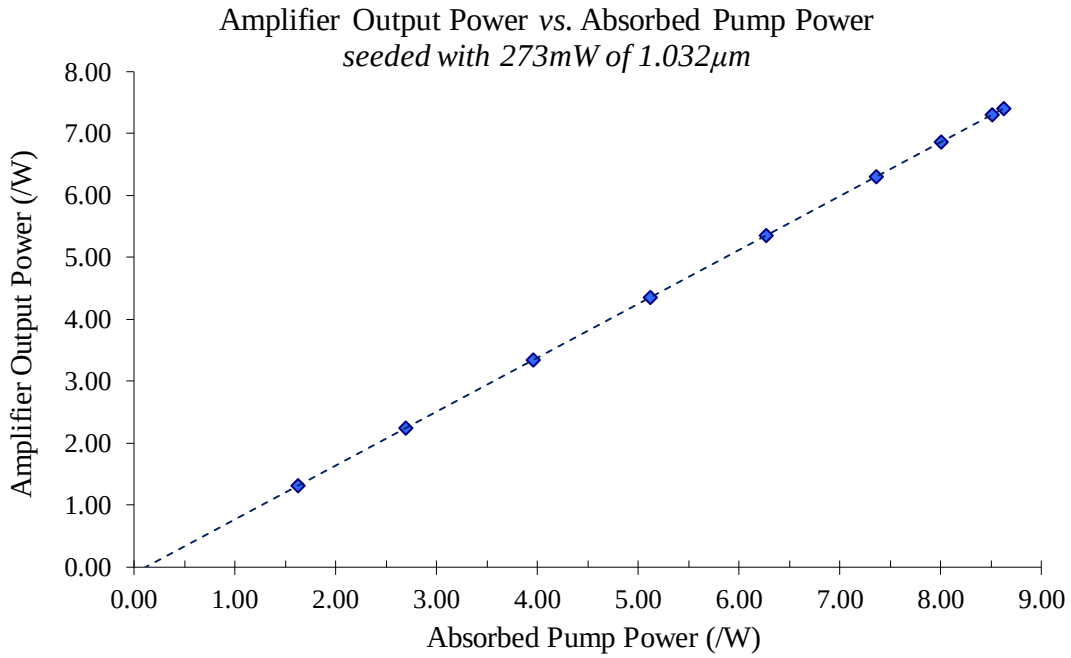

Figure 3.13 – *A plot of amplifier output power as a function of absorbed pump power for the seed-amplifier pump source seeded with 273mW of 1.032μm output from the 9.6μm-core fibre laser with an amplifier slope efficiency of 87%. The 'bunching' of points at increasing power is due to the roll-off in output of the diode pump source with measurements taken at fixed current intervals.*

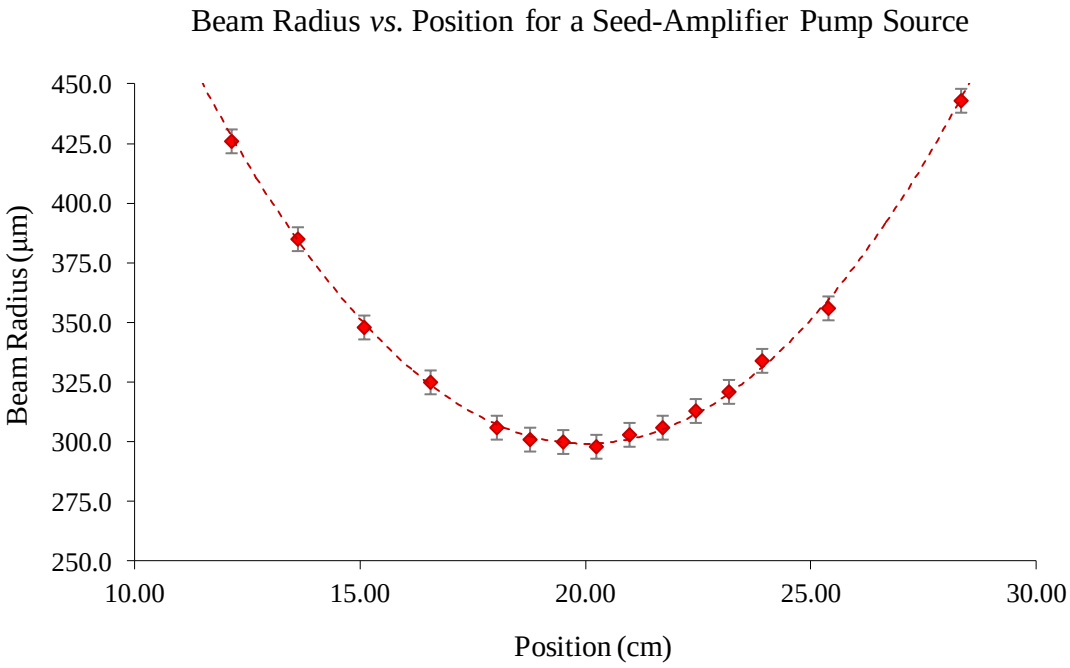

Figure 3.14 – *A plot of beam radius vs. position within the Rayleigh range for the seed-amplifier pump source with M^2 = 3.5. The ±5µm uncertainty corresponds to fluctuations in the beam radius measured using a two-slit beam profiler.*

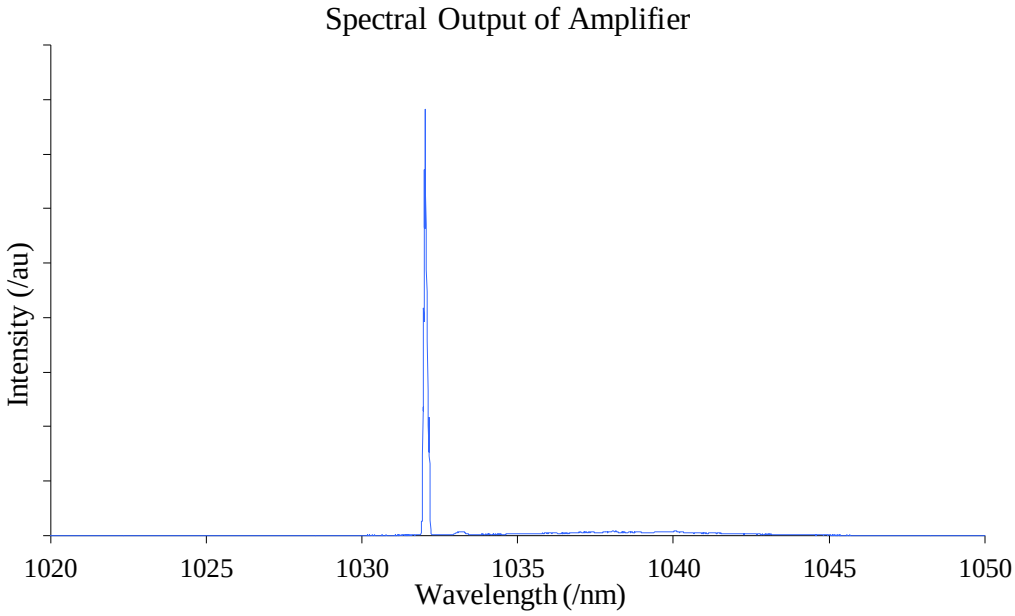

Figure 3.15 – *The spectral output from the amplifier operated at 7.4W when seeded with 273mW of 1.032µm output from the 9.6µm-core fibre laser.*

3.2.3 Self-Pulsing in Fibre Lasers

Self-pulsing is a common problem in rare-earth-doped fibre lasers. It is the phenomenon that a fibre laser can, without apparent external influence, start operating in a pulsed mode. Self-pulsing behaviour divides into two categories: sustained self-pulsing (SSP) and self mode-locking (SML). The theoretical analysis performed by Brunet *et al.* [95] shows that SSP is associated with relaxation oscillations [96], however the precise mechanism by which it is triggered remains a topic of debate. The work by Fontana *et al.* [97] demonstrates that SSP is exacerbated by a short cavity photon lifetime. The findings of Guan & Marciante [98] have shown that extending the cavity photon lifetime by using a long cavity can therefore be used as a self-pulsing suppression mechanism. Brunet *et al.* postulate that the SSP peak powers can trigger stimulated Brillouin scattering (SBS) which combines with the underlying SSP to give intense irregular pulses [99-101] that may reach the threshold for stimulated Raman scattering (SRS) and cause catastrophic damage to a fibre gain medium. SML is a term that is broadly applied to cover pulses triggered by saturation gain [102] that are directly related to the cavity photon round-trip time. Although more commonly observed at higher pump powers than for SSP [98], SML can also be observed close to the lasing threshold [95].

To investigate self-pulsing, a 1m length of the 27μm-core, 150μm-inner-cladding Yb-doped double-clad fibre (highly prone to pulsing) was used as the gain medium in a simple fibre laser (Figure 3.16). Lasing was achieved using 4% Fresnel reflection at the pumped end of the fibre and a retro-reflecting diffraction grating for wavelength selection at the other. The back end of the fibre was angle-polished at 12^{o} to prevent parasitic lasing from the facet. Pumping the fibre using the 125μm-core fibre coupled 0.976μm laser diode, the laser was operated at 1.040μm and pumped close to its threshold power of 50mW found from relaxation oscillations as described in Section 3.2.1. Based on the author's experience in developing the 1.020μm pump source, these operating conditions were predicted to promote self-pulsing behaviour. The front end output was collimated using an 8mm focal length aspheric lens and separated from the pump using a dichroic mirror having high transmission at 0.976μm and high reflectivity at 1.030μm. The temporal stability of the laser output

was monitored using a nanosecond rise time silicon photodiode detector and digital oscilloscope (Figure 3.17).

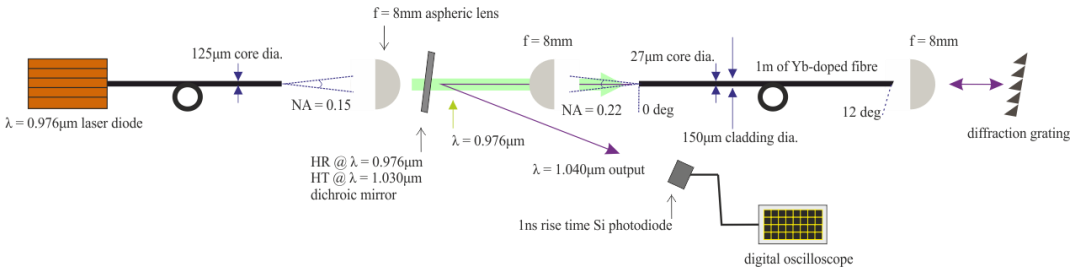

Figure 3.16 – *Schematic of the 1.040µm fibre laser used for the investigation of self-pulsing. The laser is based around a 27µm-core, 150µm-inner-cladding Yb-doped fibre gain medium with an external feedback cavity including a retro-reflecting diffraction grating for wavelength selection.*

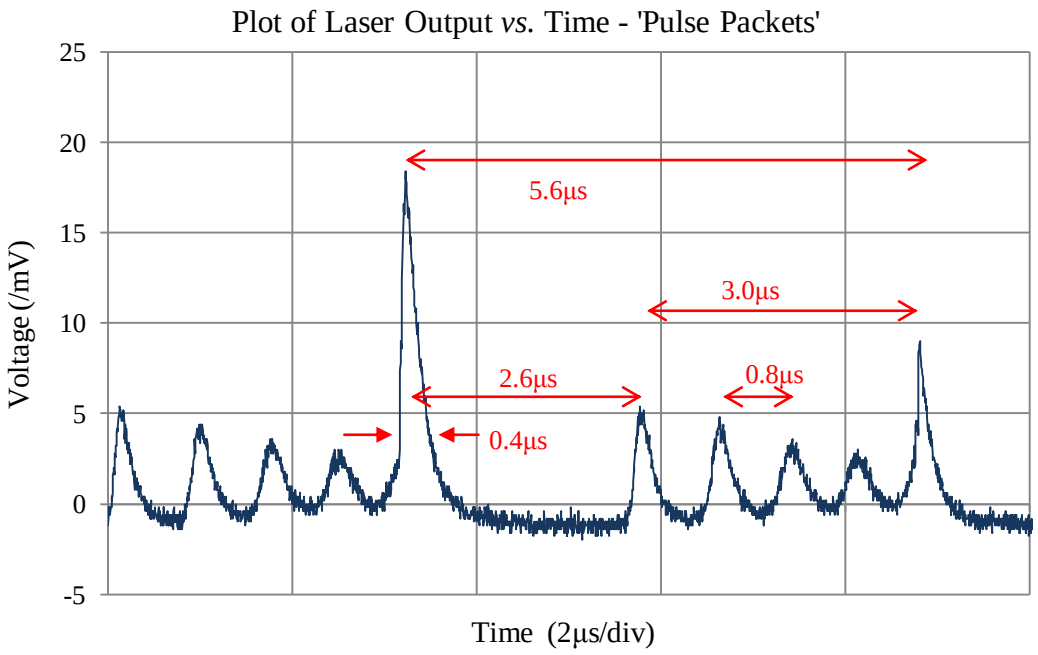

Figure 3.17 – *Self-pulsing 'packets' in the fibre laser based around a 1m length of 27µm-core Yb-doped fibre gain medium and pumped close to the lasing threshold. The spacing between consecutive pulses, consecutive 'pulse packets' and the width of the 'high power' pulse are shown.*

Figure 3.17 clearly shows that there is self-pulsing in the fibre laser. There is a repeated pattern of 4 small pulses followed by a single high (approximately ×2 relative power) pulse. From the trace it is apparent that not all these 'packets' have the same power. This offers a possible explanation as to why catastrophic damage is not necessarily immediate or always observed. As self-pulsing behaviour is first observed in this system close to the threshold power, from the literature discussed above it may be concluded that SSP rather than SML is the dominant self-pulsing effect. This conclusion is supported by observing that when a temporally stable output can be achieved above the lasing threshold, self-pulsing behaviour is not initiated unless the pump power is brought down close to the threshold, i.e. the powers for which the relaxation oscillations with which SSP is associated are once

more reached. Although the 5-peak ‘pulse packets’ are a recurrent feature of the self-pulsing observed in this fibre, Figure 3.18 shows that irregular self-pulsing may also be observed.

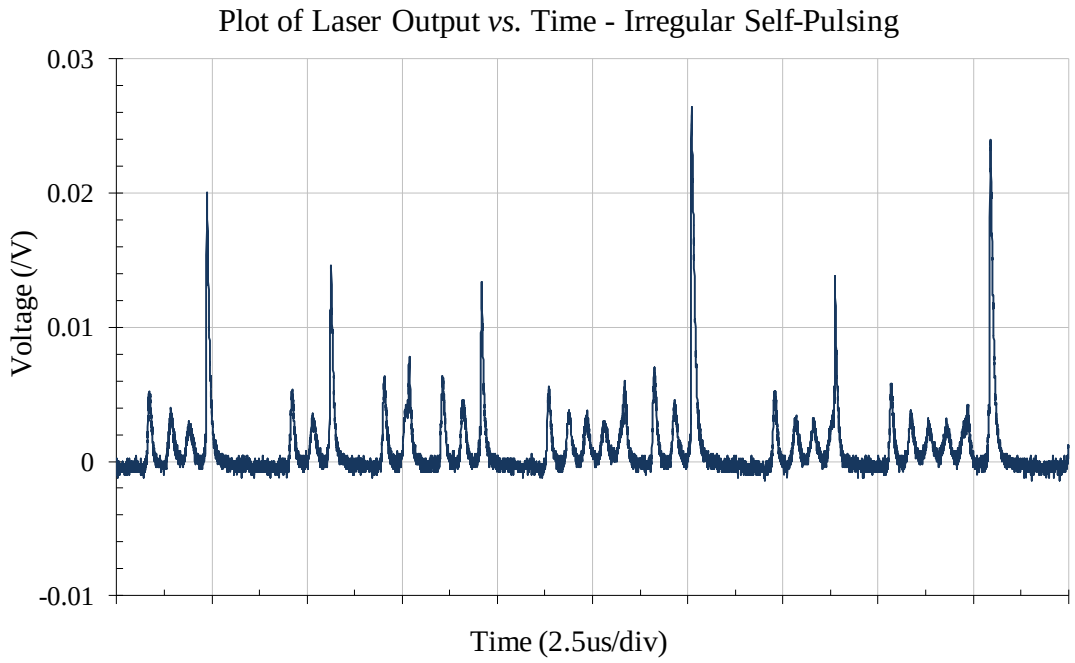

Figure 3.18 – *Irregular self-pulsing in the fibre laser based around a 1m length of 27μm-core Yb-doped fibre gain medium and pumped close to the lasing threshold.*

3.2.4 Suppression of Self-Pulsing

The build-up of SSP is described by the interaction of the photon and inversion populations (field and gain), even though the exact trigger mechanism(/s) remains disputed. Changing the relaxation oscillation dynamics, i.e. the interaction between the field and the gain), thus impacts on the SSP build-up. Various techniques for changing the relaxation oscillation dynamics to suppress self-pulsing have therefore been extensively explored. Mizrahi *et al.* [103] used active electronic feedback to the pump source, adjusting the gain and phase to minimize the relaxation oscillations. Luo & Chu [101] demonstrated that resonant pumping close to the lasing wavelength also reduces relaxation oscillations. Alternatively a semiconductor optical amplifier may be included in the laser cavity [104] to prevent signal build-up or a uni-directional ring cavity configuration adopted [105] to remove SBS as a potential trigger mechanism.

Guan & Marciante [98] demonstrated a different approach; as the frequency of relaxation oscillations f_{RO} is inversely proportional to the square root of the cavity round trip time τ_R (Equation 3.1), extending the laser cavity photon to increase the round-trip time changes the relaxation oscillation dynamics.

$$f_{RO} \approx \frac{1}{2\pi}\sqrt{\frac{LP_{cav}}{\tau_R E_{sat}}} \tag{3.2}$$

where L describes the resonator losses, P_{cav} is the intracavity power and E_{sat} is the saturation energy (i.e. the pulse energy that reduces the gain to $\frac{1}{e}$ of its original value). This technique offers the benefits of an all-fibre set-up. Various approaches for incorporating a 150m length of single-mode passive fibre into the pump laser were therefore considered for extending the cavity round-trip time by more than two orders of magnitude.

Preferring to avoid the use of free-space coupling, the first approach was to splice the 1m length of the 27μm-core active fibre used for the investigation of self-pulsing to the 5.8μm-core passive fibre. As was expected, power loss at the splice – residual

pump and stimulated emission – due to the extreme core mismatch resulted in splice damage. Free-space coupling was therefore pursued.

An 18.4mm – 4.51mm telescoping arrangement (Figure 3.19) was used to match the fundamental mode-field diameters (MFD) of the active and single-mode passive fibres found using the Marcuse formula (Equation 3.3). Matching the fundamental modes of the two fibres aimed to provide single mode operation from the multi-mode 27μm-core fibre.

$$\frac{w}{a} \approx 0.65 + \frac{1.619}{V^{3/2}} + \frac{2.879}{V^{6}} \tag{3.3}$$

where w is the mode radius, a is radius of the fibre core and the V-number is found from,

$$V = \frac{2\pi}{\lambda} a\, \phi \tag{3.4}$$

where ϕ is the numerical aperture.

As the active fibre had a NA of 0.22 and the passive fibre a NA of 0.15, the coupling efficiency in the active-to-passive direction was limited even for the case of perfect alignment. The rear end of the active fibre and both ends of the passive fibre had 12^{o} angle-polished facets to ensure that the system acted as a single laser resonator. Free-space coupling allowed the inclusion of a dichroic mirror with high transmission at 1.030μm and high reflectivity at 0.976μm to remove any residual pump light that could damage the passive fibre facet.

This set-up could be operated in two configurations: taking the laser output from the active fibre or taking the laser output from the passive fibre. Taking the output from the passive fibre would have offered the benefit of optimizing beam quality, any residual higher order modes resulting from mismatch of the MFDs being stripped out before the output. As 80% of the power is generated on the second pass through the gain medium this would, however, severely limit the power. As in optical cooling applications power is much more critical than beam quality, the active fibre was selected for the output. Pumping with the 125μm-core fibre-coupled 0.976μm laser

diode, 1.030µm lasing was achieved using 4% Fresnel at the front end and a retro-reflecting diffraction grating for wavelength selection at the other. The front end output was collimated using an 8mm focal length aspheric lens and separated from the pump using a dichroic mirror having high transmission at 0.976µm and high reflectivity at 1.030µm. The output was attenuated using a series of three 10% reflecting mirrors (0.999% attenuation) and a sequence of neutral density (ND) filters. This was then viewed using a *Spiricon IEEE-1394 (LBA-FW-SCOR20)* CCD digital camera.

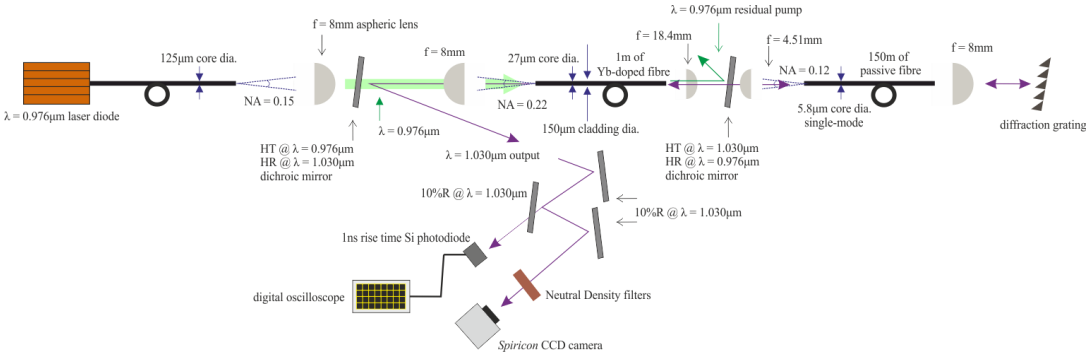

Figure 3.19 – *Schematic of a set-up for free-space coupling between a 27µm-core active fibre and 150m of single-mode 5.8µm-core passive fibre for the suppression of self-pulsing in a fibre laser. Output is monitored using a Spiricon CCD camera and a nanosecond rise time silicon photodiode.*

Good fundamental mode operation could be achieved (Figure 3.20), however this was extremely sensitive to alignment and optimum coupling would be lost within 30mins due to drift in the translation stages on which the two fibres were mounted. Thus to build a practical system a rigid set-up was pursued (see below).

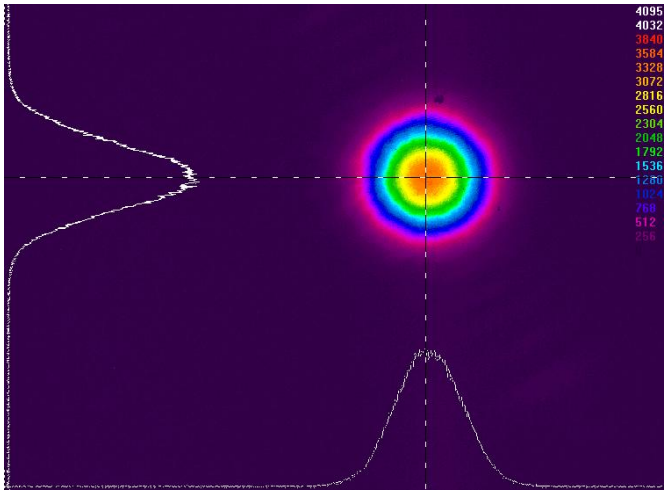

Figure 3.20 – *Fundamental mode laser output from a 27µm-core active fibre mode-matched to a 5.8µm-core passive fibre.*

To evaluate the suppression of self-pulsing, the laser output was monitored with when operating on the fundamental mode (well aligned) and when operating on higher order modes (slight misalignment). This was to ensure that the fundamental mode selection was not contributing directly to the suppression of self-pulsing. The output (Figure 3.21) was monitored continuously for 15mins and no self-pulsing behaviour was observed in either case. This work supports the published findings of Guan & Marciante [98] that self-pulsing in a fibre laser is suppressed by extending the cavity photon round-trip time so as to change the relaxation oscillation dynamics.

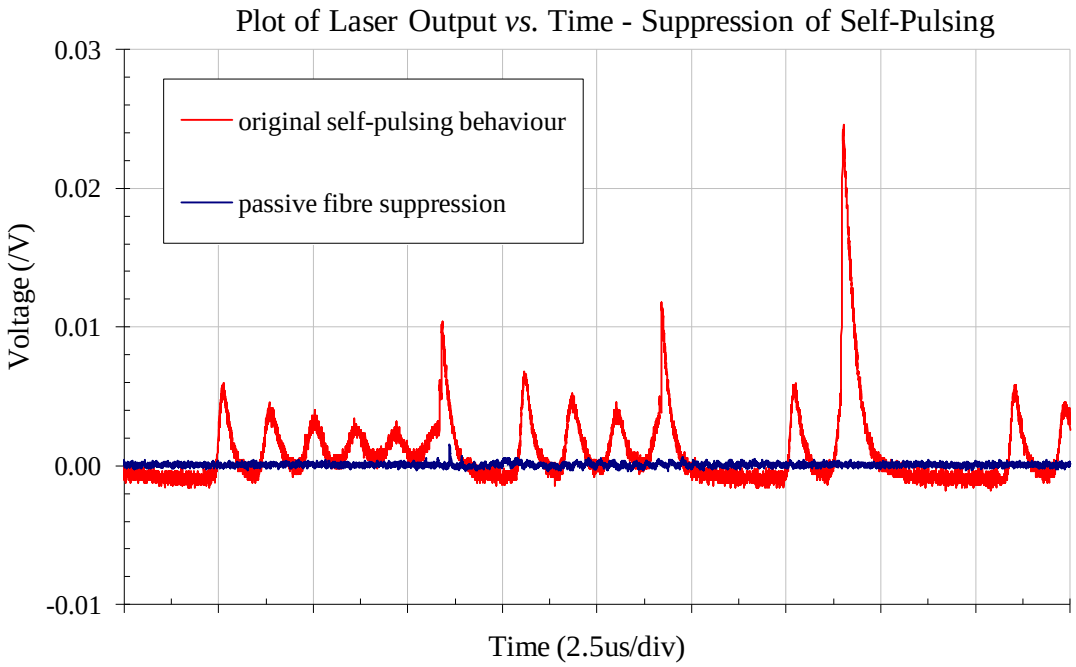

Figure 3.21 – *Suppression of self-pulsing (blue line) using a 150m length of single-mode passive fibre free-space mode-matched with a 1m length of 27μm-core active fibre. Plot shows the output of the active fibre alone for comparison (red line).*

After demonstrating the effectiveness of this approach for the suppression of self-pulsing, the project focused on building a robust set-up that would not require continuous realignment. A set-up was designed that fixed the two fibres and the 4.51mm coupling lens at their optimal positions. The position of the 18.4mm lens was then adjusted by means of a purpose built jig while the alignment was assessed by using the *Spiricon* CCD camera to view an ASE signal transmitted in the passive-to-active direction. The ASE was generated by pumping a 2m length of the 9.6μm-core, 150μm-inner-cladding Yb-doped double-clad fibre with the 125μm-core fibre-coupled 0.976μm laser diode. The back end of the 9.6μm-core fibre had a 12^{o} angle-polish to prevent lasing. The output was collimated using an 8mm focal length

aspheric lens and focused into the back[9] end of the passive fibre using an identical lens. As this was a low power source for alignment purposes only, coupling into the passive fibre did not have to be optimized, thus allowing the 1:1 telescoping arrangement. Residual pump light was removed using a dichroic mirror having high transmission at 1.030μm and high reflectivity at 0.976μm situated between the lenses. When fundamental ASE output from the active fibre was observed, the lens was fixed in place with UV-glue. Despite much time and effort being put into correcting alignment issues and ruling out other explanations, useful operation of this rigid set-up could not be achieved. The conclusion drawn is that the rigid set-up does not have sufficient degrees of freedom during assembly for effective coupling.

Having concluded that free-space coupling was not a viable option for a reliable and timely solution, a single-mode active fibre was procured which could be spliced to the passive fibre without significant loss. This fibre would be core pumped at 0.946μm which would allow even shorter fibre lengths to be used and potentially lower wavelengths to be achieved. Due to the adoption of the intracavity cooling scheme (Section 3.3) this set-up was never rigorously tested, however preliminary experiments with a 6μm-core core-pumped fibre laser employing a diffraction grating for wavelength selection showed that operating wavelengths as low as 1.004μm could be achieved at low powers. Significantly, this allowed pump wavelengths shorter than the mean fluorescence of Yb^{3+}:CaF_2 (1.008μm) to be achieved in an Yb-doped fibre laser.

[9] relative to the active-passive fibre laser

3.3 1µm Intracavity Pumping

A simple technique for the initial identification of cooling samples requires that the cooling effect should be maximized in order to clearly distinguish it from other thermal effects (e.g. ambient temperature fluctuations and uniform fluorescence reabsorption). As most crystals have extremely low absorption above their mean fluorescence wavelength, power scaling the pump source to increase the cooling power is a highly inefficient method for achieving this. Increasing the cooling efficiency (/pump wavelength) and the absorbed pump power are therefore preferred ways to improve the cooling performance. The pump development work discussed in Section 3.1 attempted to optimize cooling by employing a tuneable pump source, thereby allowing the optimum pump wavelength to be reached and maintained. To absorb more pump power one option is to use more highly doped crystals. This, however, increases the probability of ion-ion interaction and parasitic heating effects. A different approach widely used in the optical cooling community is to use various multi-pass geometries for the pump beam. This section of the thesis discusses the less commonly employed technique of intracavity pumping. The cooling experiments reported in Chapter 5 report the first application of such a pump geometry in the case that the sample and gain medium are different materials.

For intracavity (/resonant) pumping the cooling sample is placed inside a low loss pump laser cavity. In non-resonant pump schemes, selecting a pump wavelength that provides an optimal combination of absorption and cooling efficiency is critical. Equation 3.2 shows that for an intracavity pump scheme with no other cavity losses L, regardless of how small the double-pass absorption (as a fraction of the total pump power) in the crystal η_{cry} is, all of the available pump power will be absorbed in the sample:

$$\eta_{abs} = \frac{\eta_{cry}}{(\eta_{cry} + L)} \tag{3.2}$$

Thus the absorption efficiency for a lossless cavity is independent of wavelength. In practice, however, there will always be some cavity losses and the pump wavelength must be selected such that the sample absorption remains the dominant effect.

A Nd:YLF bulk laser operating at 1.047µm was selected for pumping samples in the 1µm-regime as this wavelength yields relatively high cooling efficiencies whilst the absorption coefficients for Yb^{3+}:YAG and Yb^{3+}:CaF_2 of 0.314cm^{-1} and 0.399cm^{-1} respectively are still sufficient to dominate cavity losses. Adopting an established bulk laser design, a low risk, robust source could be built (Figure 3.22). The practical dimensions of such a cavity allow for the simple exchange of samples adding to its usefulness. The high absorbed pump power negates any disadvantage that is incurred by the lack of tunability.

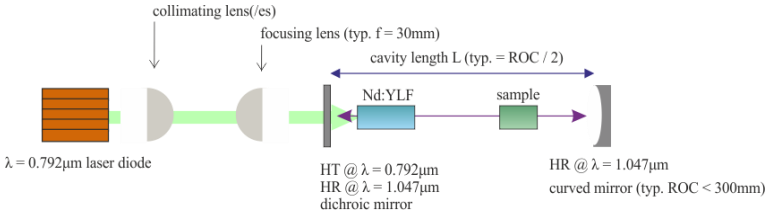

Figure 3.22 – *Schematic of a typical intracavity pump set-up based on a Nd:YLF bulk laser.*

3.4 Summary

This chapter has covered the development of two possible pump sources for optical cooling trials: a fibre-based seed-amplifier source tuneable in the range 1.010µm to 1.095µm (1.032µm with a narrow linewidth wavelength selection VBG) and a Nd:YLF 1.047µm bulk laser suitable for intracavity pumping of Yb^{3+}:YAG and Yb^{3+}:CaF_2.

To build a robust fibre laser, the issue of self-pulsing suppression was addressed by integrating a 150m length of passive fibre into the cavity. Analyzing the observed temporal behaviour, the success of this suppression technique has been verified and ‘pulse packets’ observed as a characteristic feature of self-pulsing in the 27µm-core fibre used in this work. The final design for a tuneable fibre laser with self-pulsing suppression offers a robust, power scalable source for use in future high power

1μm-regime cooling studies. The wide tuning range, power scalability and option for adopting resonance-enhanced pump schemes gives this source advantages over currently used Ti:sapphire and Yb-doped fibre laser 1μm tuneable sources.

The described Nd:YLF laser with an intracavity pump geometry employs a conventional, bulk laser design to offer stable, reliable operation while maximizing the pump absorption. Though not of novel design, the optical cooling experiments reported in Chapter 5 cover the first application of such a scheme for 1.047μm pumping of Yb-doped samples.

Chapter 4 covers the development of a novel diagnostic for temperature measurement in transparent samples. The pump sources described in this chapter are then returned to in Chapter 5 which reports their use in cooling experiments with Yb^{3+}:YAG and Yb^{3+}:CaF_2 crystals.

Chapter 4

Developing a Laser-Based Thermometer

Section 4.1 of this chapter discusses the background to various high-sensitivity temperature measurement techniques. Initial photothermal deflection studies of pumped Yb^{3+}:YAG are presented in Section 4.2. Section 4.3 covers longitudinal mode-shift relative thermometry (LMRT), a novel interferometric approach for non-contact observation of thermal effects in transparent samples.

4.1 High-Sensitivity Thermometry

High-sensitivity non-contact thermometry falls broadly into two categories: spectroscopy and techniques that are based on the temperature dependence of refractive index. Spectroscopic thermometry relies on the fact that the emission spectrum of a material has a temperature dependence. As the range of atomic energy level transitions available to an electron decrease with thermal energy in accordance with the changing Boltzmann distribution, for a well characterized sample the varying spectrum can be directly linked to an absolute temperature. This technique has been demonstrated as an effective non-contact method for continuous, high-sensitivity monitoring of temperature in optical cooling applications [29]. It is, however, limited in that it can only measure the bulk temperature of samples. The necessity to have a detailed thermo-spectroscopic characterization of each sample is another major disadvantage to this technique. A further constraint on the accuracy of this technique is placed by fluorescence trapping shifting the emission spectrum to falsely long wavelengths [31].

A simpler and more commonly used method for measuring small variations in the temperature of a medium is the photothermal deflection (PTD) technique[1] [106, 107]. This employs a low power probe beam at a wavelength that is not absorbed by the material under investigation. A position sensor is then used to measure any beam deflection caused by thermal lensing due to an induced refractive index gradient. Able to be linked with mathematical models to yield absolute temperature values, PTD has proven itself a very flexible technique whilst retaining a comparatively simple set-up. The wide range of situations to which PTD has been applied include: determining absorption coefficients [108], finding values for thermal diffusivity [109], measuring flow velocity in gases [110], temperature/beam profiling [111] and most recently for monitoring optical cooling [29, 47, 50]. In most practical situations, PTD sensitivity is limited by the spatial resolution of available position sensors. Although it improves on spectroscopic thermometry by allowing local thermal effects to be measured, PTD is disadvantaged in that to experience a refractive index gradient the probe beam cannot be collinear with the pump. It is therefore particularly sensitive to non-uniform thermal effects elsewhere in a sample. Section 4.2 discusses in detail the theory of PTD and the results obtained for an Yb^{3+}:YAG rod in an optical cooling set-up.

Interferometric techniques also rely on the temperature-dependence of refractive index and can be used to obtain greater temperature resolution than is offered by PTD. Interferometry offers the added advantage that both local and collinear temperature measurements can be obtained. The high precision offered by two-beam interferometry has been used to find various thermal coefficients [112, 113] and in a Mach-Zehnder[2] configuration applied to optical cooling [53]. Section 4.3 of this chapter covers the theory, development and evaluation of a laser-based technique for measuring temperature changes along any path within a transparent sample to interferometric precision without the complexity of a conventional two-beam interferometer.

[1] This is sometimes referred to as ‘beam deflection’ or ‘optical beam deflection’.

[2] A two beam interferometer in which one beam is shone through the sample and the other through an equal distance of free space.

4.2 Photothermal Deflection Technique

Prior to developing a new technique for temperature measurement, the established PTD method was trialled to enable a comparison to be drawn. This section outlines the theory behind PTD and reports a preliminary PTD investigation of optical cooling in Yb^{3+}:YAG.

4.2.1 Theory of Photothermal Deflection

The temperature profile in a long cylindrically symmetric sample of length L_c and radius r_0 that is pumped along its centre by a beam of radius w_p (i.e. assumption of radial heat flow only) is described by the function:

$$T(r,z) = \left[\frac{P_h \cdot \alpha \cdot e^{-\alpha z}}{4\pi K_c(1-e^{-\alpha z})}\right] \times \left[\left\{\left(1-\frac{r^2}{w_p^2}\right)+\ln\left(\frac{r_0^2}{w_p^2}\right)\right\}\Theta\left(r^2-w_p^2\right)+\ln\left(\frac{r_0^2}{r^2}\right)\Theta\left(w_p^2-r^2\right)\right] \quad (4.1)$$

where P_h is the incident heating power, α is the absorption coefficient, K_c is the thermal conductivity and $\Theta(R)$ is the Heaviside step function[3]. Equation 4.1 describes a temperature profile (Figure 4.1) that is hyperbolic within the pumped region and has a logarithmic fall-off outside this region.

[3] The Heaviside step function is defined as:

- $\Theta(R) = 1$ when $R < 1$
- $\Theta(R) = 0$ when $R \geq 1$
- $\frac{d}{dR}\Theta(R) = \delta(R)$ the Dirac delta function.

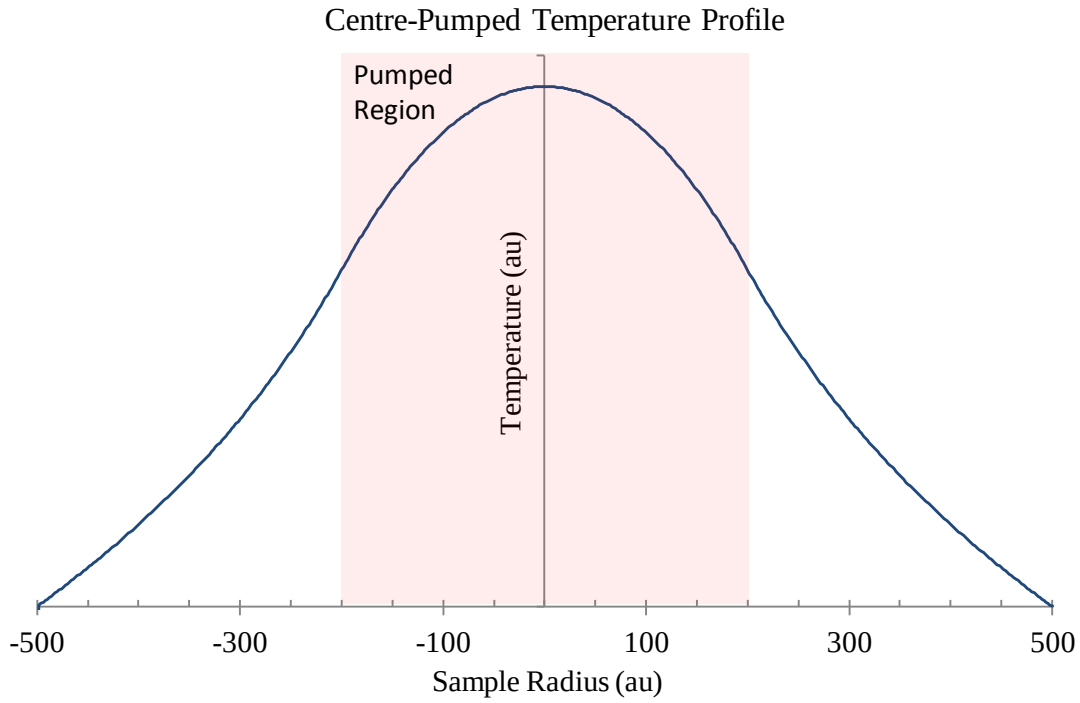

Figure 4.1 – *Temperature profile in a centre-pumped cylindrically symmetric sample.*

The temperature gradient outside the pumped region is therefore given by:

$$\frac{dT}{dr} = \frac{-1}{r} \times \left(\frac{P_h \cdot \alpha \cdot e^{-\alpha z}}{4\pi K_c (1 - e^{-\alpha z})} \right) = \frac{-2A}{r} \tag{4.2}$$

and a thermal lensing effect will arise due to the radial dependence of refractive index (/effective sample length):

$$n(r) = L_c \times (n_0 + \frac{2A}{r} \frac{dn}{dT}) \tag{4.3}$$

where the thermo-optic coefficient $\frac{dn}{dT}$ describes the temperature dependence of refractive index.

Defining the heating power as:

$$P_h = P_{in} \times \frac{\lambda_P}{\lambda_{fl}} \tag{4.4}$$

where P_{in} is the incident pump power, λ_P is the pump wavelength and λ_{fl} is the mean fluorescence wavelength, the focusing effect f_g at radial position s is described by:

$$f_g = \frac{2\pi K_c\, s^2}{P_h e^{-\alpha z} \frac{dn}{dT}} \tag{4.5}$$

leading to a linear beam deflection Δx given by:

$$\Delta x = -\frac{sl}{f_g} \tag{4.6}$$

where s is now defined as the radial separation between the pump and the probe beams and l is the linear distance between the thermal lens and the monitoring plane.

4.2.2 Measurements of Photothermal Deflection

For PTD measurements a *Thorlabs* single-mode, well collimated, narrow beam 17mW HeNe laser[4] was co-propagated through the sample with the 1.032μm output from the seed-amplifier pump source described in Section 3.2.2 (Figure 4.2). The two beams were combined and separated by means of dichroic mirrors having high reflectivity at 0.633μm and high transmission at 1.030μm for a 45^o incident angle. An additional alignment mirror having high reflectivity at 0.633μm for a 45^o incident angle was mounted on a translation stage and used to introduce a 1mm centre-centre radial offset in the path of the HeNe relative to the pump. Performing this procedure, between the dichroic mirrors the probe beam propagated parallel to and outside of the pumped region. The final position of the probe beam was monitored continuously using the twin-slit *DataRay Inc. Beamscope*^{TM} *P7* beam profiler that had a linear displacement tracking function. The bulk temperature of the Yb^{3+}:YAG sample was measured using a thermocouple immediately before and after pumping. The thermocouple was removed during pumping to avoid fluorescence absorption which would lead to falsely high temperature measurements and could possibly be a source of parasitic heating at the point of contact with the sample. The assumption that there is a linear relationship between Δx and ΔT was then applied for a basic calibration (Figure 4.4). Low-level fluorescence reabsorption within the sample was assumed to be a uniform heating effect, not contributing to the temperature gradient in the sample. PTD is therefore a measurement technique that is insensitive to low-level fluorescence reabsorption parasitic heating effects.

[4] model: HNL170R

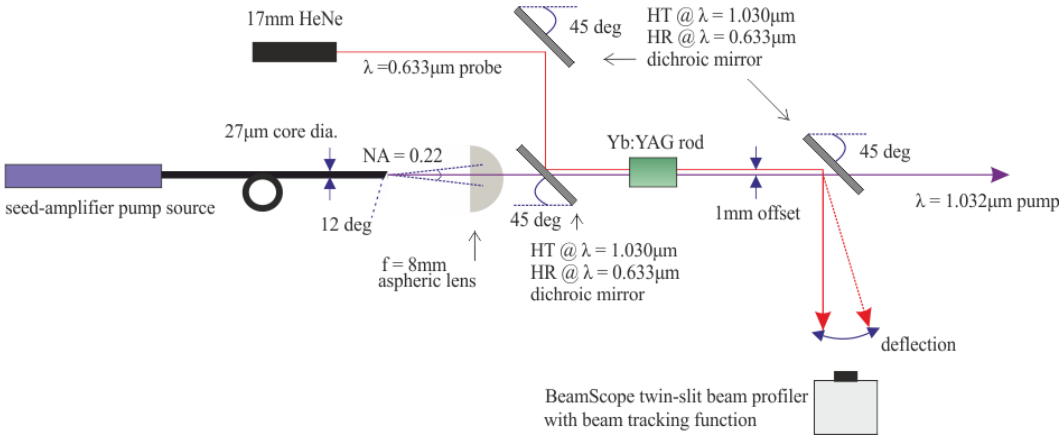

Figure 4.2 – *Schematic of an experimental set-up for photothermal deflection measurement of temperature in an optically cooled sample.*

A *Scientific Materials Corp.* 5%-doped 3mm × 5mm Yb^{3+}:YAG laser rod was pumped at 1.032μm for 5 minutes in a single-pass configuration. The sample absorbed 912mW of the 6W incident pump corresponding to a measured absorption coefficient of $0.97cm^{-1}$. The sample was cleaned in an ultrasonic bath in order to remove any surface contamination. The sample was then mounted on two supports made from crossed microscope cover-slips (Figure 4.3) in order to minimize thermal contact with its surroundings. The sample was not pumped *in vacuo* as convective heat transfer would only limit the net cooling and not mask the local temperature gradient being probed in these preliminary experiments.

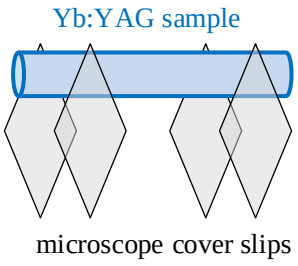

Figure 4.3 – *Low thermal contact sample mount.*

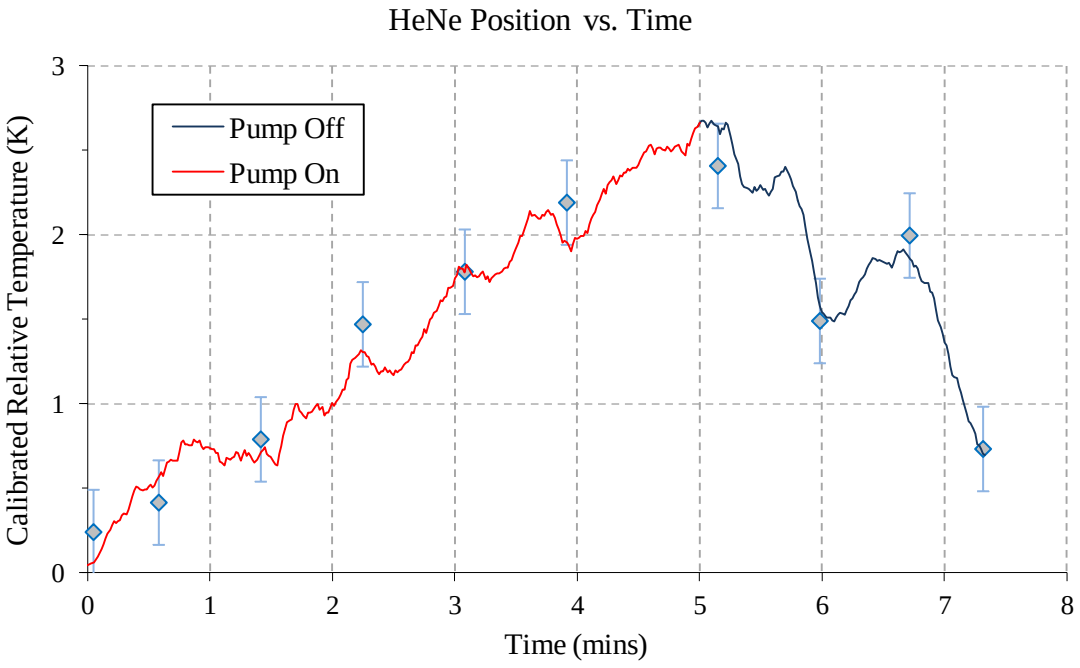

Figure 4.4 – *Photothermal deflection measurement of temperature in Yb^{3+}:YAG pumped at 1.032μm using a seed-amplifier source. Presented temperature values are found by calibrating deflection data using a thermocouple. Solid line shows 3× averaged data with typical data points shown for clarity. Error bars show the ±0.25K jitter-limited resolution of the PTD technique.*

Figure 4.4 shows approximately linear heating in the Yb^{3+}:YAG sample during pumping. The relative temperature increase measured using the thermocouple was 2.7±0.05K followed by a three-minute drop-off during which pronounced ambient temperature fluctuations were more noticeable. The poor jitter-limited resolution to PTD of ±0.25K is calculated from two standard deviations in the spread of the measured beam positions at a fixed temperature. Repeating the experiment for various pump periods between 3→5 minutes, the observed temperature rises were all consistent with the PTD monitored heating being linear over this five minute pump duration.

4.3 Longitudinal Mode-Shift Relative Thermometry

This section covers the development of a more sensitive technique than PTD for interferometric non-contact temperature measurement. The LMRT diagnostic technique improves on PTD in that it can directly measure the relative temperature within the pumped region of a sample. Such an approach offers the ability to prove conclusively whether there is a cooling effect in the pumped region even if the net temperature of the sample increases due to fluorescence reabsorption or other parasitic heating effects.

The first concept solution to be explored in developing this diagnostic was a two-beam temperature-gradient interferometer (TGI). This would have provided the required precision and the ability to measure temperature changes along the path of the pump beam. It would improve upon the conventional Mach-Zehnder interferometer by being independent of variations in the ambient temperature (both beams travelling equal free space and sample distances). Importantly the TGI would yield values for cooling power that were not susceptible to uniform fluorescence reabsorption in the sample. A second approach – discussed in this section of the thesis – was preferred as a simpler, more robust set-up.

The LMRT technique developed in this work uses a scanning Fabry-Pérot interferometer to monitor continuously the longitudinal modes of a bulk laser inside which a sample is placed. Any change in the temperature of the sample will result in a change in the effective cavity length (Figure 4.5). Thus there will be a shift in the longitudinal modes supported by the probe resonator. This mode-shift and its directionality can be related to the change in temperature and thus used as diagnostic for continuous monitoring of the relative temperature in a sample. LMRT therefore provides measurements of temperature to interferometric precision without the complexity of splitting and recombining the probe beams as in conventional interferometry. The linewidth of a single-frequency bulk laser is proportional to the square of the bandwidth of the cavity resonances[5]. Thus observing individual longitudinal modes offers greatly improved resolution.

[5] This is sometimes referred to as the ‘resonator bandwidth’.

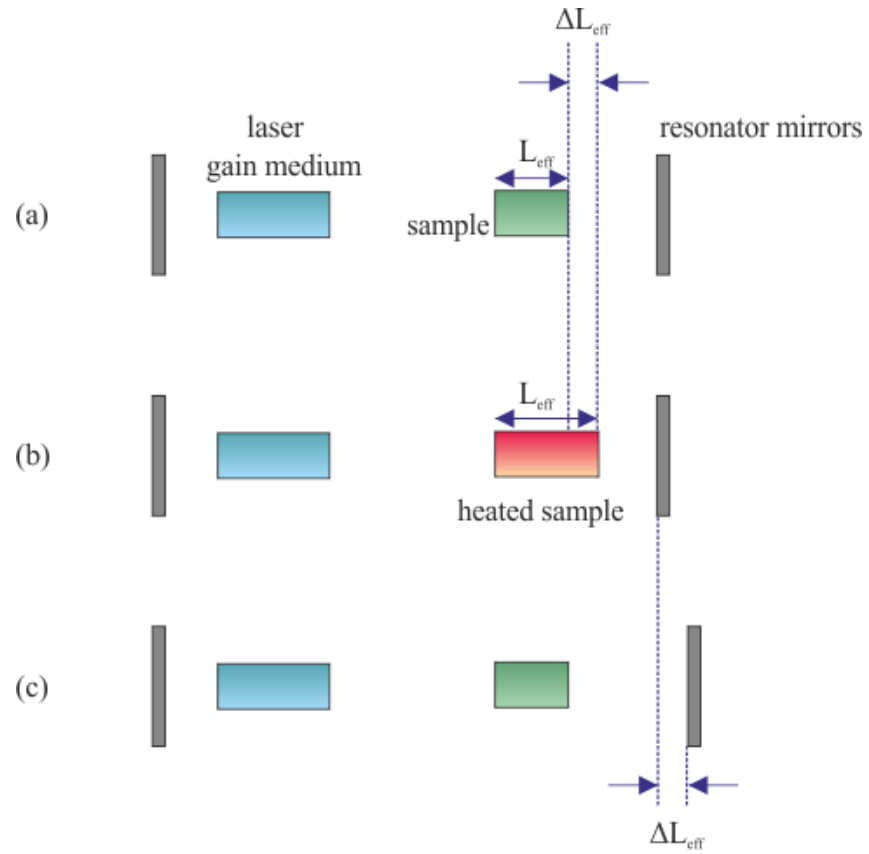

Figure 4.5 – *Diagram showing the principles involved in longitudinal mode-shift relative thermometry; (a) a probe cavity at the initial temperature, (b) a probe cavity for a heated sample and (c) a cavity equivalent to that for a heated sample showing the change in effective resonator length.*

To avoid parasitic heating, the probe laser must be selected to operate at a wavelength for which there is negligible sample absorption. In the event that intracavity pumping of the sample is to be used, the probe resonator should be overlapped with the pump by means of a dichroic or a polarizer. The longitudinal modes of the pump laser should not be monitored as the initial thermal expansion of the gain medium will dominate the mode-shift and falsify the data.

4.3.1 Theory

Frequency shifting due to thermal expansion of a fibre laser gain medium is used in the latest generation of sensors for high sensitivity thermometry [114-116]. It has not, however, been reported as a technique for measuring the internal temperature of samples. This section of the report covers the theory behind a novel laser based technique for continuous high-sensitivity relative temperature measurement by monitoring longitudinal mode-shift in a laser cavity. This allows any path within a transparent sample to be measured to interferometric precision while retaining a comparatively simple and robust probe configuration.

Measurement of Relative Temperature

There are three contributions to the change in optical pathlength of a sample that is subjected to a temperature change ΔT. A contribution due to the dependence on temperature of refractive index ΔL_n (Equation 4.7) and two contributions – stress-induced birefringence, physical elongation – due to thermal expansion ΔL_T (Equation 4.8). For a cylindrically-symmetric core-pumped sample of length l:

$$\Delta L_n = l \times \frac{dn}{dT} \times \Delta T \tag{4.7}$$

$$\Delta L_T = \left[-\frac{\alpha \cdot c_x'' \cdot n_0^3}{48(1-v)} + \frac{2(n_0 - 1) \cdot \alpha \cdot 2s}{l} \right] \times \Delta T \tag{4.8}$$

where α is the thermal expansion coefficient, c_x'' is a stress-related coefficient [85], n_0 is the original refractive index, v is Poisson's ratio and s is the length over which significant thermal elongation of the rod occurs (~twice rod diameter). The latter term in ΔL_T relates to end-face bulging and over the limited temperature changes for which this technique is most useful dominates the net volume expansion of a sample. Equations 4.7 and 4.8 can be rearranged and combined to give a thorough expression for the change in temperature as a function of the effective length ΔL_{eff}:

$$\Delta T = \frac{\Delta L_{eff}}{\left[l \cdot \frac{dn}{dT} - \frac{\alpha \cdot c_x'' \cdot n_0^3}{48(1-\upsilon)} + \frac{2(n_0-1)\cdot\alpha\cdot 2s}{l}\right]} \tag{4.9}$$

The resonance condition for longitudinal modes of wavelength λ in a cavity of length L_{eff} is:

$$L_{eff} = q\frac{\lambda}{2} \tag{4.10}$$

where q is an integer.

As the theoretical axial mode spacing $\Delta\lambda$ in terms of wavelength is given by:

$$\Delta\lambda = \frac{\lambda^2}{2L_{eff}} \tag{4.11}$$

Monitoring a shift in the longitudinal modes $\delta\lambda$ as a fraction of the axial mode spacing the change in effective length can be calculated:

$$\Delta L_{eff} = \frac{\delta\lambda}{\Delta\lambda} \times \frac{\lambda}{2} \tag{4.12}$$

Substituting Equation 4.12 into 4.9, the change in temperature in terms of the fractional mode shift is then given by:

$$\Delta T = \frac{\left[\frac{\delta\lambda}{\Delta\lambda} \cdot \frac{\lambda}{2}\right]}{\left[l \cdot \frac{dn}{dT} - \frac{\alpha \cdot c_x'' \cdot n_0^3}{48(1-\upsilon)} + \frac{2(n_0-1)\cdot\alpha\cdot 2s}{l}\right]} \tag{4.13}$$

To be accurately resolvable, the mode-shift $\delta\lambda$ should be greater than the linewidth[6] Δw of the modes after taking into account the uncertainty due to noise. For a perfectly isolated (noiseless) system, the linewidth $\Delta\lambda_{LW}$ from the Schawlow-Townes equation and thus the resolution of the LMRT diagnostic is related to the probe cavity finesse F by:

$$\Delta\lambda_{LW} = \frac{\pi hc^2\lambda}{4m^2L_{eff}^2F^2P_{PL}} \tag{4.14}$$

where m = 1 for a plane-plane cavity and m = 2 for a plano-concave cavity and P_{PL} is the output power of the probe laser assuming no resonator losses.

Combining Equations 4.13 and 4.14, the ideal temperature resolution δT of this technique is thus given by:

$$\delta T = \frac{\left[\frac{\pi hc^2}{4mLF^2P_{PL}}\right]}{\left[l\cdot\frac{dn}{dT} - \frac{\alpha\cdot c_x''\cdot n_0^3}{48(1-\upsilon)} + \frac{2(n_0-1)\cdot\alpha\cdot 2s}{l}\right]} \tag{4.15}$$

This technique employs two resonators: a laser 'probe' resonator in which the sample is placed and a scanning Fabry-Pérot monitoring resonator. For a typical probe cavity with 1% output coupling a finesse of >600 could reasonably be achieved. This compares to a typical finesse of >1000 for current commercially available scanning Fabry-Pérot interferometers. However, as the linewidth of the probe laser is proportional to $\frac{1}{F^2}$ whereas the bandwidth of the Fabry-Pérot interferometer is proportional to $\frac{1}{F}$, the resolution of a perfectly isolated LMRT diagnostic will be limited by the Fabry-Pérot cavity finesse.

[6] Full Width at Half-Maximum, FWHM, in units of length (m)

The bandwidth of the Fabry-Pérot cavity being related to its finesse by:

$$\Delta\lambda_{BW} = \frac{\lambda^2}{2L_{eff}F} \tag{4.16}$$

combining Equations 4.13 and 4.16, the temperature resolution δT of this technique as limited by the Fabry-Pérot cavity finesse is given by:

$$\delta T = \frac{\left[\frac{\lambda}{2F}\right]}{\left[l \cdot \frac{dn}{dT} - \frac{\alpha \cdot c_x'' \cdot n_0^3}{48(1-\upsilon)} + \frac{2(n_0-1)\cdot\alpha\cdot 2s}{l}\right]} \tag{4.17}$$

Making the approximation valid for YAG that the change in refractive index is the dominant thermal term accounting for 75% of the total change in optical pathlength [84], applying Equation 4.15 to the case of a typical probe laser: F = 1000, λ = 1.064μm, $\frac{dn}{dT}$ = $7.3\times10^{-6}K^{-1}$ and sample of length 10mm, a minimum resolution in temperature of <4.5mK is calculated. In all practical interferometric techniques, frequency jitter due to vibrations of the probe laser and Fabry-Pérot resonator components will substantially reduce this sensitivity. It should be noted that if in a given probe resonator there is appreciable mode-hopping, this technique cannot be applied.

Analysis of Cooling Power

If parasitic heating effects outside the pumped region (e.g. surface contamination, fluorescence reabsorption) are greater than the cooling power, the net sample temperature will increase and any cooling effect that is present will not be observed by simple LMRT observation of relative bulk temperature. Application of a steady-state model that compares the temperature in the pumped region of a sample to that at the surface, however, allows the cooling power to be measured. Such a temperature gradient analysis will not be affected by any parasitic heating that may be assumed to be uniform throughout the sample.

At thermal equilibrium, the cooling power is exactly balanced by heat flow into the pumped region and no further change in temperature is observed. The cooling power P_{cool} may therefore be defined for a cylindrically symmetric sample as:

$$P_{cool} = \frac{4\pi K l (T_s - T_p)}{1 + 2ln\left(\frac{r_s}{r_p}\right)} \tag{4.18}$$

where K is the thermal conductivity, l is the length of the sample, T_s & T_p are the temperatures at the surface and in the pumped region respectively and r_s & r_p are the sample and pumped region radii.

Substituting Equation 4.17 into 4.18, the resolution in cooling power δP for a long, centre-pumped sample with co-propagating pump and probe beams is then given by:

$$\delta P = \frac{4\pi K l \lambda}{\left[2 + 4ln\left(\frac{r_s}{r_p}\right)\right] \times \left[l \cdot \frac{dn}{dT} - \frac{\alpha \cdot c_x'' \cdot n_0^3}{48(1-\upsilon)} + \frac{2(n_0-1)\cdot\alpha\cdot 2s}{l}\right]} \tag{4.19}$$

For the typical case of a perfectly isolated system: K = 8.2W m^{-1} K^{-1}, r_s = 3mm and r_p = 0.3mm; this gives a theoretical resolution in cooling power of <1.08mW. Although frequency jitter will substantially reduce this resolution, these calculations prove that the LMRT technique is sufficiently precise to identify any significant cooling effect.

Depending on the pump scheme, practical probe cavity lengths may have mode spacings that are too small compared to the noise (/frequency jitter) to be usefully resolvable. In this work it has been shown, however, that the property of laser resonators that they do not necessarily operate on all the available longitudinal modes can increase the noise-limit to resolution. Section 4.3.2 discusses a preliminary experiment to validate the accuracy of the LMRT technique under conditions of controlled temperature.

4.3.2 Evaluation

Experimental Set-up

To validate the LMRT technique, a 1.064μm Nd:YAG probe laser was built using a plane 2% output coupler at the pumped end and a 300mm ROC high reflector at the other. An AR/AR coated plane-plane 3mm × 10mm Nd:YAG[7] rod was used as the gain medium. This was supported in a water-cooled copper mount held at 17°C. The crystal was pumped at 0.808μm using a *LIMO* 200μm-core, 0.15 NA fibre-coupled laser diode[8] focused into the gain medium using a 30mm focal length spherical lens. Measuring the Nd:YAG 1.064μm laser output power as a function of absorbed 0.808μm pump power (Figure 4.6) the slope efficiency was found to be 55%. The high lasing threshold (P_{th} = 2.5W from Figure 4.6) is ascribed to a poor overlap efficiency for this resonator.

Two intracavity thin film polarizers were used to select π-polarized operation of the Nd:YAG laser. Such polarization selection was included to demonstrate the ability of the probe cavity to be polarization-combined with a pump laser for optical cooling. The probe wavelength of 1.064μm was chosen as the absorption of Yb^{3+}:YAG at this wavelength is – and was measured to be – negligible. Also, given that 1.064μm is longer than the mean fluorescence wavelengths of common Yb-doped samples, for investigations of optical cooling any residual absorption will not heat a pure crystal. An AR/AR coated 5%-doped Yb^{3+}:YAG 3mm × 15mm laser rod from *Scientific Materials Corp.* was mounted in a copper heat sink connected to a Peltier cooler. This was inserted close to the output coupler after a small aperture to minimize the amount of rapidly diverging residual 0.808μm pump light incident on the sample.

[7] manufacturer unknown

[8] model: FP-A0487

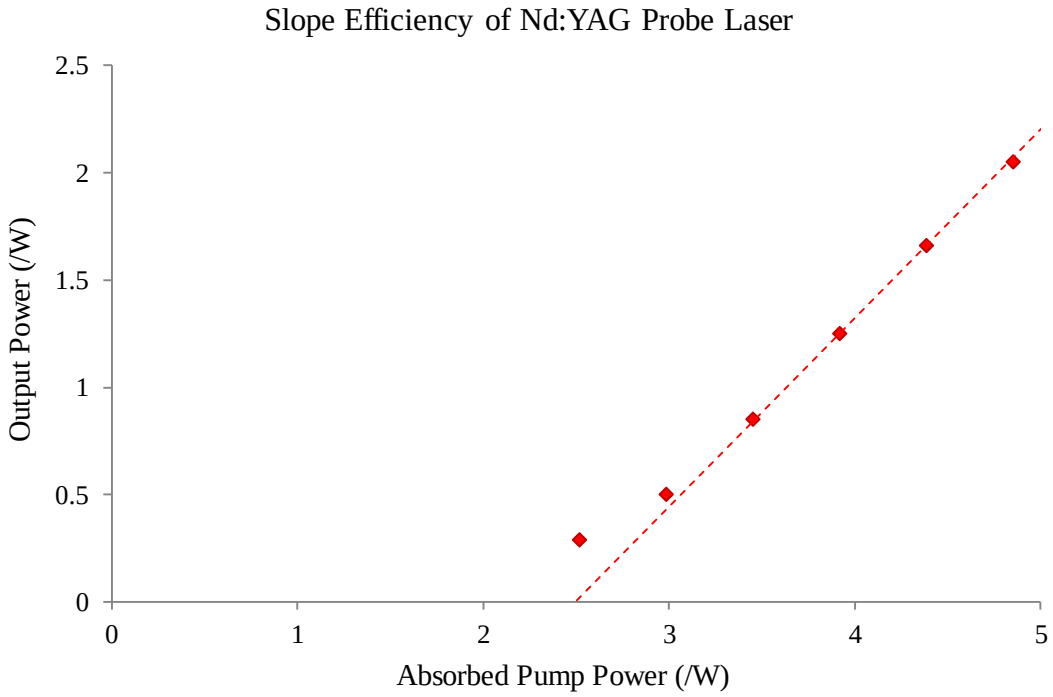

Figure 4.6 – *Plot of output power vs. absorbed pump power for the Nd:YAG probe laser operating at 1.064μm. For a pump wavelength of 0.808μm the slope efficiency is 55%.*

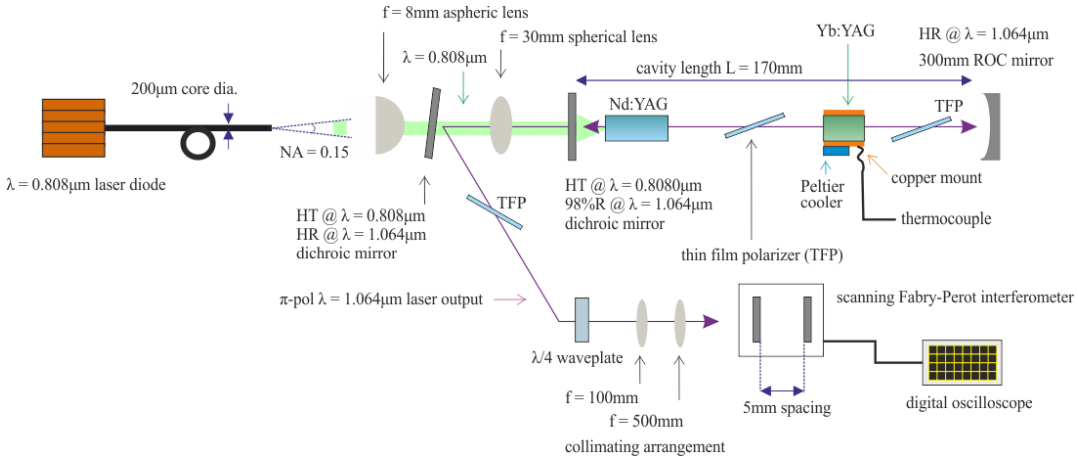

Figure 4.7 – *Schematic of a Nd:YAG laser resonator for evaluating Longitudinal Mode-Shift Relative Thermometry using a Peltier cooled Yb^{3+}:YAG control sample.*

The output from the Nd:YAG laser was separated from the 0.808μm pump using a dichroic mirror having high transmission at 0.808μm and high reflectivity at 1.064μm. The output beam was reasonably collimated by the 30mm spherical lens. It was then passed through an external thin film polarizer and a quarter-waveplate to prevent feedback from the Fabry-Pérot interferometer into the probe cavity. A telescoping arrangement consisting of a 100mm focal length spherical focusing lens and a 500mm focal length spherical re-collimating lens was used to ensure that the beam was well collimated at the Fabry-Pérot interferometer. The collimated 1.064μm beam was then incident on a plane-plane scanning Fabry-Pérot interferometer. This had a mirror spacing L_{FP} of 5mm giving a free spectral range (FSR) of 30 GHz calculated from:

$$FSR = \frac{c}{2mL_{FP}} \tag{4.20}$$

where m = 1 for a plane-plane cavity and m = 2 for a plano-concave cavity. The interferometer was connected to a *Tektronix TDS5053B* digital oscilloscope via a simple, non-commercial[9] amplifier to maximize the signal-to-noise ratio. Setting the timebase of the oscilloscope display such that two Fabry-Pérot resonances (spaced by the FSR) could be observed, the horizontal scale was calibrated from the calculated value for the FSR. Although a commercial *Melles-Griot FPI-25* Fabry-Pérot interferometer[10] was used, information regarding the cavity losses (i.e. mirror reflectivities) was not available. The finesse of the interferometer was therefore calculated experimentally using:

$$F = \frac{FSR}{\Delta\nu_{BW}} \tag{4.21}$$

where $\Delta\nu_{BW}$ is the measured bandwidth of the resonance peaks. For these initial experiments the achieved finesse was only 50. This corresponds to a temperature resolution of ±0.09K calculated from Equation 4.17.

[9] The amplifier was built in-house by an unknown individual prior to the author joining the department.

[10] Model: SW39, compatible controlled with the associated FPZ-3 ramp signal generator.

The length of the Nd:YAG cavity was set at 170mm for which clearly separated modes good be observed on the oscilloscope. The probe beam had a mean radius of 330μm in the sample. As a significant mode-shift occurs during warm-up of the Nd:YAG gain medium, the probe laser was allowed to stabilize for 45 minutes. This initial mode-shift was used to define the directionality of the mode-shift corresponding to heating/cooling. The ability to empirically define the directionality before each experiment without a separate calibration diagnostic is a major advantage to this technique. After stabilization the mode-shift was monitored for a further 15 minutes before any measurements were taken to reference the residual linear drift.

The temperature of the copper mount was controlled using the Peltier cooler and monitored with a thermocouple. The edge-cooled sample was allowed to reach thermal equilibrium with the mount before the mode-shift was measured. As LMRT is a technique for relative temperature measurement, a reference point was taken at 296K (room temperature). Measurements of temperature were then taken down to 292K. For each controlled temperature, 6 measurements of mode-shift were taken over a one minute period to compensate for jitter.

Results and Discussion

Figure 4.5 compares the drift-compensated measurements of temperature relative to a reference of 296K taken using this technique to the thermocouple measured controlled temperature of the mount. The plotted points show the mean of the 6 measured temperature values for each controlled temperature. Considering the experimental uncertainty to be one standard deviation for each of these points at ±0.12K, the uncertainty is ±0.03K above that calculated from Equation 4.17. This demonstrates the noise-limited resolution of such a simple set-up deriving from jitter in the Nd:YAG and Fabry-Pérot cavities. The red line shows the plot for ideal measurements (i.e. gradient = 1), but it must be remembered that due to the resolution of the thermocouple there is an uncertainty of ±0.05K in the values for controlled temperature. There is a 2% difference in gradient between the

least-squares-fit LMRT plot and the real temperature. This is accurate within the limits of experimental uncertainty, validating the LMRT as a technique for relative temperature measurement.

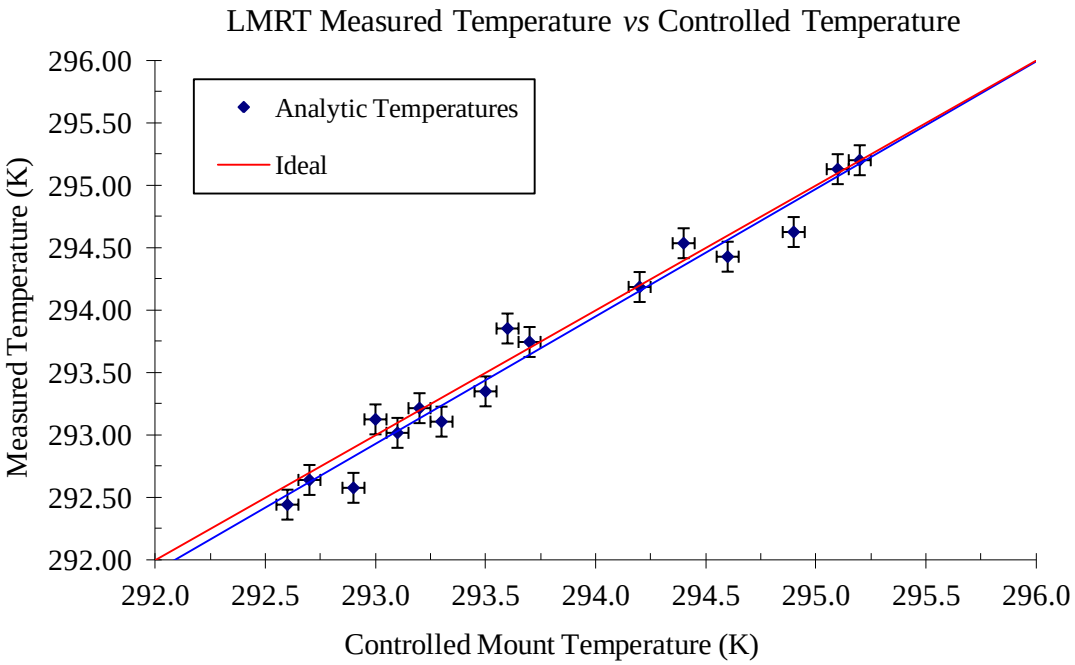

Figure 4.8 – *Plot (blue line) of Yb^{3+}:YAG temperature measured using the LMRT technique at various controlled temperatures between 292K and 296K showing (red line) the expected values for an ideal diagnostic. Errors shown correspond to jitter (vertical ±0.12K) and thermocouple resolution (horizontal ±0.05K).*

The principal error in this set-up resulting from jitter could be reduced by having a rigid set-up and improving the vibrational isolation of the entire system. Shortening the cavity lengths to limit operation to a lesser number of axial modes could contribute to improving the resolution. Reducing the Nd:YAG output coupling and using Brewster-cut samples to reduce cavity losses would increase the cavity finesse and could further improve both the precision and accuracy of this technique. An important point to note is that to operate orthogonally polarized lasers simultaneously

with Brewster-cut sample interfaces (100% σ-polarization loss), a waveplate that leaves the π-polarized beam unchanged (full-waveplate) and rotates the σ-polarized beam by $\frac{\pi}{2}$ (half-waveplate) would be required before the sample. This would reduce the flexibility of the diagnostic as the pump wavelength would have to be determined in advance and could not be tuned. The low measured finesse of the Fabry-Pérot interferometer means that there is clear scope for improving the resolution of the LMRT diagnostic by addressing this.

4.4 Summary

In this chapter two high sensitivity methods of thermometry have been discussed. The PTD technique has been demonstrated for measuring heating in a pumped Yb^{3+}:YAG rod and a novel laser-based diagnostic for monitoring the relative temperature along any path in a transparent sample developed. Although the application of this LMRT technique has been discussed in the context of identifying optical cooling, its potential for use in other work requiring accurate spatial temperature mapping has been demonstrated. Examples of possible uses include detailed studies of thermal lensing in laser crystals and monitoring thermal detuning in VBGs. Without introducing added complexity to the diagnostic set-up, LMRT has given more precise values for relative temperature than those achieved using the simple PTD set-up. Although both techniques have significant scope for optimization, any such improvements would equally benefit both methods and not change their relative performance. Having identified LMRT as the preferred technique for temperature measurement, spatial investigations of optical cooling in Yb^{3+}:YAG and Yb^{3+}:CaF_2 using this diagnostic are discussed in Chapter 5.

Chapter 5

Optical Cooling Experiments

This chapter reports the investigation of optical cooling in Yb^{3+}:YAG and Yb^{3+}:CaF_2 crystals using the pump source and the longitudinal mode-shift relative thermometry technique described in the previous chapters. Local cooling relative to the bulk sample temperature is identified in an Yb^{3+}:CaF_2 crystal pumped at 1.035μm using an Yb-doped fibre laser. The data is analysed exploiting the diagnostic advantages offered by the LMRT technique. Possible parasitic heating effects are explored and discussed.

5.1 Yb^{3+}:YAG Experiments

Experimental Set-up

To investigate optical cooling in Yb^{3+}:YAG using the LMRT technique, the AR/AR coated 3mm × 15mm 5%-doped rod used for the photothermal deflection measurements in Section 4.2.2 was pumped at 1.047μm using a Nd:YLF laser in an intracavity pump scheme (Figure 5.1). An AR/AR coated plane-plane 3mm × 7mm Nd:YLF rod[1] was used as the gain medium. This was supported in a water-cooled copper mount held at 17°C. The Nd:YLF crystal was pumped using an in-house 0.792μm, beam-shaped laser diode stack[2]. The cavity included a thin film polarizer to select σ-polarized operation. The resonator was built using a plane mirror having high reflectivity at 1.047μm at the pumped end and a 300mm ROC mirror having

[1] manufacturer unknown

[2] This stack had been assembled prior to the author joining the department. The laser had no serial number and neither the identity of the originator nor laser parameters were available for reference.

high reflectivity at 1.064μm at the other. The resonator length of 170mm was selected to be equal to that for the Nd:YAG laser resonator (see below). Thus the pump and probe beam sizes would be perfectly overlapped with a mean radius of 330μm through the sample.

The 1.064μm π-polarized Nd:YAG probe laser described in Chapter 4 was overlapped with the pump source at the polarizer. The resonator was built using a plane 2% output coupler at the pumped end and shared the 300mm ROC high reflector with the pump resonator at the other. The shared mirror was selected to have high reflectivity at 1.064μm to give conditions of optimized finesse (i.e. minimized losses) for the probe laser. The 1.064μm output was separated from the 0.808μm pump light using a dichroic at near normal incidence and monitored using the scanning Fabry-Pérot interferometer as described in Chapter 4. The measured double-pass sample absorption was 7.8% at 1.047μm and immeasurable within the limits of experimental uncertainty at 1.064μm.

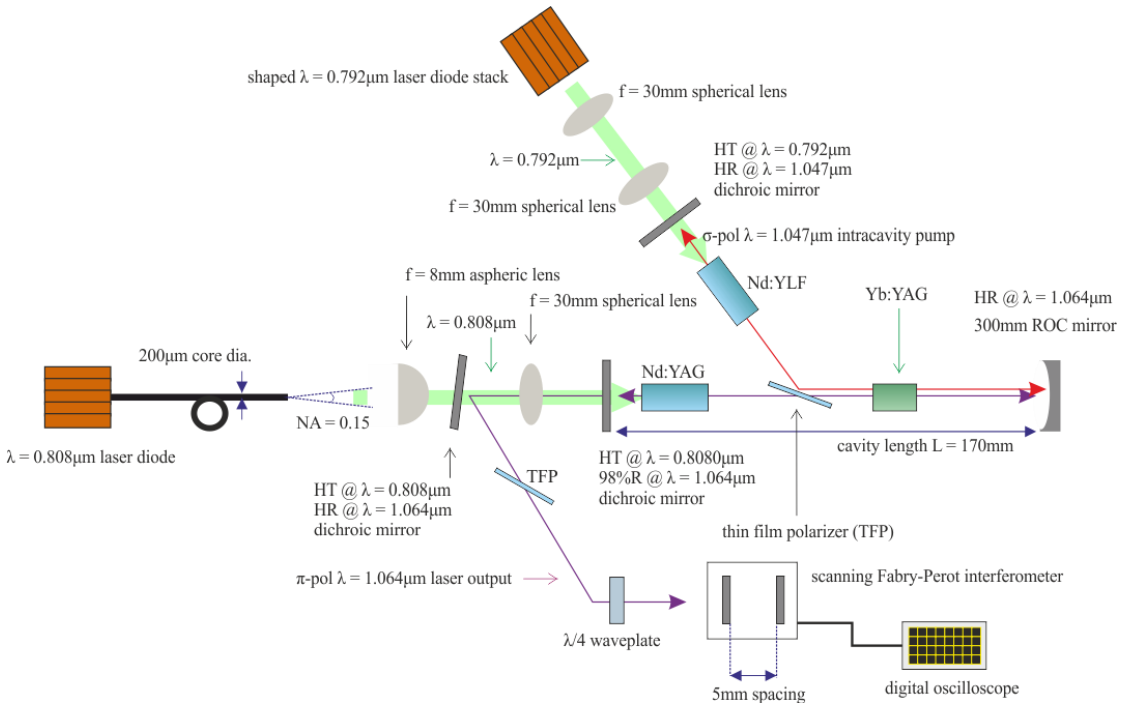

Figure 5.1 – *Schematic for intracavity pumping at 1.047μm using a Nd:YLF laser overlapped with a LMRT Nd:YAG diagnostic laser for optical cooling of* Yb^{3+}*:YAG.*

The Nd:YLF cavity losses L were characterized using a Caird analysis. The standard expression for the Caird formula can be arranged to give:

$$\frac{\lambda_P}{\lambda_L\,\eta_{sl}} - 1 = \frac{L}{T} \tag{5.1}$$

where λ_p is the pump wavelength, λ_L is the lasing wavelength, η_{sl} is the slope efficiency and T is the output coupling. The relationship between slope efficiency and output coupling of the above resonator configuration – including the Yb^{3+}:YAG sample – was investigated by exchanging the back 300mm ROC high reflector for various 300mm ROC output couplers: 2.2%, 5%, 10% and 12.5%. The inverse slope efficiencies were then plotted as a function of inverse output coupling (Figure 5.2). The gradient of the least squares fit line gave a value for the total losses of 9.9%.

Taking the measured Yb^{3+}:YAG double-pass absorption of 7.8%, the cavity losses were thus found to be 2.1%. Such high losses – particularly problematic as the laser was intended for intracavity pumping – were ascribed to the shared Nd:YAG and Nd:YLF components making it difficult to optimally align both cavities. Based on these values for sample absorption and residual loss, the Yb^{3+}:YAG sample was calculated to absorb 85% of the available intracavity power. This corresponded to an absorbed pump power of 3.40W and a predicted cooling power of 73mW calculated using Equation 2.5.

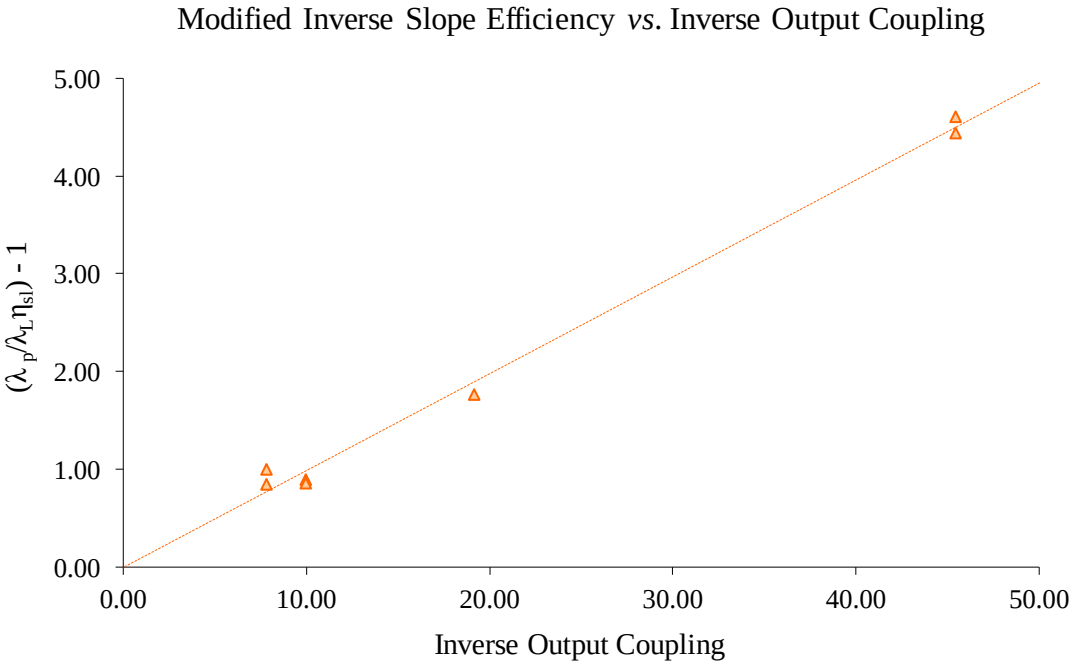

Figure 5.2 – *Plot of modified inverse slope efficiency (see Equation 5.1) vs. inverse output coupling giving measured Nd:YLF cavity losses of 2.1%.*

The sample was pumped for 15 minutes and the longitudinal mode-shift plotted every 20s. The surface temperature of the sample was measured immediately before and after pumping using a thermocouple. During pumping the thermocouple was

removed to avoid fluorescence absorption giving falsely high temperature values and being a source of parasitic heating at the point of contact with the sample.

Results

Figure 5.3 shows fluctuations of ±0.2K in the ambient temperature. These are greater than the ±0.15K jitter-limited experimental uncertainty defined as one standard deviation in the spread of the measured mode positions monitored at a fixed temperature. Averaging out these fluctuations, a temperature rise of 1.6±0.15K is observed within the pumped region. This is greater than the 1.4±0.05 K pre-post surface temperature increase (accounting for ambient temperature fluctuations) measured using a thermocouple at the surface. It is thus observed that there is a heating effect within the pumped region. Applying the steady state analysis described in Equation 4.18 of the previous chapter, a heating power of 90±60mW may be calculated. During the first five minutes of pumping (i.e. before the equilibrium state is reached), the observed temperature rise is linear. This is consistent with that found by photothermal deflection as reported in Section 4.2.2 (Figure 4.4).

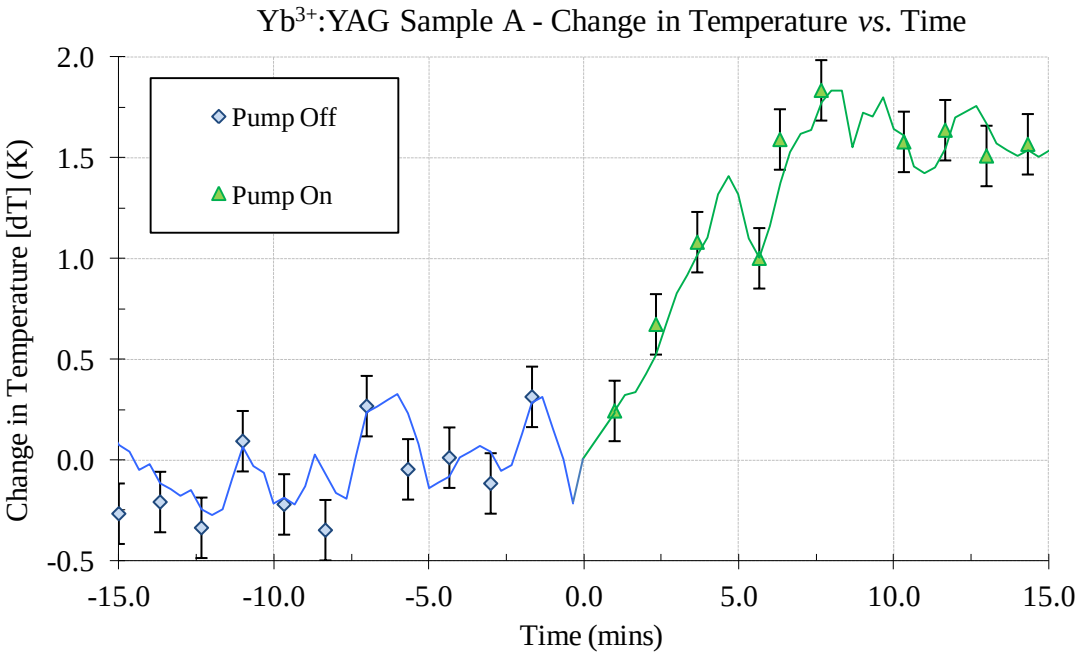

Figure 5.3 – *Plot of temperature vs. time for intracavity-pumped Yb^{3+}:YAG showing a temperature rise of 1.6±0.15K. The solid line connects 3× averaged values with typical data points plotted for clarity. The error bars show the ±0.15K jitter-limited uncertainty in the measurements for temperature.*

Another identical AR/AR coated 3mm × 15mm 5%-doped Yb^{3+}:YAG laser rod supplied by *Scientific Materials Corp.* was then also studied using the same experimental set-up (Figure 5.4).

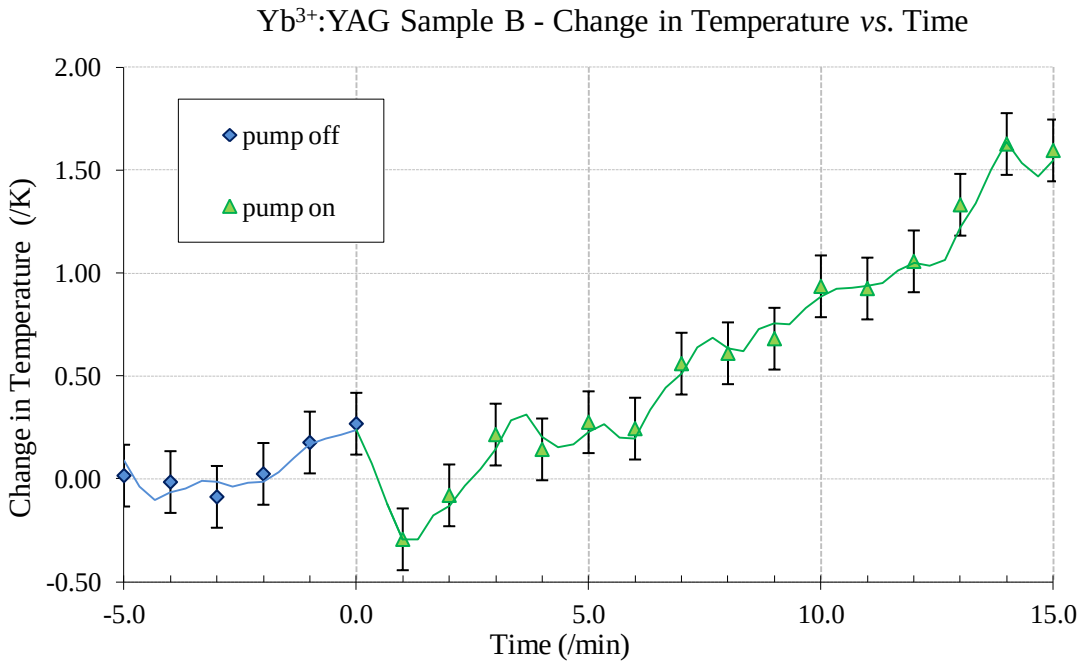

Figure 5.4 – *Plots of temperature vs. time for the second identical intracavity-pumped Yb^{3+}:YAG laser rod showing an initial dip to -0.3±0.15K followed by a temperature rise of 1.6±0.15K. The solid line connects 3× averaged values with typical data points plotted for clarity. Error bars show the ±0.15K jitter-limited uncertainty of the LMRT technique.*

Given the large (~66%) experimental uncertainty in the values for cooling power calculated from Equation 4.18, the observed heating for the two samples is the same. It is interesting to note, however, that the LMRT measurements for sample B show a brief dip in relative temperature to -0.3±0.15K and no roll-off towards the end of the pump period. This is indicative of some cooling within pumped region and a heating effect predominantly outside this area. A temperature gradient is still observed from a comparison of the LMRT values and the 1.3±0.05K pre-post thermocouple measurement. Considering the substantial experimental uncertainty in the LMRT value, however, this may be a lesser effect than the raw figures initially suggest. Reconciling the observations of a temperature gradient and initial cooling, it may be

reasoned that there is non-uniform heat removal/deposition along the path of the pump beam. It is important to note that this observation of possible cooling in Yb^{3+}:YAG could not be reliably achieved after exchanging the sample.

The ultimate goal of this work was to identify samples for use in future optical cooling research. As each of the commercially obtained Yb^{3+}:YAG samples demonstrated bulk heating, no more detailed studies were performed with these crystals. Although temperature gradients could be resolved, these results show that for accurate investigations of cooling power additional measures must be taken to reduce jitter in the probe and Fabry-Pérot resonators.

5.2 Yb^{3+}:CaF_2 Experiments

Although recognized as a good candidate crystal due to its low phonon energies (i.e. reduced multiphonon nonradiative decay), cooling in Yb^{3+}:CaF_2 has not previously been reported. As discussed in Section 2.2, it offers both a higher theoretical cooling efficiency and pump absorption than Yb^{3+}:YAG when pumped at 1.047μm. A high-purity 3%-doped Yb^{3+}:CaF_2 crystal of dimensions[3] 8×5×10.7mm^3 was grown at the University of Caen[4] by the Bridgman process. The crystal was left uncoated to eliminate any possible end-face heating related to the coating compounds.

5.2.1 Intracavity Pumping

Experimental Set-up

The experimental set-up described in Section 5.1 was modified by the inclusion of a second intracavity thin film polarizer (Figure 5.5). This allowed the probe and pump resonators to be fully independent and easily adjusted for temperature measurement along an arbitrary path relative to the pump beam. The Nd:YLF resonator was now completed using a 300mm ROC mirror with high reflectivity at 1.047μm. The Nd:YLF resonator length was kept matched to that of the Nd:YAG laser at 170mm in order to maintain good overlap with the probe beam. The low thermal contact mount (Figure 4.3) was fixed to a 3D translation stage allowing the path of the pump beam through the crystal to be readily shifted without requiring realignment of the cavity. The entire Nd:YAG resonator was built on a single baseplate and special attention paid to tightening all securing screws. Implementing these measures a jitter limited resolution of ±0.05K was achieved corresponding to one standard deviation in the

[3] These dimensions were selected to allow for the possibility of Brewster angled pumping in a future set-up.

[4] The author gratefully acknowledges the support of Richard Moncorgé, University of Caen for providing the Yb^{3+}:CaF_2 crystal.

spread of measured mode positions at a fixed temperature. This precision is equal to that for the thermocouples used in the cooling experiments.

The 500mm focal length collimating lens before the Fabry-Pérot interferometer was replaced with a 1m focal length spherical lens to further improve the collimation of the probe output beam. The finesse of the Fabry-Pérot interferometer calculated from the free spectral range and resonance bandwidth using Equation 4.21 was now 135. This corresponds to a decrease in the resonator losses of 7.9% found using the approximation:

$$F \approx \frac{2\pi}{1-\rho} \equiv \frac{2\pi}{L} \tag{5.2}$$

where ρ is the fractional power remaining after one round-trip and L defines the resonator losses. The most probable explanation for such a substantial improvement is that the reduced jitter in the probe resonator has allowed the resonance bandwidth to be more accurately measured than for the previous experiments. Applying Equation 4.17 the theoretical temperature resolution of the LMRT probe is found to be ±0.044K. Thus the achieved jitter-limited resolution is within 6mK of the theoretical value.

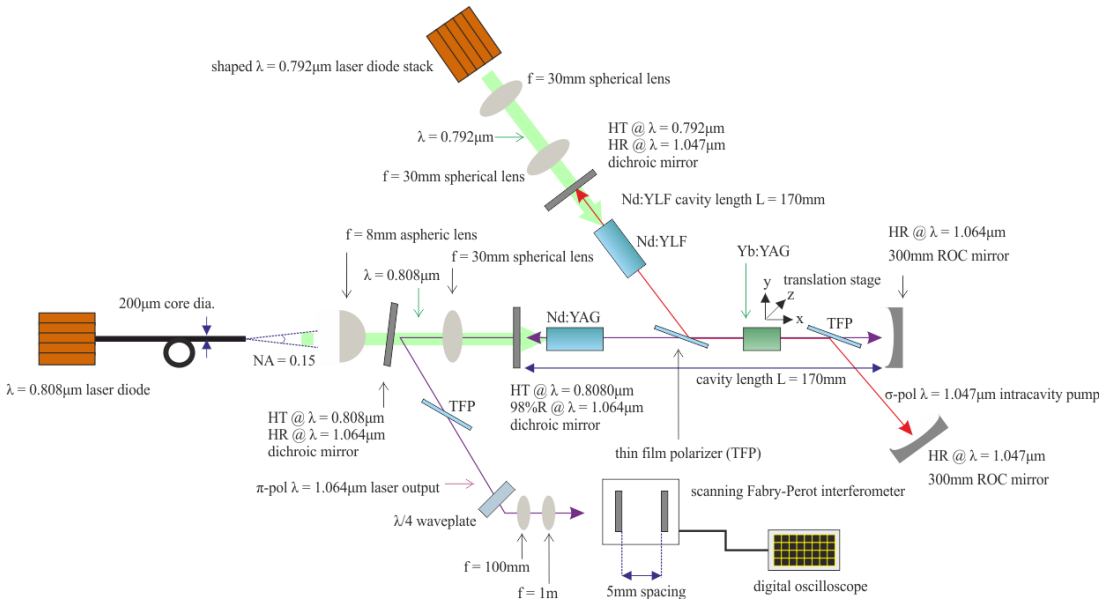

Figure 5.5 – *Schematic for intracavity pumping at 1.047μm with a Nd:YLF bulk laser overlapped with a Nd:YAG LMRT diagnostic laser for optical cooling of* Yb^{3+}*:*CaF_2.

The double-pass absorption of the Yb^{3+}:CaF_2 sample at 1.047μm was measured to be 8.1%, in close agreement with the predicted value of 8.2% (see Figure 2.6). Performing a Caird analysis using the same methodology as described in Section 5.1 (Figure 5.6), the Nd:YLF cavity losses were found to be 0.9%. Comparing this value to the 2.1% losses for the intracavity pump laser in Section 5.1, separating the Nd:YAG and Nd:YLF cavities significantly improved the pump laser performance. Taking the measured values for sample absorption and resonator losses, the Yb^{3+}:CaF_2 crystal was calculated to absorb 90% of the available pump power. This corresponds to 3.6W of absorbed power and a predicted cooling power of 130mW. Although Yb^{3+}:CaF_2 does not offer a significant improvement in absorption compared to Yb^{3+}:YAG at 1.047μm, the improved resonator alignment for this experimental configuration has allowed an additional 5% of the available power to be usefully absorbed for cooling. The doubling of the predicted cooling power is due to the greater cooling efficiency of Yb^{3+}:CaF_2 (3.6% c.f. 2.1%). The sample was

centre-pumped on its long axis for 15 minutes and the longitudinal mode-shift plotted every 20s. The initial and final sample temperatures were measured using a thermocouple. This was removed during pumping to prevent fluorescence reabsorption giving falsely high results. The ambient temperature was measured every minute within 20mm of the sample using a thermocouple that was shielded from Yb^{3+}:CaF_2 fluorescence by gold foil.

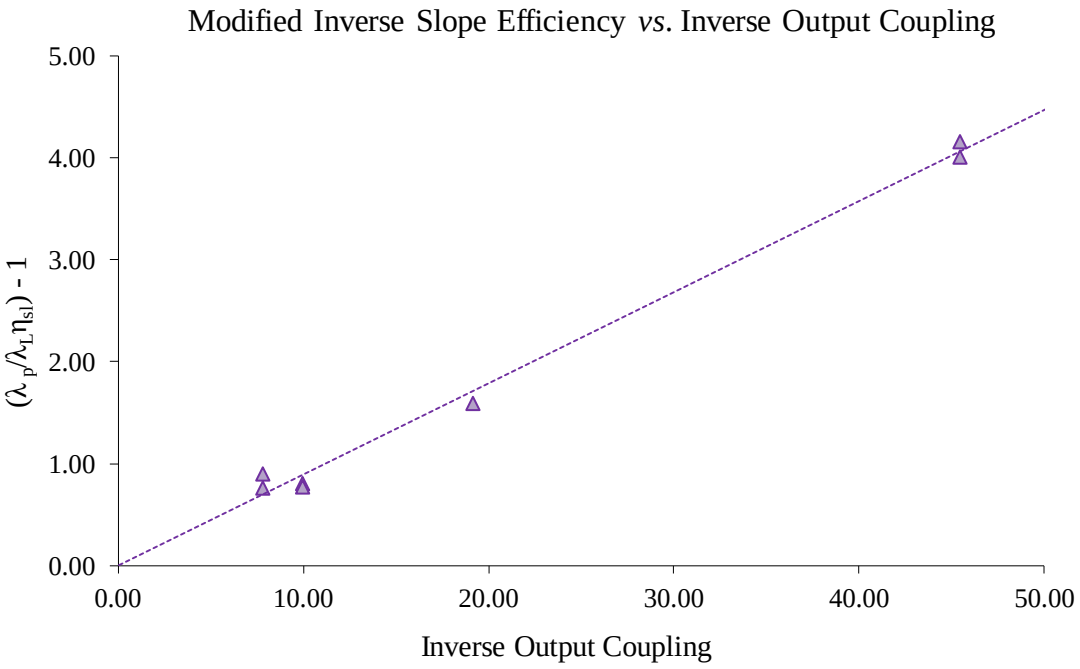

Figure 5.6 – *Plot of modified inverse slope efficiency (see Equation 5.1) vs. inverse output coupling giving measured Nd:YLF cavity losses of 0.95%.*

Results

The plot for the Yb^{3+}:CaF_2 crystal centre-pumped on its long axis (Figure 5.7) shows a temperature increase of 0.5±0.05K. This temperature rise is the same as the pre-post temperature change at the surface measured using a thermocouple. It may thus be concluded that any cooling effect is offset by parasitic heating within the limits of experimental uncertainty. There is insufficient evidence to conclude from

this data whether uniform fluorescence reabsorption is the cause of the increase in bulk sample temperature.

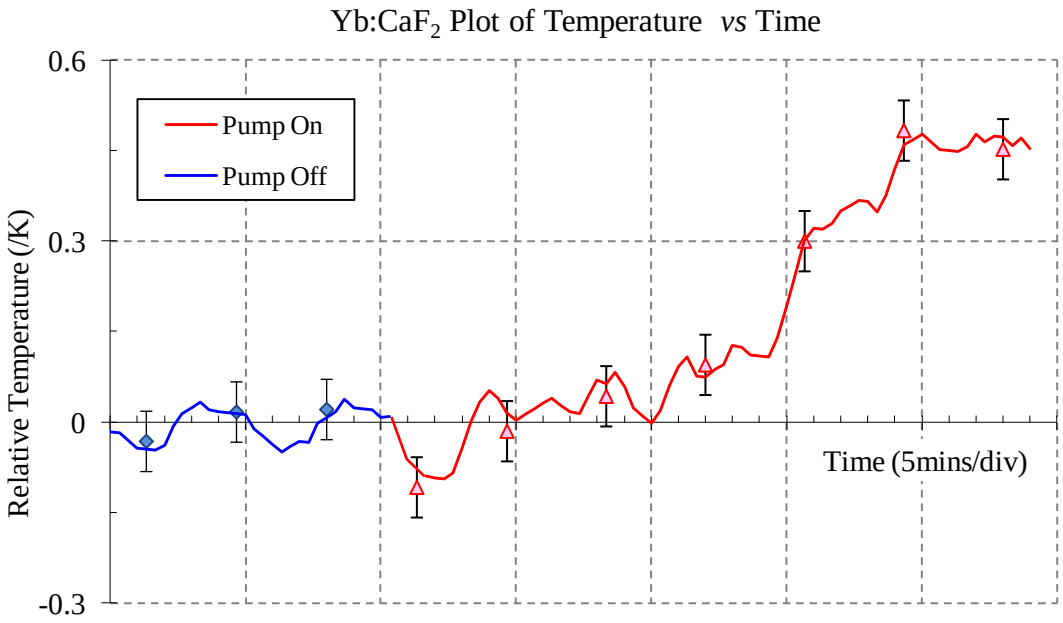

Figure 5.7 – *Plot of temperature monitored using LMRT vs. time for Yb^{3+}:CaF_2 intracavity pumped at 1.047μm using a Nd:YLF bulk laser.*

Immediately after the pump is turned on there is a consistently observed brief dip in the measured temperature. This indicates that the component of heating along the path of the pump beam may not quite offset the cooling and that the heating effect is probably due to fluorescence reabsorption[5]. To establish whether fluorescence reabsorption was the dominant parasitic heating mechanism, this experiment was repeated with the sample pumped close to each of the four corners (Figure 5.8) where ~69% of the fluorescence 'immediately' escapes [54]. Figure 5.9 shows the measured temperature changes.

[5] either by dopants or impurities

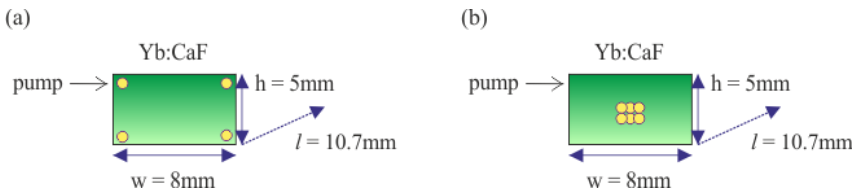

Figure 5.8 – *End-face of a 8×5×10.7mm^3 Yb:CaF$_2$ crystal pumped along its long axis showing (a) approximate positions of the pump paths for the four cases of corner pumping and (b) approximate range of pump paths used for pumping within the approximation of cylindrical symmetry.*

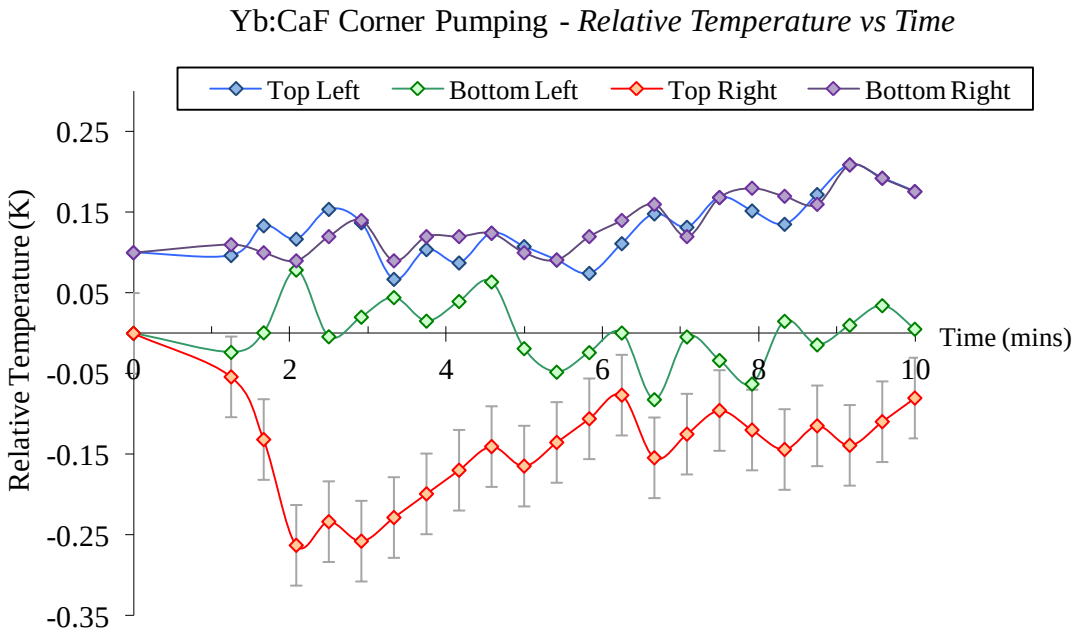

Figures 5.9 – *Solid lines show the 3× averaged relative temperature for Yb^{3+}:CaF$_2$ intracavity-pumped along each of the four corners. Typical points are plotted for clarity with error bars showing ±0.05K jitter-limited resolution of the LMRT technique. The top left and bottom right data (blue & purple lines) is offset by +0.1K for clarity.*

Accounting for the ±0.1K fluctuations in ambient temperature, three of the pump paths resulted in the net sample temperature increasing by between 0.1→0.2±0.05K when measured before and after using a thermocouple. When pumping along the 'top right' corner, no temperature change was measured within the limits of experimental uncertainty. From these results there is clearly still a heating effect offsetting the predicted cooling, however corner pumping has substantially reduced this when compared to the center pumped data in Figure 5.7. Due to the asymmetric pump arrangement, a simple temperature gradient analysis for evaluating the cooling power cannot reasonably be applied. However, as corner pumping has substantially reduced the net heating of the sample, it may be concluded that fluorescence reabsorption is the dominant heating mechanism in the sample.

The absence of any initial temperature decrease in the LMRT data for three of the corners indicates that there is parasitic heating along the path of the pump beam in addition to the identified fluorescence reabsorption effect. Considering the difference in performance between the corners, it is concluded that this parasitic heating in the pumped region is not spatially uniform throughout the sample.

For each of the four cases the final temperature measured within the pumped region was slightly less than that found using a thermocouple. This provides evidence that there is a limited, local cooling effect within the pumped region of the sample. When pumping along the 'top right' corner, a pronounced temperature decrease of 0.3±0.05K was seen before a slow temperature rise to an equilibrium value of -0.15±0.05K. It is thus proven that by taking steps to minimize fluorescence reabsorption an optically pumped region of an Yb^{3+}:CaF_2 sample can be cooled from its initial temperature.

5.2.2 *In Vacuo* Pumping

Experimental Set-up

To ensure that variations in the ambient temperature could be excluded as causing the observed temperature changes, the Yb^{3+}:CaF_2 sample was placed in a vacuum chamber[6] held at 3.6×10^{-3}mbar. For achieving significant cooling, it is important to use low emissivity coatings in the chamber to minimize blackbody heating of the sample. For the small temperature changes considered in these experiments, blackbody radiation does not contribute significantly to the heating. Thus black anodizing was used to absorb the fluorescence in the water-cooled vacuum chamber.

A 300mm ROC mirror having high reflectivity at 1.064μm was inserted into the vacuum chamber. A window with anti-reflection coatings at 1.064μm allowed the Nd:YAG probe laser discussed in previous sections to be built with the 0.808μm pump source, the gain medium and 2% output coupler situated outside the vacuum chamber. The resonator length was increased to 230mm to accommodate the spatial constraints placed by the dimensions of the vacuum chamber. A single thin film polarizer was included between the gain medium and the vacuum chamber window to select π-polarized operation. The 1.064μm output was monitored using a scanning Fabry-Pérot interferometer as described in Section 5.2.1. Although the 300mm ROC high reflector was no longer mounted on the same baseplate as the other resonator components, the same temperature resolution of ±0.05K could be achieved.

For these experiments a variation of the seed-amplifier fibre pump source described in Section 3.2.2 was used. The VBG was replaced with a diffraction grating for wavelength selection and the unpolarized seed-amplifier operated at 1.035μm, the optimum pump wavelength for Yb^{3+}:CaF_2. Despite modifying the seed source, there was no significant change in the amplifier slope-efficiency (see Figure 3.13). The 1.035μm pump beam collimated using an 8mm focal length aspheric lens was overlapped with the Nd:YAG laser at the thin film polarizer. As the fibre based pump

[6] The author gratefully acknowledges Lee Pearson for designing and arranging the manufacture of the chamber prior to the author joining the department.

system was unpolarized, this incurred a 50% loss due to π-polarized transmission at the polarizer. The 300mm ROC mirror inside the vacuum chamber retro-reflected the pump beam through the sample thereby doubling the absorption pathlength. The double-pass absorption of Yb^{3+}:CaF_2 at 1.035μm was measured to be 15.1%. This is in reasonable agreement with the predicted value of 15.7% (see Figure 2.6). The sample was calculated to absorb 314mW of 1.035μm pump light. Applying Equation 2.5 this gives a predicted cooling power of 8mW.

The vacuum chamber had inputs for two thermocouples. Both thermocouples were connected to gold strips of equal area. One was placed in contact with the sample and the other slightly separated from it to reference the effect of heating on the thermocouple. A continuous, accurate thermocouple measurement of the sample surface temperature could then be monitored. Having identified spatial variations in the parasitic heating from the analysis presented in Section 5.2.1, the sample was pumped along various central paths (Figure 5.8b) in an attempt to locate a pump path for which significant local cooling could be observed. Only central paths were investigated in order to approximate cylindrical symmetry allowing the steady-state analysis in Equation 4.18 to be applied for evaluation of the cooling power. For each experiment (/path) the sample was pumped for 20 minutes and both the mode-shift and thermocouple values plotted every 20s.

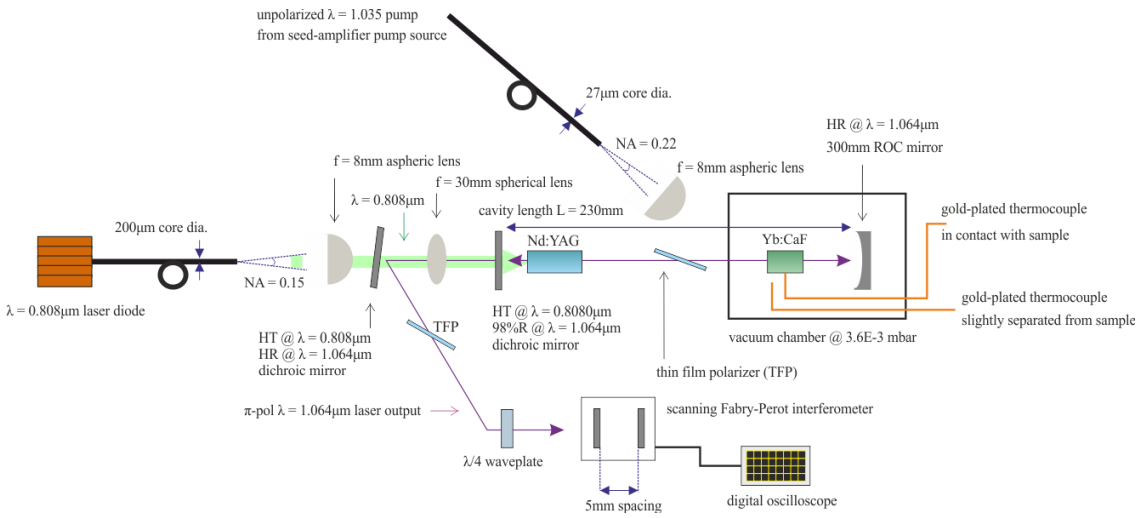

Figure 5.10 – *Schematic for in vacuo pumping of an Yb^{3+}:CaF_2 sample pumped using a 1.035μm seed-amplifier source and overlapped with a Nd:YAG laser for LMRT measurement.*

Results

Centre-pumping the sample (i.e. repeating the measurements presented in Figure 5.7), a temperature increase was again observed in the pumped region. As this was in agreement with the experiments performed in the previous section at atmospheric pressure, it may be concluded that convective heating due to ambient effects is not a significant contributing factor to the parasitic heating. Adjusting the position of the pump beam, it was possible to find a path along which the temperature *T(p)* in the pumped region of the Yb^{3+}:CaF_2 crystal was 1.4±0.1K lower than the surface temperature *T(su)* (Figure 5.11). The temperature in the pumped region returned to thermal equilibrium with the rest of the sample over 10 minutes. Making the assumption that there is minimal heat loss from a sample held *in vacuo*, the net (/equilibrium) temperature of the sample is observed to increase by 0.3±0.05K when pumped in this configuration.

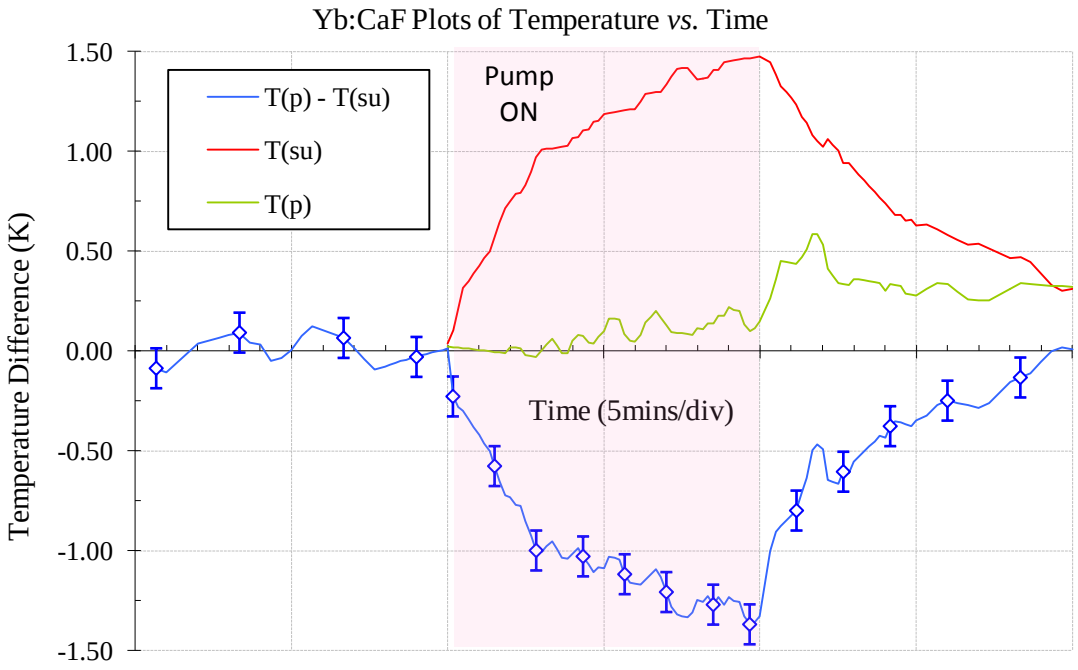

Figure 5.11 – *Local relative cooling (blue line) measured using a steady-state comparison of the thermocouple measured surface T(su) and LMRT measured pumped region T(p) temperatures for* Yb^{3+}*:*CaF_2 *pumped in vacuo at 1.035μm. Lines are plotted to a 3× moving average with typical data points for clarity. Error bars correspond to the ±0.1K combined uncertainty from the thermocouple and LMRT measurements.*

As discussed in Chapter 4, a sample experiencing heat deposition/removal uniformly around its surface (e.g. due to surface contamination) will have a uniform steady-state temperature profile (top hat). A sample experiencing heat deposition/removal uniformly through its bulk (e.g. due to fluorescence reabsorption) will also have a uniform steady-state temperature profile. The only steady-state condition under which there will be a temperature gradient in a sample is the case that there is non-uniform heat deposition/removal within the bulk of the sample. It may thus be concluded from the results presented in Figure 5.11 that there is heat being removed along the path of the pump beam. Taking the approximation of cylindrical symmetry and applying Equation 4.18, this cooling effect is evaluated to

be 5mW. This compares to the theoretical value of 8mW that is based on the assumption of pure radiative decay.

As the net sample temperature increased, there must be heat deposition outside of the pumped region offsetting this cooling effect. These results support the initial findings drawn in Section 5.2.1 that there are at least two parasitic heating effects in pumped Yb^{3+}:CaF_2: a spatially variant component along the path of the pump beam and a component that is approximately spatially uniform throughout the sample, the most likely cause of which is fluorescence reabsorption. The results presented in this section improve upon those in Section 5.2.1 in demonstrating the ability to achieve local optical cooling in Yb^{3+}:CaF_2. The potential of this material for further investigation is shown. The presence of the parasitic heating effects mentioned above means, however, that this particular crystal in its current geometry is not suitable for use in future optical cooling research.

5.3 Discussion

There may be two parasitic heating effects in an optically cooled solid: decay (radiative and nonradiative) of ions distributed uniformly throughout the sample due to excitation by fluorescence reabsorption and nonradiative decay of ions (dopants and/or impurities) in the pumped region. The distribution of dopants and impurities in a sample grown to high purity may reasonably be assumed to uniform. In a 'pure' crystal isotropic, low intensity fluorescence means that reabsorption due to impurity ions will be negligible and not contribute significantly to the heating. As discussed in Section 2.3.1, however, fluorescence reabsorption by rare-earth-dopants has the potential to completely offset the cooling power. The spatial studies of optical cooling using the LMRT technique have allowed fluorescence reabsorption outside the pumped region to be directly identified as a contributing factor to the parasitic heating effect in an optically pumped sample. By reducing the mean pathlength for fluorescent photons in the sample, the parasitic heating effect was observed to be reduced. The LMRT technique has also enabled a heating effect in the pumped region that is not spatially uniform throughout the sample to be distinguished from the contribution due to fluorescence reabsorption. This effect, attributed to nonradiative decay of ions in the pumped region, is demonstrated to be the critical factor in observing cooling.

The initial investigation into Yb^{3+}:YAG gave the first direct evidence for the conclusion that parasitic heating in standard commercial crystals occurs predominantly in the pumped region. The core temperature of a centre-pumped crystal was found to be greater than that at the surface, a steady-state temperature profile requiring heat deposition of 90mW in the pumped region. This suggests that optical cooling requires samples that are grown to higher purity than commercially available laser crystals; a critical point to consider when planning any future research.

The more detailed spatial investigation of the Yb^{3+}:CaF_2 crystal by means of the newly developed LMRT technique demonstrated conclusively that the heating effect in the pumped region is not necessarily uniform throughout the sample. A single

crystal was observed to exhibit regions of local heating and cooling. Although for the purposes of considering fluorescence reabsorption throughout the sample the distribution of dopants and impurities was reasonably assumed to be uniform, slight variations may arise during the crystal growth process. As pure nonradiative decay of an ion contributes approximately -20× the cooling effect for purely radiative transition, slight variations in the concentration of impurities will have much more significant impact on the parasitic heating effect. This work provides a more rigorous confirmation of published research identifying localized cooling in samples by means of the photothermal deflection technique [29, 47, 50]. The investigation of Yb^{3+}:CaF_2 reported in this thesis also demonstrated that even when pumped along such a 'cooling path' fluorescence reabsorption throughout the crystal may still result in net heating of the sample. The spatially-selective LMRT technique has allowed local cooling in Yb^{3+}:CaF_2 to be identified despite net fluorescence reabsorption heating. A cooling power of 5mW has been quantified using the steady-state analysis described in Chapter 4.

This work did not have the scope to conduct independent detailed spectroscopic evaluations of the samples used, but the concentration of impurities can reasonably be assumed to be very low so as not to have been observed by the crystal growers (Yb^{3+}:CaF_2 [117]). Assuming that impurity absorption of the pump light results in purely nonradiative decay (i.e. worst case scenario) and that dopant absorption leads to purely radiative decay (i.e. best case scenario, no multiphonon decay), Yb^{3+}:YAG pumped at 1.032μm would require a relative impurity concentration[7] of 0.70% and Yb^{3+}:CaF_2 pumped at 1.035μm a relative impurity concentration of 2.33% to exactly balance the cooling. In practice the dopants may undergo multiphonon decay thus reducing the effective cooling efficiency. This would further decrease the impurity concentrations required to offset cooling. Other than multiphonon decay, there are three other possible contributions to parasitic heating: dopant-impurity interaction, dopant-dopant interaction (clustering) and structural defects in the crystal.

As the Yb^{3+}:CaF_2 crystal was grown to high purity in an academic environment [72], it may reasonably be assumed that undetected structural defects are not the

[7] Percentage of impurities as a fraction of the dopant concentration.

cause of these transitions. Section 2.3.2 of this thesis discusses the probability of dopant-dopant and dopant-impurity interactions. In this discussion it is shown that for the rare-earth-doping concentrations used, unless significant clustering of ions occurs, dopant-dopant interaction is a negligible effect. The contribution of ion-ion interactions due to impurities will be even smaller. Therefore the experiments reported in this chapter, when compared with a theoretical analysis of the parasitic heating processes in rare-earth-doped crystals, show that nonradiative decay of impurity ions excited by absorption of pump photons critically limit the ability to achieve optical cooling in solids. Thus it is essential that research in this field includes involvement in the sample growth. It is also demonstrated that if net cooling is to be achieved, a sample geometry that minimizes fluorescence reabsorption is required. Suitable samples would either be closely matched to the dimensions of the pump beam (pumping along a single path) or thin (for complex pump geometries). A rectangular geometry should be selected to reduce fluorescence trapping.

5.4 Summary

This chapter discussed in detail experiments for the identification of optical cooling in Yb^{3+}:YAG and Yb^{3+}:CaF_2 crystals. Conclusions are drawn from these results about the parasitic heating effects in cooling samples. It is shown in this work that ultra-pure samples are a critical requirement if optical cooling is to be observed. The role of sample geometry is also shown to be a factor in achieving net cooling.

Although in the course of these studies no suitable samples were identified for further cooling research, the capabilities of the novel LMRT technique have been proven in making the first reported observations of local optical cooling by anti-Stokes fluorescence in Yb^{3+}:CaF_2. Relative cooling by 1.4±0.1K is reported for a local temperature rise of 0.1±0.05K. Minimizing fluorescence reabsorption the pumped region of the sample has also been demonstrated to cool by 0.15±0.05K from its initial temperature. LMRT has been demonstrated as a diagnostic that can usefully discriminate thermal effects within the pumped region of a sample from ambient temperature fluctuations and heating due to fluorescence reabsorption.

Chapter 6

Conclusion and Future Work

6.1 Summary and Conclusions

The principal aim of the work covered in Part 1 of this thesis was to develop a novel diagnostic for the measurement of temperature along any path within a transparent sample in order to open new avenues of research in optical cooling. The requirement for a simple and robust method for temperature measurement has been realized in the novel laser-based technique of longitudinal mode-shift relative thermometry (LMRT). The theory underlying this technique has been discussed and validated empirically. The application of the diagnostic in its intended role for identifying optical cooling by anti-Stokes fluorescence has been proven in a series of experiments with Yb^{3+}:YAG and Yb^{3+}:CaF_2 samples. The demonstrated ability of the LMRT technique to measure local temperature changes within transparent media to interferometric precision while retaining a relatively simple set-up is a significant step forward in the field of thermometry. The usefulness of LMRT as a diagnostic extends well beyond the field of optical cooling, the observation of thermal effects in laser crystals (e.g. thermal lensing) and detuning in volume Bragg gratings (VBGs) being just two alternative applications.

The LMRT technique developed in this work offers the first reported approach for measuring cooling within the pumped region of a sample independently of external heating effects[1]. Localized cooling has been successfully discriminated from fluorescence reabsorption and fluctuations in the ambient temperature. Thus LMRT could be readily employed to identify the regions of a crystal that exhibit cooling,

[1] This is achieved by performing a steady-state analysis from the LMRT measured temperature.

avoiding commercially critical time and money being lost in the preparation of crystals unsuitable for use in optical refrigerators.

The cooling experiments performed to test the LMRT technique agree with published research in that the optical cooling effect in solids is extremely sensitive to crystal purity. The difficulty in finding crystals of the required purity has greatly hindered further research in the field. The most important conclusion to be drawn from the reported investigations into optical cooling is that the growth of ultra-pure samples is a key area of research to pursue. If reliable sourcing of sufficiently pure crystals is found, any future research would greatly benefit from the temperature measurement capabilities developed in this work.

The other contribution that this work has made to the specific field of optical cooling has been the first reported identification of local cooling in an Yb^{3+}:CaF_2 crystal. A temperature difference of -1.4±0.1K relative to the bulk sample temperature has been achieved corresponding to a measured cooling power of 5.1mW. In this experiment, however, the bulk sample temperature increased by 1.5K. Separately cooling to an equilibrium value of -0.15±0.05K from the initial sample temperature has been achieved. The potential of pure Yb^{3+}:CaF_2 for use in future optical cooling experiments has thus been demonstrated.

In the course of the development and study of LMRT for optical cooling applications, a contribution has been made to the characterization of self-pulsing in fibre lasers. The frequent catastrophic failure of the designed fibre lasers due to self-pulsing presented a major challenge to the building of a reliable pump source. The subsequent investigation into self-pulsing led to the observation of ‘pulse packets’ consisting of four small pulses followed by one large (~×2 amplitude) pulse as a feature of sustained self-pulsing (SSP) in a fibre laser. The technique recently published by Guan & Marciante [98] for the suppression of self-pulsing by extending the cavity round-trip time using a long length of passive fibre was adapted for use with the proposed pump source. It was integrated in such a way as to also achieve fundamental mode operation with the multi-mode active fibre. Self-pulsing can greatly impede progress in all areas of fibre laser research. Verifying this approach

for the suppression of self-pulsing with the added feature of mode selection therefore makes a useful contribution to the broader field of fibre lasers.

6.2 Future Work

Part 1 of this thesis covers a comprehensive evaluation of LMRT as a diagnostic for observing thermal effects in transparent samples, particularly in the context of optical cooling. Future application of this measurement technique in the field of optical cooling would primarily involve the initial identification of suitably pure crystals at the point of growth. There is also the possibility to employ LMRT as the diagnostic in low temperature cooling experiments as a simpler non-contact diagnostic than current spectroscopic and photothermal deflection methods. To be viable any such cooling research should have access to ultra-pure crystals that are preferably grown within the framework of the research establishment conducting the experiments. As higher power bulk lasers are developed and VBGs increasingly used for narrow linewidth wavelength selection, LMRT could also prove its value as a diagnostic in more fundamental laser research.

LMRT would be of greatest value in studies to expand the range of candidate samples, but future research into optical cooling should focus on maximizing the available and absorbed pump. This could be most readily be achieved by increasing the available pump power with higher amplification in the seed-amplifier source developed in this work. Another approach that builds on this fibre pump source is to maintain the cooling efficiency by active feedback wavelength tuning of the pump source. Real-time digitally processed LMRT monitoring could be used as a controller in such a set-up. A more radical solution is to use a resonance-enhanced fibre laser [118] for intracavity pumping. This could combine the advantages of the fibre lasers developed in this work with the high pump absorption offered by conventional intracavity pump schemes. This latter approach could be combined with active feedback tuning to maintain cooling powers that are an order of magnitude greater than any that have been reported to date.

6.3 Concluding Remarks

The work covered in Part 1 of this thesis began with the objective of identifying rare-earth-doped crystals for use in optical cooling experiments. A novel, flexible technique for the measurement of local thermal effects in transparent samples has been developed for this purpose. This diagnostic has been demonstrated in the context of optical cooling research with investigations of Yb^{3+}:YAG and Yb^{3+}:CaF_2 crystals. Despite achieving relative local cooling to -1.4±0.1K and absolute local cooling of -0.15±0.05K, no suitable samples were identified for further optical cooling experiments. The diagnostic technique and pump sources developed in this project have, however, established the foundations for continued research in this field.

Part 2

Laguerre-Gaussian Mode Generation

Chapter 7

Introduction to Laguerre-Gaussian Modes

Section 7.1 begins this chapter with a discussion of the motivation for studying Laguerre-Gaussian mode generation. Section 7.2 summarizes the aims of Part 2 of this thesis and Section 7.3 outlines its structure. Sections 7.4 and 7.5 respectively cover the historical and theoretical background to LG modes.

7.1 Motivation

Silicon chips and novel computing devices require machining to nanoscale precision. No longer are the frontiers of medicine at the cellular level, but involve the study of individual biological molecules. Conventional mechanical apparatus is rapidly becoming too cumbersome to satisfy the needs of both researchers and industry, a clear solution to which is the use of coherent light sources for momentum transfer at the atomic scale.

Laguerre-Gaussian (LG) modes, also commonly referred to as 'ring' or 'doughnut' modes, are the cylindrically symmetric set of resonator eigenmodes. In contrast to Hermitian-Gaussian (HG) modes which can have an arbitrary number of tranverse nodes depending on the mode indices *n,m*, all LG modes other than the fundamental are ring shaped with an arbitrary number of radial nodes depending on the mode indices *p,l*. In this work only the $p = 0$ modes having a single central node are considered. This central node originates from a $2\pi l$ azimuthal phase-shift around a LG mode creating a phase singularity at the centre. This azimuthal phase-shift, resulting in a Poynting vector that traces a helical path, gives LG modes the unique property of an angular momentum component that is independent of polarization.

Although the transfer of photon momentum is an established technique for the manipulation of particles, most lasers carry only linear momentum in their direction of propagation thereby limiting their usefulness. The angular momentum carried by LG modes can, however, also be imparted to particles upon interaction with matter making LG beams of interest in a wide variety of applications such as: 'optical bottles' [119], 'optical spanners' [120], 'optical tweezers' [121], microdrilling [122], light-driven micro-rotors [123] and even for laser cooling[1] [124]. With the possibility of having controlled radial, azimuthal or linear polarization, a robust technique for the generation of pure LG modes could have many applications in both science and engineering.

7.2 Part 2 Aims

Current techniques for the generation of LG modes mainly rely on the conversion of fundamental mode or plane wave inputs. The various approaches to mode-conversion all lead to imperfect LG outputs. Limited research has been performed in the area of intracavity LG mode generation by which clean modes can be obtained. The published research in this area does not, however, provide a simple selection mechanism for the desired mode order. The aim of this work was to selectively generate pure, low order LG modes in a robust set-up that could be used for both scientific and future industrial applications.

[1] Generation and trapping of Bose-Einstein condensates (BECs) by laser-Doppler momentum transfer, not optical cooling by anti-Stokes fluorescence.

7.3 Part 2 Outline

Section 7.4 of this chapter reviews the historical background to LG mode generation. The theory of LG modes is developed in Section 7.5 where a mathematical description for LG modes is extended to the two techniques for LG mode generation that were investigated in this project: astigmatic mode-conversion and use of a ring-shaped pump beam.

Chapter 8 of this thesis reports experiments performed using a novel hollow-core-fibre beam-shaping technique for ring-pumped intracavity LG mode generation. The output achieved using this method is compared to that from an astigmatic mode-converter. Applying this same mode-converter as a diagnostic to analyze the ring-pumped LG output, some new insights into the properties of cavity LG modes are presented and discussed.

Chapter 9 concludes Part 2 by reviewing the effectiveness of the hollow-core-fibre beam-shaping technique for LG mode generation. Possible avenues for future research are discussed.

7.4 Historical Background

The first detailed theoretical analysis relating to the generation of LG modes was performed by Tamm & Weiss in 1990 [125]. A separate theory of LG mode generation was developed by Abramochkin & Volostnikov 1991 [126]. In this 1991 paper the authors present the first experimental data for LG mode generation using an astigmatic mode-converter. Although the presented data shows conversion of various HeNe TEM_{nm} modes to closed structures, these are clearly not perfect rings and the modes – if indeed they are really LG in nature – are of extremely poor quality. The theoretical work performed by Tamm & Weiss was generalized by Allen *et al.* in 1992 [127]. Also proposed in this paper is an improved design for an astigmatic mode-converter. In 1993 Beijersbergen *et al.* performed these experiments using a HeNe laser source [128]. The obtained modes results more closely resemble

rings than those presented by Abramochkin & Volostnikov, but are still of poor quality. The investigation by Beijersbergen *et al.* did, however, involve a rigorous empirical analysis of the mode-converter using various azimuthal input angles for the TEM_{nm} modes and a second mode-converter was employed to prove that the process was indeed reversible. The detail of these experiments supports the conclusion that the generated modes were really LG in nature. This was the first convincing demonstration of LG mode generation.

An alternative approach to introducing the azimuthal phase-shift intrinsic to an LG mode is to use a spiral phaseplate that gives varying phase retardation around a fundamental mode input beam. Beijersbergen *et al.* first demonstrated such a phaseplate in 1994 [129]. Although the authors successfully applied the technique to generate ring modes using the fundamental mode output from a HeNe laser, the segmented nature of a practical phaseplate limited the achievable mode purity. Two years later Turnbull *et al.* performed similar experiments [130]. The reported 'hot spots' in the phase-shifted output from an InP Gunn diode oscillator clearly show the performance limiting nature the phaseplate approach to LG mode generation. The design and manufacture of spiral phaseplates has significantly improved over the subsequent two decades, however fabrication issues still limit the usefulness of this technique [131].

At the same time as mode converters and spiral phaseplates were being developed, holograms began to be explored as an interferometric method for generating LG modes. In 1992 Heckenberg *et al.* published clear proof-of-principle data [132] using a fundamental mode HeNe beam passed through a patterned Fresnel plate. The output, although not of uniform intensity, had a clear ring structure. The absence of a detailed intensity profile or further empirical analysis in the results presented by Heckenberg *et al.* leaves questions as to whether the generated mode was purely LG in nature. Holographic LG mode generation is currently used for most practical applications.

The techniques discussed above all rely on the conversion of TEM_{nm} beams to generate the LG modes. The practical constraints of beam manipulation mean that such modes cannot be as pure as those generated within a laser cavity. This was

appreciated by Harris *et al.* who in 1994 reported single-mode LG operation in an argon-ion laser [133]. This was achieved by including a circular absorber in the laser cavity to suppress the fundamental mode and employing an aperture to spatially select the first order LG mode. Higher order LG_{02} and LG_{03} modes were also observed, but insufficient evidence is offered for the conclusion that these were pure (i.e. did not contain lower order mode components). The authors verified the LG nature of the output using an interference analysis. In the course of their study Harris *et al.* noted that a single-frequency laser cavity operating on an LG mode had an equal probability of having a sense of phase that is left- or right-handed.

Progress in the area of LG mode generation stagnated over the following decade, the work that was published focusing on refining the fabrication of components for TEM_{nm} mode-conversion. It was not until 2005 that Bisson *et al.* advanced intracavity LG mode generation by ring-pumping a Nd:YAG laser [134]. This beam-shaping was achieved by defocusing a diode pump source. This resulted in poor beam quality and limited the modal selectivity that could be achieved. In other recent progress a biaxial cystal has been used for intracavity mode-conversion [135] and, in a similar approach to that by Harris *et al.*, a cavity mirror defect employed to suppress the TEM_{00} mode [136].

7.5 Theory

This section of the thesis first discusses the general theory of Laguerre-Gaussian modes. This theory is developed to present a detailed mathematical analysis of the two methods for generating LG modes that were studied in this work: astigmatic mode-conversion and ring-pumping. Holographic and spiral phaseplate generation of LG modes are not considered within the scope of this work, however for completeness their theory is summarized in Appendix A.

7.5.1 General Theory

Laser beams typically have intensity profiles that are described by a coherent superposition set of Hermitian-Gaussian (TEM_{nm}) modes. Another complete set of solutions to the wave equation describing the cylindrically symmetric case are the Laguerre-Gaussian (LG_{pl}) modes.

A unique property of LG modes is that they have a $2\pi l$ azimuthal phase shift around the beam, where the index l is an integer describing the order of the mode. This leads to a helical structure in the temporal phase profile of the beam (Figure 7.1). The Poynting vector connects points of equal intensity and thus maps out the temporal evolution of a phase front. Consequently the phase structure in LG modes may be described by a Poynting vector that spirals around the propagation axis [137]. Except for the fundamental LG_{0l} mode (LG_{00} = TEM_{00}), this phase-shift results in a singularity at the centre of the beam and all higher order LG modes have an annular structure.

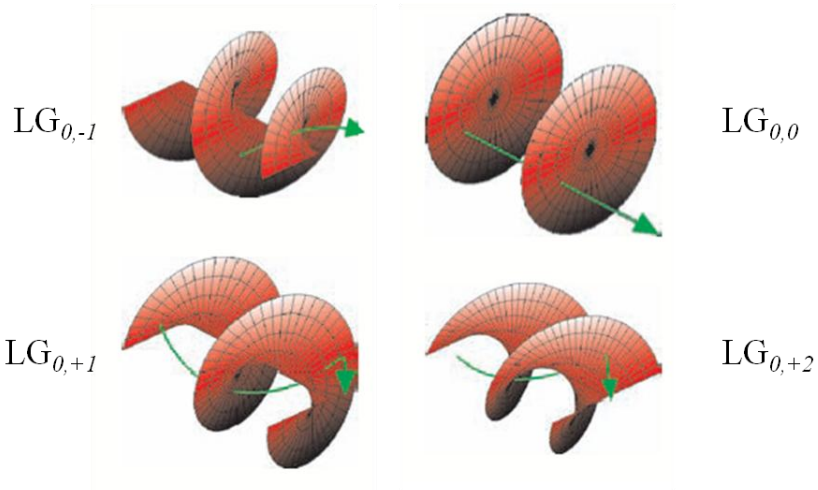

Figure 7.1 – *Helical phase structure of LG_{00}, LG_{01} and LG_{02} modes showing the two senses of phase (l = ±1) for the LG_{01} case; the green arrow represents the Poynting vector* [138].

Mathematical Description

LG modes can be described mathematically [139] by modulating the amplitude function *A* of the fundamental Gaussian mode by a periodic function of the azimuthal angular variable φ given in Equation 7.1.

$$\varphi = \tan^{-1}\frac{k_x}{k_y} \tag{7.1}$$

where k_x and k_y are the *x* and *y* components of the wavevector respectively.

Applying the identity:

$$k_x \pm ik_y = \sqrt{k_x^2 + k_y^2}\cdot e^{\pm i\varphi} \tag{7.2}$$

this modulation is equivalent to using an amplitude function that is proportional to:

$$A(k_x, k_y) \propto (k_x + ik_y)^p \cdot (k_x - ik_y)^{p+l} \tag{7.3}$$

Thus it is shown that the amplitude function for a LG mode has an angular-dependence described by a function of the variable φ. Applying this to the fundamental mode field distribution:

$$E \propto \iint\limits_{(k_x^2+k_y^2)\leq k^2} \frac{A(k_x,k_y)}{4\pi^2}\exp\left(k_x x + k_y y + \sqrt{k^2 - k_x^2 - k_y^2}\cdot z\right)\ dk_x dk_y \tag{7.4}$$

substituting Equation 7.3 into 7.4 an expression for the amplitude of the electric field *E* can be obtained:

$$E_{p,l} \propto \iint\limits_{-\infty}^{\infty} \frac{1}{4\pi^2}(k_x + ik_y)^p (k_x - ik_y)^{p+l} e^{i(S)} dk_x dk_y \tag{7.5}$$

where *p* and *l* are the LG mode indices and $S = k_x x + k_y y + \sqrt{k^2 - k_x^2 - k_y^2}\cdot z$.

Equation 7.5 may be simplified as:

$$E_{p,l} \propto E_0 \cdot (\partial_x + i\partial_y)^p \cdot \left(\partial_x - i\partial_y\right)^{p+l} \tag{7.6}$$

where E_0 is the Gaussian electric field amplitude distribution for a beam of radius w and Rayleigh range Z_R:

$$E_0 = \frac{1}{w}\exp\left(-ikz - \frac{x^2+y^2}{w^2} - i\psi\varsigma\right) \tag{7.7}$$

In Equation 7.7 the term $\psi = 2p + l + 1$ is equivalent to the M^2 parameter, w is the 1/e mode radius and ς is the Gouy phase shift.

The Laguerre polynomials are the set of canonical solutions to the second-order linear differential Laguerre equation:

$$xy`` + (1-x)y` + ny = 0 \tag{7.8}$$

and are defined by Rodrigues' formula:

$$L_p^l(x) = \frac{e^x}{p!}\frac{d^n}{dx^n}(e^{-x}x^n) \tag{7.9}$$

Substituting Equation 7.7 into 7.6, applying the definition of the Laguerre polynomials, converting to cylindrical (r,φ,z) coordinates and simplifying the constants in a single factor C, the electric field amplitude distribution for an LG mode is then given by:

$$E_{p,l} = \frac{C}{w}\exp(\pm il\varphi)\left(\frac{2r^2}{w^2}\right)^{|l/2|} L_p^l\left(\frac{2r^2}{w^2}\right)\exp\left(-ikz - \frac{r^2}{w^2} - i\psi\varsigma\right) \tag{7.10}$$

In the case discussed in this work that the index p is zero (single radial node), the Laguerre polynomial is unity and Equation 7.10 simplifies to:

$$E_{p,l} = \frac{C}{w}\exp(\pm il\varphi)\left(\frac{2r^2}{w^2}\right)^{|l/2|}\exp\left(-ikz - \frac{r^2}{w^2} - i\psi\varsigma\right) \tag{7.11}$$

This is the general equation for a LG_{0l} mode.

Angular Momentum

A spiralling Poynting vector (Figure 7.1) has components not only in the direction of propagation z but also azimuthally φ. This means that there is an azimuthal dependence to the energy flux. As electromagnetic energy E and momentum ρ are related by the equation:

$$E = \rho c \tag{7.12}$$

a LG mode clearly carries angular momentum. This is termed the *orbital* angular momentum as distinct from the polarization dependent photon *spin* angular momentum. Drawing an analogy between paraxial optics and quantum mechanics, the term $e^{\pm il\varphi}$ in Equation 7.10 is the eigenfunction to the angular momentum operator. The orbital angular momentum will thus be quantized at a value $l\hbar$.

On interaction with matter the angular momentum carried by a LG beam may be usefully transferred to molecules. This allows suitably high order beams (i.e. carrying significant angular momentum) to be used for applications where particles need to be trapped or moved. This is most frequently encountered in the field of biophysics where biological molecules require non-contact manipulation (optical tweezers). Three dimensional trapping of particles in a Steinmetz solid potential well has a role to play in the fine positioning of particles for nuclear fusion and collider experiments. Another use of blue-detuned LG modes is for laser-Doppler cooling and trapping of Bose-Einstein condensates (BEC).

7.5.2 Astigmatic Mode-Conversion

A Laguerre-Gaussian mode may be considered as a superposition of Hermitian-Gaussian modes combined with suitable relative phase (Figure 7.2). The link between the TEM_{nm} and LG_{pl} indices is given by the relationships:

- $l = | n - m |$
- $p = \min(n,m)$

from which it follows that the LG_{00} and TEM_{00} modes must be equivalent. All higher order LG modes will display the characteristic annular structure. As only the zeroth order p index modes (single radial node) are considered in the following analysis, to simplify the notation the LG modes are expressed in this section only by the n,m indices rather than $p,\pm l$.

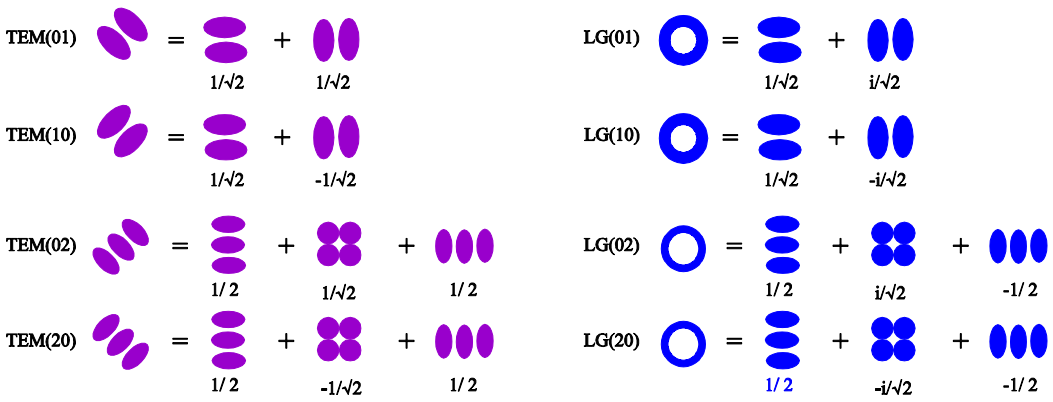

Figure 7.2 – *Decomposition of $TEM_{01,10}$, $TEM_{02,20}$, $LG_{01,10}$ and $LG_{02,20}$ modes into their respective HG superposition sets, where the TEM and LG modes are defined in terms of the n,m indices.*

A TEM_{0m} mode with its principal axis aligned at 45^o to the x-y axes can be decomposed into a set of Hermitian-Gaussian modes aligned with the x-y axes. Figure 7.2 shows that this decomposition is identical to that for an LG_{0m} (/LG_{m0}) mode except that the components are all in phase. Introducing a $\frac{\pi}{2}$ phase shift between successive component modes in a 45^o oriented TEM_{0m} mode will thus generate the superposition mode set of the LG_{0m} mode.

The relationship between LG_{nm} and TEM_{nm} (HG) modes is given by [126, 127]:

$$LG_{nm}(x,y,z) = \sum_{j=0}^{N} i^j \cdot b(n,m,j) \cdot HG_{N-j,j}(x,y,z) \tag{7.13}$$

where $N = n + m$, $i = \sqrt{-1}$ and the coefficient b is defined as:

$$b(n,m,j) = \left(\frac{(N-j)!\,j!}{2^N n!\,m!}\right)^{1/2} \times \frac{1}{j!}\frac{d^j}{dt^j}\left[(1-t)^n \times (1+t)^m\right]_{t=0} \tag{7.14}$$

The coefficient i^j corresponds to the $\pm\frac{\pi}{2}$ phase shift between successive superposition modes.

To introduce the required phase shift between the x-components and y-components of a beam, an astigmatic set-up can be used. If two cylindrical lenses are used to focus and re-collimate a circularly symmetric beam, an astigmatism will exist between the lenses only. The Guoy phase ζ of a beam is [140]:

$$\zeta = \left(n + \frac{1}{2}\right)\zeta_x + \left(m + \frac{1}{2}\right)\zeta_y = \tan^{-1}\left(\frac{z}{Z_R}\right) \tag{7.15}$$

Thus the x-components and y-components of an astigmatic beam ($\zeta_x \neq \zeta_y$) will experience different Guoy phase shifts over the astigmatic region. If the parameters of the incident beam and focusing lenses are selected such that the difference in phase shift between the components is $\frac{\pi}{2}$, a LG mode will be generated.

To successfully recombine the astigmatic components, the transverse radii of the x- and y-components must be matched at two lenses separated by a distance *2d*:

$$\frac{Z_{Rx}^2 + d^2}{Z_{Rx}^2} = \frac{Z_{Ry}^2 + d^2}{Z_{Ry}^2} \tag{7.16}$$

In addition the input and output beams must be mode-matched, requiring the focal length *f* of the lenses to be [127, 128]:

$$f = \left(\frac{d}{Z_{Rx}^2 + d^2} - \frac{d}{Z_{Ry}^2 + d^2} \right)^{-1} \tag{7.17}$$

Substituting for Equation 7.17, 7.16 may be reduced to:

$$Z_{Rx} = \left(\frac{d^2 - {}^{d^3}/_{f}}{1 + {}^{d}/_{f}} \right)^{1/2} = d \times \left(\frac{1 - {}^{d}/_{f}}{1 + {}^{d}/_{f}} \right)^{1/2} = d \times B \tag{7.18}$$

and

$$Z_{Ry} = \left(\frac{d^2 + {}^{d^3}/_{f}}{1 - {}^{d}/_{f}} \right)^{1/2} = d \times \left(\frac{1 + {}^{d}/_{f}}{1 - {}^{d}/_{f}} \right)^{1/2} = \frac{d}{B} \tag{7.19}$$

From symmetry arguments, the introduced difference in Guoy phase shift between the two components will be:

$$\Delta\zeta = \Delta\zeta_x - \Delta\zeta_y = 2 \times \left[\tan^{-1}\left(\frac{d}{Z_{Rx}} \right) - \tan^{-1}\left(\frac{d}{Z_{Ry}} \right) \right] \tag{7.20}$$

Substituting for Equations 7.18 and 7.19 this simplifies to:

$$\Delta\zeta = 2 \times \left[\tan^{-1}\left(\frac{1}{B}\right) - \tan^{-1}(B)\right] \tag{7.21}$$

showing that the difference in Guoy phase shift is dependent only on the selected lens focal length and lens spacing. Also demonstrated is that the introduced phase-shift may range from $0 \rightarrow \pi$. Achieving a $\frac{\pi}{2}$ phase shift thus requires that the condition be satisfied:

$$d = \frac{f}{\sqrt{2}} \tag{7.22}$$

For a cylindrical lens with its astigmatism in the y-axis, Equation 7.19 for mode-matching requires that the incident symmetric beam has a Rayleigh range:

$$Z_{Ry} = f + d = \left(1 + \frac{1}{\sqrt{2}}\right) \times f = Z_{Rx} \tag{7.23}$$

Applying the conditions in Equations 7.22 and 7.23 a practical mode-converter can be designed.

It is important to note that mode-conversion is a reversible process and that an incident LG mode will lose its relative phase-shift across such an astigmatic region. The resultant output will be a TEM_{0m} mode at 45^{o} to the x-y axes.

7.5.3 Ring Pumping

Most published techniques for intracavity mode generation rely on suppression of the TEM_{00} central intensity maximum [133, 141]. An alternative technique first demonstrated by Bisson *et al.* in 2005 [134] is to use ring-pumping so that no gain is generated at the centre of the pumped region. This work improves upon the experiments performed by Bisson *et al.* by using a novel beam-shaping method to give a pump beam of good quality. The ring is formed by transmitting light from a

diode pump source through the inner-cladding of a hollow-core-fibre. If a high beam quality fibre-coupled diode pump source is used, the dimensions of the hollow-core-fibre can be selected to preserve beam quality and simple, adjustable telescoping can then be used to control the pump spot size in the gain medium. As presented in the following derivation, a LG mode of desired order can thereby be selected.

It can be seen from Equation 7.11 that as the order of the mode l increases, the $1/e^2$ mode radius b increases and the thickness of the ring $b - a$ as a fraction of the mode radius decreases (Figure 7.3), where a is the inner radius at which the pump intensity drops to $1/e^2$. Thus by carefully selecting the dimensions of the pump beam to match the desired LG_{0l} mode, any mode may be individually selected. The ratio $\frac{b-a}{b}$ of the ring thickness to the mode radius may also be used as a diagnostic for identifying the order of an imaged mode.

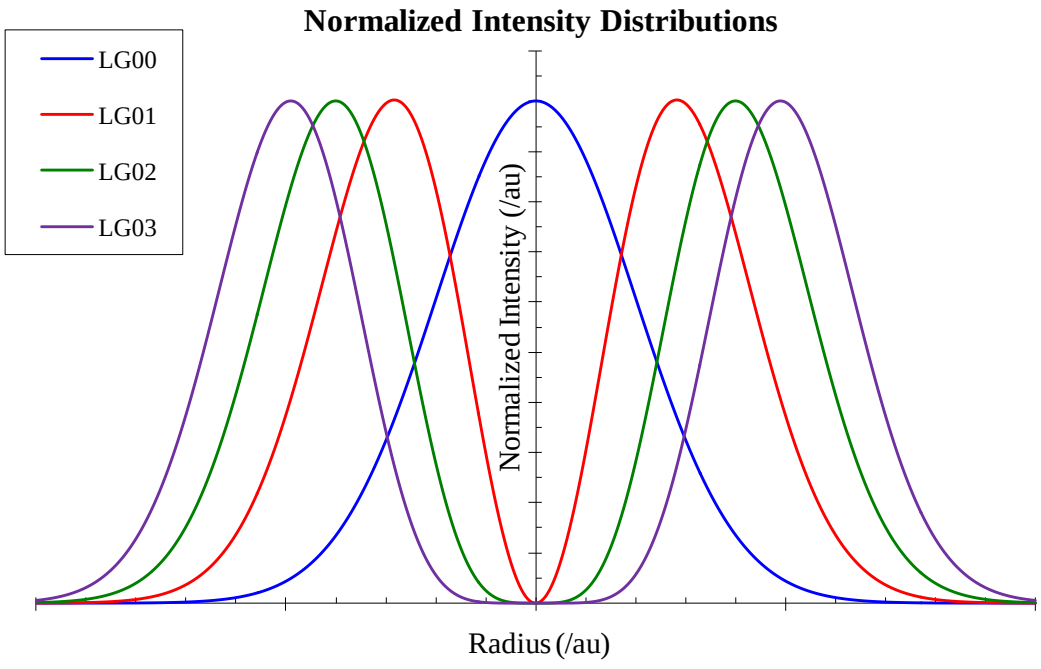

Figure 7.3 – *Normalized intensity distributions for the LG_{00} (fundamental), LG_{01}, LG_{02} and LG_{03} modes showing the different positions and relative thicknesses of the rings.*

The threshold for a four-level laser system is given by [142]:

$$P_{th} = \frac{\pi\left(\frac{hc}{\lambda_p}\right)\left(L + T + 2\sigma_a f_L N l_c\right)}{4\sigma_e \tau_f \left(f_L + f_U\right)\eta_{abs} \cdot \left(\frac{\lambda_p}{\lambda_L}\right) \cdot \eta_{ov}} \tag{7.24}$$

where λ_p and λ_L are the pump and laser wavelengths respectively, L and T are the percentage loss and output coupling respectively, σ_a and σ_e are the absorption and emission cross-sections, f_L and f_U are the fractional populations in the upper and lower lasing levels respectively, N is the dopant concentration, l_c is the resonator cavity length, τ_{fl} is the fluorescence lifetime, η_{abs} is the pump absorption efficiency and η_{ov} is the overlap efficiency.

The overlap efficiency η_{ov} is a term that describes how well the pump and laser mode profiles are superposed and is defined as:

$$\eta_{ov} = \int_{cavity} s\,(r, \varphi, z) \cdot r_p(r, \varphi, z)\, dV \tag{7.25}$$

where s and r_p are the cavity mode and photon density distributions respectively.

A poor overlap efficiency means that either not all of the laser mode is being pumped or much of the pump is being wasted. The pump profile may be selected, as in the case of ring-pumping, such that a desired mode experiences a good overlap (LG_{0l}) and the undesired mode experiences a poor overlap (TEM_{00}). In this case the desired ring mode will reach threshold first and deplete the gain, thereby suppressing the undesired fundamental mode.

For a TEM$_{00}$ beam with a top-hat pump:

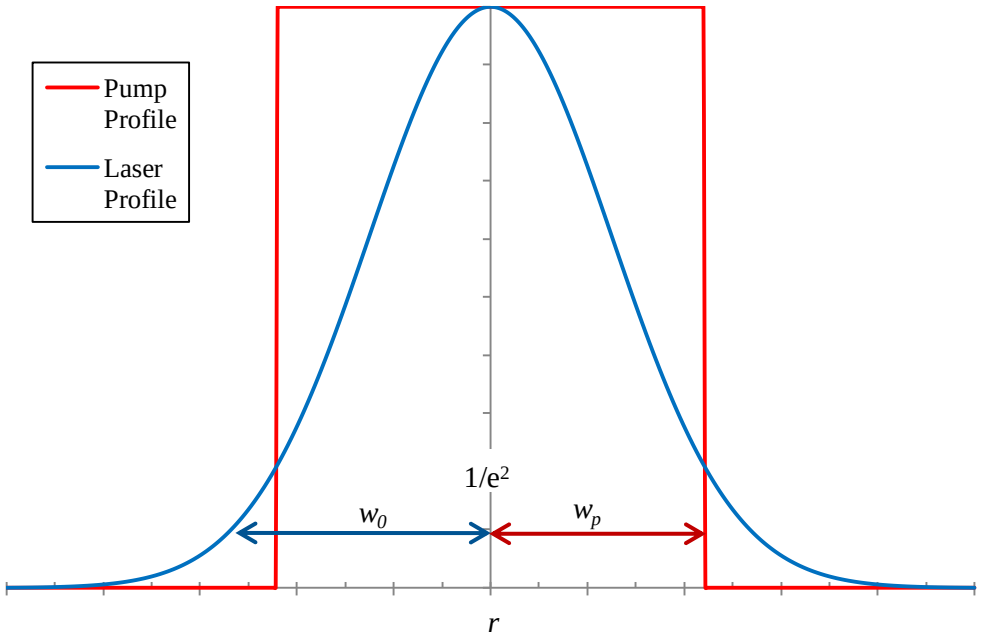

Figure 7.4 – *A TEM$_{00}$ mode with a top-hat pump showing the 1/e^2 pump w_p and laser w_0 mode radii respectively.*

$$s = \frac{2}{\pi w_0^2 L_c} \exp\left(\frac{-2r^2}{w_0^2}\right) \tag{7.26a}$$

$$r_p = \frac{\alpha_p e^{-\alpha_p z}}{\pi w_p^2 \eta_{abs}} \qquad r \leq w_p \tag{7.26b}$$

$$r_p = 0 \qquad elsewhere$$

where L_c is the length of the gain medium, w_0 and w_p are the 1/e^2 cavity mode and pump spot radii respectively, α_p is the absorption coefficient and η_{abs} is the absorption efficiency. Thus the overlap integral is:

$$\eta_{ov} = \frac{1}{\pi w_p^2 L_c}\left[1 - \exp\left(\frac{2w_p^2}{w_0^2}\right)\right] \tag{7.27}$$

For a LG_{0l} mode with a top-hat ring pump of inner radius *a* and outer radius *b*:

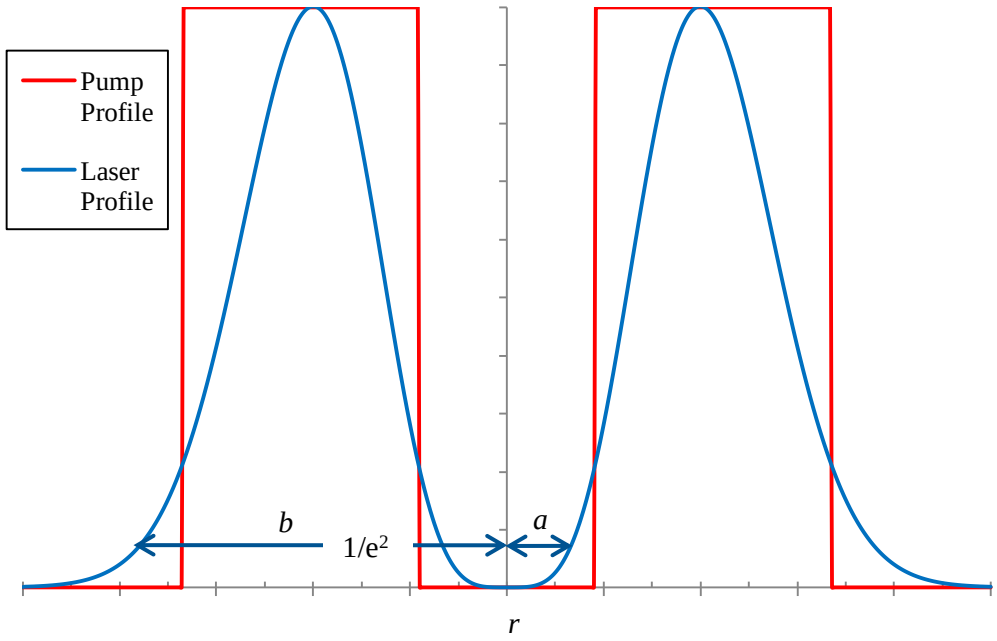

Figure 7.5 – *A LG_{01} mode with a top-hat ring-pump showing the inner 'a' and outer 'b' laser mode radii respectively.*

$$s = \frac{2}{l!\,\pi w_0^2 L_c}\left(\frac{2r^2}{w_0^2}\right)^l \exp\left(\frac{-2r^2}{w_0^2}\right) \tag{7.28a}$$

$$r_p = \frac{\alpha_p e^{-\alpha_p z}}{\pi(b^2 - a^2)\eta_{abs}} \qquad a \le r \le b \tag{7.28b}$$

$$r_p = 0 \qquad elsewhere$$

Thus the overlap integral is:

$$\eta_{ov} = \frac{1}{\pi(b^2 - a^2)L_c}\sum_{i=0}^{l}\frac{1}{(l-i)!}\left[\left(\frac{2a^2}{w_0^2}\right)^{l-i}\exp\left(\frac{-2a^2}{w_0^2}\right) - \left(\frac{2b^2}{w_0^2}\right)^{l-i}\exp\left(\frac{2b^2}{w_0^2}\right)\right] \tag{7.29}$$

Substituting Equation 7.29, the threshold for a ring pumped laser operating on a LG_{0l} mode may be easily calculated from the standard equation for the lasing threshold (Equation 7.24):

$$P_{th}^{LG} = \frac{\pi\left(\frac{hc}{\lambda_p}\right)(L + T + 2\sigma_a f_L n_L L)}{4\sigma_e \tau_f f_U \eta_{abs} \cdot \frac{\lambda_p}{\lambda_L}} \times \frac{1}{\frac{1}{\pi(b^2-a^2)L_c}\sum_{i=0}^{l}\frac{1}{(l-i)!}\left[\left(\frac{2a^2}{w_0^2}\right)^{l-i}\exp\left(\frac{-2a^2}{w_0^2}\right) - \left(\frac{2b^2}{w_0^2}\right)^{l-i}\exp\left(\frac{2b^2}{w_0^2}\right)\right]} \tag{7.30}$$

Taking Equations 7.27 and 7.29, the ratio of the LG_{0l} to the fundamental mode threshold pump power is given by:

$$\frac{P_{th}^{00}}{P_{th}^{LG}} = \frac{(b^2 - a^2)}{w_p^2} \frac{1 - \exp\left(\frac{-2w_p^2}{w_0^2}\right)}{\sum_{i=0}^{l}\frac{1}{(l-i)!}\left[\left(\frac{2a^2}{w_0^2}\right)^{l-i}\exp\left(\frac{-2a^2}{w_0^2}\right) - \left(\frac{2b^2}{w_0^2}\right)^{l-i}\exp\left(\frac{2b^2}{w_0^2}\right)\right]} \tag{7.29}$$

Figure 7.6 shows plots of the threshold pump powers for different LG_{0l} modes for two pump spot sizes. These plots show that it is possible to selectively excite individual LG_{0l} modes by careful ring pumping.

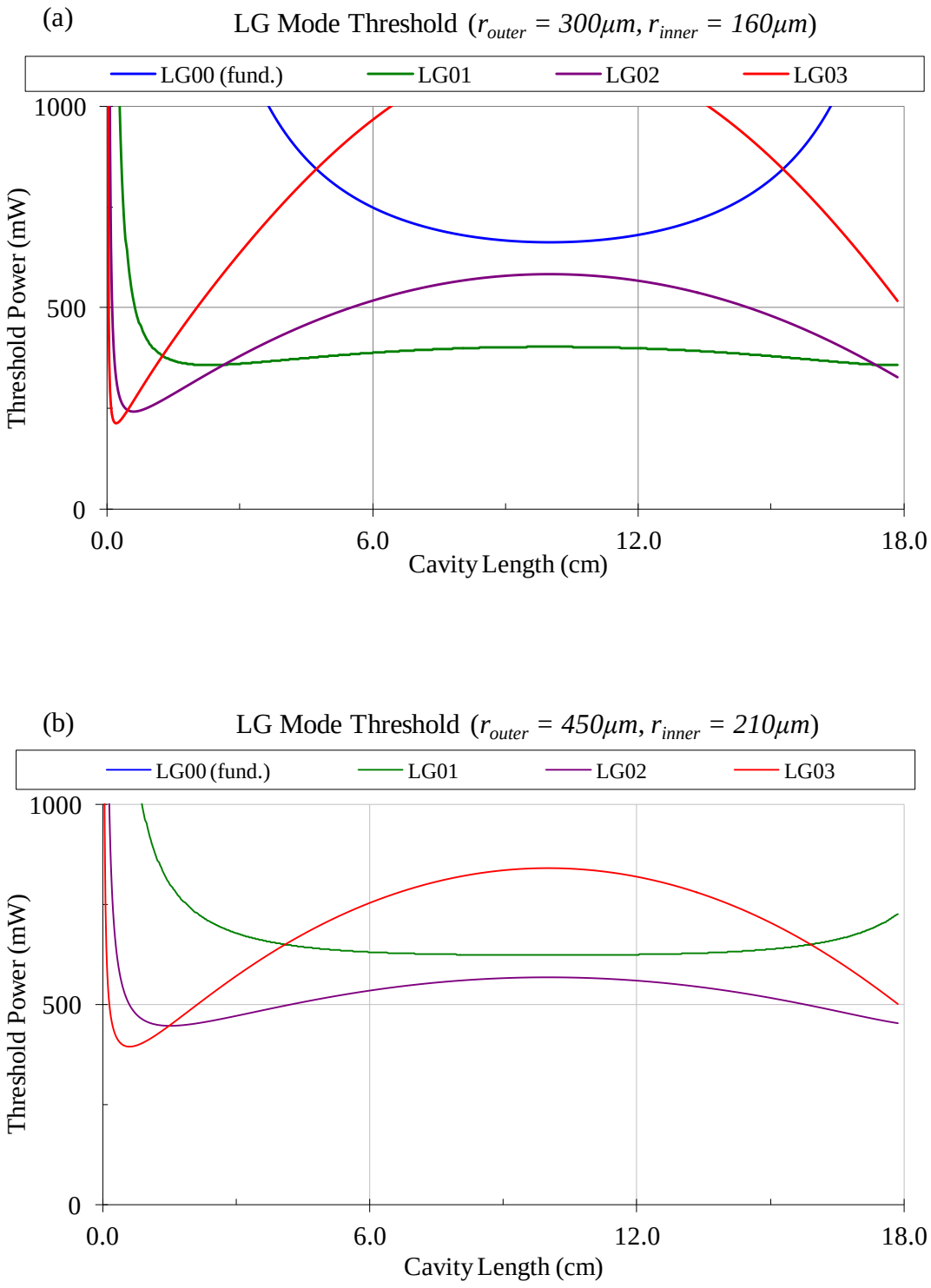

Figure 7.6 – *Plots of the LG_{00} (fundamental), LG_{01}, LG_{02} and LG_{03} mode lasing thresholds for (a) 300μm and (b) 450μm outer radius ring-pumped LG mode cavities.*

Chapter 8

Generation of Laguerre-Gaussian Modes

This chapter covers the investigation of Laguerre-Gaussian (LG) modes that are selectively generated by ring-pumping a gain medium. In Section 8.1 the novel approach developed in this work of using a hollow-core-fibre for shaping the pump beam is validated as a technique for generating high purity LG modes. As discussed in Sections 7.1 and 7.5.1, a LG mode has a $2\pi l$ azimuthal phase-shift around the beam leading to a Poynting vector that spirals around the propagation axis. The directionality of the Poynting vector can thus be used to define a LG mode as having either a left-handed or right-handed 'sense of phase'. Section 8.2 presents a hypothesis that each longitudinal mode in a resonator cannot simultaneously support LG modes having opposite senses of phase. If a single longitudinal mode were a superposition of two LG modes with opposite senses of phase, the resultant mode would be a lobed TEM_{nm} structure. A Fabry-Pérot cavity was used with an astigmatic mode-converter based on the theory described in Section 7.5.2 to split each longitudinal mode generated using the set-up in Section 8.1 into its constituent TEM_{nm} components. The results of this analysis validate the above hypothesis. During the course of this investigation some additional insights were gained into the nature of cavity LG modes. These are discussed in Section 8.3.

8.1 Laguerre-Gaussian Mode Generation

A *Lumics* 125µm-core, 0.15 NA fibre-coupled 0.808µm diode laser[1] with a maximum specified output power of 4W and an M^2 parameter of 36.3 was focused into the 200µm-diameter, 0.46 NA silica inner-cladding of a passive optical fibre[2] having a 105µm-diameter hollow core. In this arrangement a 1.16W ring-shaped output beam could be obtained. To improve the efficiency of this beam-shaping technique, the hollow-core-fibre was tapered by heating the fibre in a splicer to collapse the hole (Figure 8.1). This enabled all of the pump output to be coupled into the hollow core fibre. In the ideal case the coupled light would then be guided around the expanding hole. There was, however, still significant loss over the short taper length which was not optimized for these initial experiments. Nevertheless a 25% improvement in transmitted power was achieved (P_t = 1.45W). The ring-shaped output was collimated using a 60mm focal length spherical lens. Attenuating this beam with two mirrors having 90% transmission at 1.064µm and a sequence of neutral density (ND) filters, the shaped output was viewed using a *Spiricon IEEE-1394 (LBA-FW-SCOR20)* CCD digital camera (Figure 8.2). The ring-shaped pump beam had a measured M^2 parameter of 75.2. This was found by focusing the output through an 80mm focal length spherical lens and measuring the beam size around the waist position (/focal plane) using a *DataRay Inc. BeamScope*^{TM}*-P7* silicon two-slit beam profiler. Taking data over the region for which the paraxial approximation holds, a quadratic line of best fit based on a least squares fit analysis (Figure 8.3) could be used to find the spot size and Rayleigh range. Applying Equation 3.1 the M^2 parameter could then be calculated.

[1] model: LU0808T040

[2] The author gratefully acknowledges John Hayes for fabricating the fibre. Fibre code: A0032.

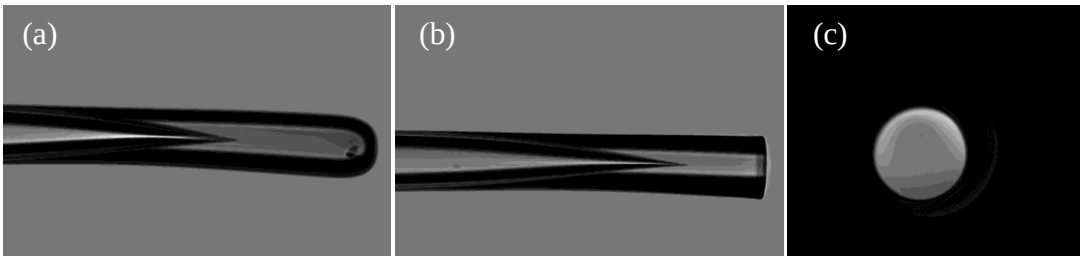

Figure 8.1 – *(a) Tapered, (b) tapered and cleaved, (c) cleaved end-face views of the hollow-core-fibre.*

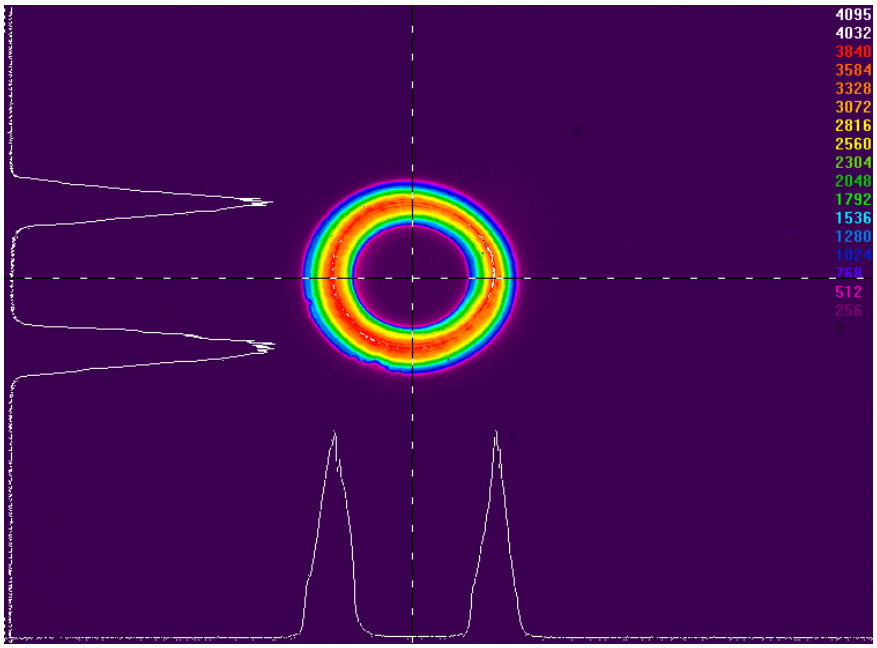

Figure 8.2 – *Hollow-core-fibre beam-shaped pump.*

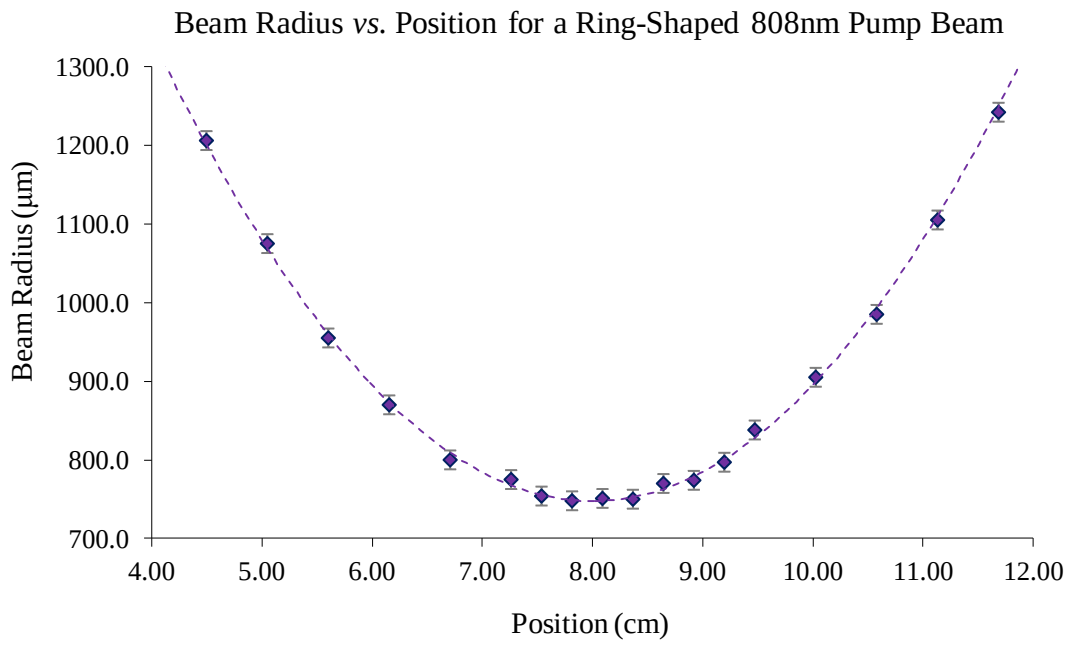

Figure 8.3 – *A plot of beam radius vs. position within the Rayleigh range for the ring-shaped 808nm output of a 200μm-cladding, 105μm-core hollow core fibre with* $M^2 = 75.2$. *The ±12μm uncertainty corresponds to fluctuations in the beam radius measured using a two-slit beam profiler.*

The ring-shaped pump beam was slightly defocused to give a diverging output. An 80mm lens was used to focus the pump into a 3mm × 10mm Nd:YAG rod. This was supported in a water cooled copper mount held at 17°C. Adjusting the distance *s* between the collimating and focusing lenses, the overlap between the pump and laser modes could be controlled. A 130mm long resonator was built using a plane input coupler having high transmission at 0.808μm and high reflectivity at 1.064μm. The resonator was completed with a 200mm ROC 3% output coupler at 1.064μm (Figure 8.4). The average pump radius in the gain medium at $1/e^2$ intensity was then set at 340μm to optimize overlap with the LG_{01} resonator mode that was calculated using an ABCD ray matrix method.

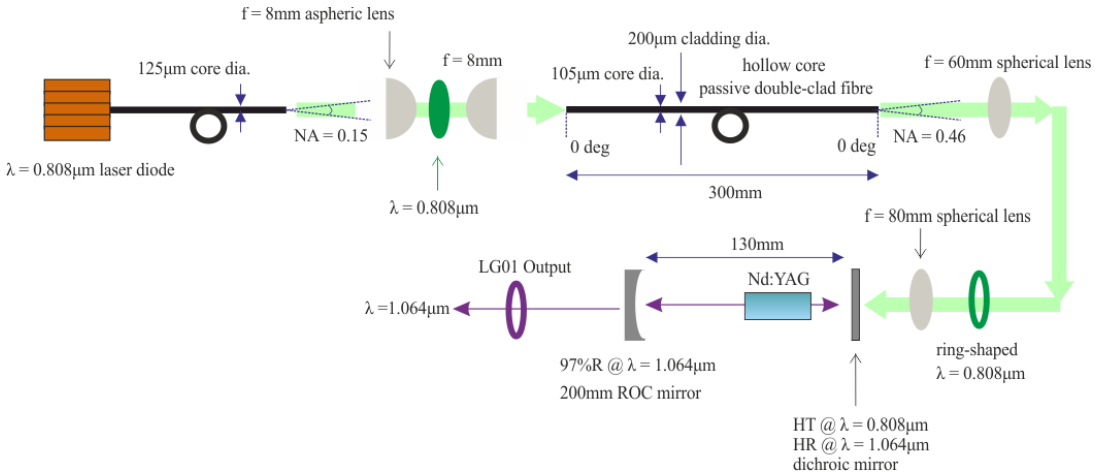

Figure 8.4 – *Experimental schematic for ring-pumped LG_{0l} mode generation in a Nd:YAG laser. The 0.808μm pump beam is shaped using a 300mm length of 200μm-cladding, 105μm-core hollow core optical fibre.*

Using this pump scheme, a ring-mode was generated (Figure 8.5). This had a measured M^2 parameter of 2.05 found using the experimental procedure described above (Figure 8.6). This is in close agreement with the theoretical[3] M^2 of 2 for a LG_{01} mode. The threshold power of 411mW was found by investigating the pump power for which relaxation oscillations were first observed. This was performed by monitoring on a *Tektronix TDS5053B* digital oscilloscope the output attenuated using two mirrors having 90% transmission at 1.064μm and detected using a *Thorlabs DET10A/M* nanosecond rise time silicon photodiode. This is consistent with that predicted for LG_{01} operation from Equation 7.30. The slope efficiency of this laser was measured to be 67% (Figure 8.7). The ratio (b-a)/b = 0.82 as defined in Section 7.5.3 also compares favourably with the theoretical value of 0.84 for the LG_{01} mode. This evidence all supports the conclusion that a pure LG_{01} mode was generated, validating the hollow-core-fibre approach for ring-pumping a laser gain medium as a technique for generating pure Laguerre-Gaussian modes.

[3] $M^2 = 2p + l + 1$

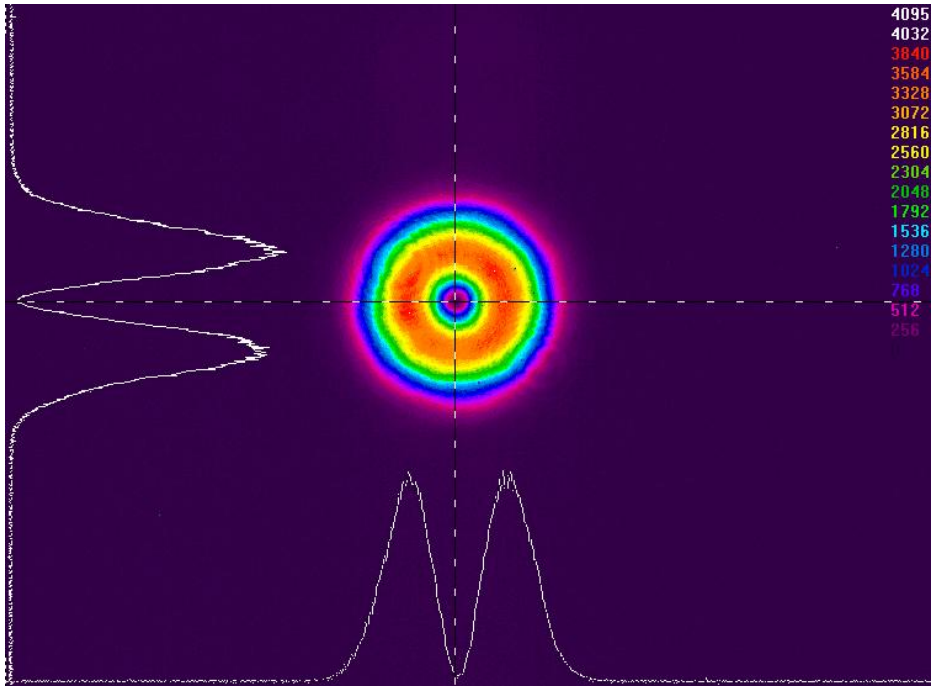

Figure 8.5 – *Ring-pumped LG_{01} mode 1.064μm output from a Nd:YAG laser.*

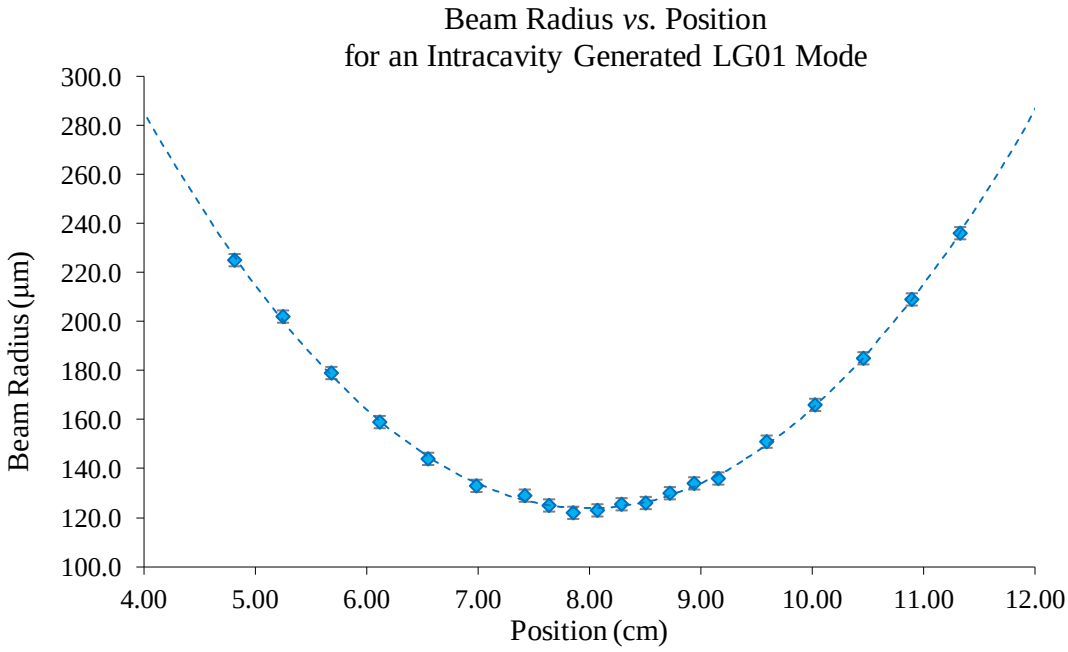

Figure 8.6 – *A plot of beam radius vs. position within the Rayleigh range for an intracavity generated LG_{01} mode with $M^2 = 2.05$. The ±2.5μm uncertainty corresponds to fluctuations in the beam radius measured using a two-slit beam profiler.*

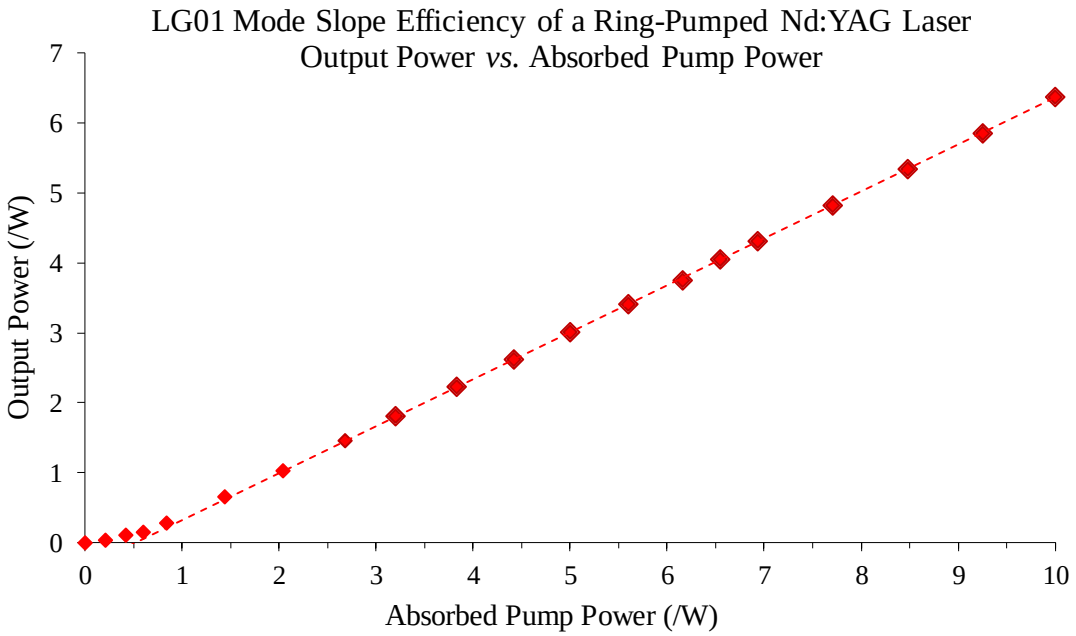

Figure 8.7 – *A plot of LG_{01} output power as a function of absorbed pump power for a ring-pumped Nd:YAG laser having a slope efficiency of 67% and a threshold of 411mW (found from relaxation oscillations).*

8.2.1 Sense of Azimuthal LG Phase - Hypothesis

From Equation 7.11, the azimuthal dependence of phase in a LG mode is described by the term:

$$e^{\pm il\varphi} \tag{8.1}$$

where l is the LG mode index and φ is the azimuthal variable.

Thus a superposition of a left-handed and a right-handed LG_{0l} mode will have an azimuthal phase dependence described by:

$$\Psi \cdot \Psi^* = \left(e^{+il\varphi} + e^{-il\varphi}\right) \times \left(e^{-il\varphi} + e^{+il\varphi}\right) = 4\cos^2(l\varphi) \tag{8.2}$$

where Ψ and Ψ^* represent the wavefunction and its complex conjugate respectively.

Equation 8.2 describes a mode with $2l$ lobes. The superposition mode will therefore be described by a Hermite-Gaussian function.

This mathematical consideration of the azimuthal phase dependence in a LG mode may be followed to the hypothesis that a single longitudinal mode in a resonator cannot simultaneously support LG modes having opposite senses of phase. This argument does not preclude the possibility of a resonator simultaneously supporting LG modes with different senses phase but at slightly different frequencies (/longitudinal modes).

The discussion above only considers the phase at a fixed plane along the propagation axis. There is an additional term for phase dependence with propagation:

$$e^{-ikz} \tag{8.3}$$

where k is the wavenumber.

The superposition of a left-handed and a right-handed LG_{0l} mode will thus have an azimuthal phase dependence that varies along the propagation axis described by:

$$\Psi \cdot \Psi^* = 4\cos^2(l\varphi + kz) \tag{8.4}$$

Equation 8.4 gives a mode in which the lobed structure described by Equation 8.2 rotates through 2π radians every half wavelength as it propagates along the z (i.e. reproduces itself every quarter wavelength). Thus for simple observation using a CCD camera, the time-averaged lobed superposition mode will appear to be a ring even though it is not a pure LG mode. Thus an alternative technique must be applied for verifying the above hypothesis.

As covered in Section 7.5.2 of the theory, a LG mode can be split into a TEM_{nm} superposition set with a suitable phase shift between the different component modes. Removing this phase shift, the resultant modes are the superposition set for a Hermite-Gaussian (HG) mode. As shown in Figure 7.2, LG modes with a left-handed sense of phase will split into a different superposition set to that for a right-handed LG mode. Thus removing the phase difference between the component modes using an astigmatic mode-converter, 'opposite' HG_{nm} modes (i.e. $\pi/2$ rotated, e.g. HG_{01} and HG_{10}) will be generated for left-handed and right-handed modes respectively. Isolating individual longitudinal LG modes by means of a Fabry-Pérot etalon, investigating the modes in this way can demonstrate conclusively whether a single longitudinal mode has both left-handed and right-handed LG components, only one component or flips between the two. An astigmatic mode-converter was therefore built in accordance with the theory described in Section 7.5.2 to prove the hypothesis that individual longitudinal modes can only have one sense of azimuthal phase.

8.2.2 Sense of Azimuthal LG Phase - Investigation

To fulfil the conditions described in Section 7.5.2 that are required to introduce a π/2 phase-shift to successive components in the TEM_{nm} superposition set for a HG mode, an astigmatic mode-converter must satisfy the criteria,

$$d = \frac{f}{\sqrt{2}} \tag{8.6}$$

$$Z_{Rx} = \left(1 + \frac{1}{\sqrt{2}}\right) \times f = Z_{Ry} \tag{8.7}$$

where d is the separation of the two astigmatic lenses having focal length f and Z_R is the Rayleigh range of the beam incident on the mode-converter. Satisfying Equation 8.5 introduces the π/2 phase shift between the components while Equation 8.6 must be fulfilled to correctly mode-match the incident and output beams.

The mode-converter built for this experiment used two cylindrical lenses having focal lengths of 50mm in the vertical direction. The separation of the lenses was set at 35mm to satisfy Equation 8.5. The cylindrically symmetric LG output from the Nd:YAG laser described in Section 8.1 was focused using a 60mm focal length spherical lens to a spot size (2w) of 480μm. This gave a Rayleigh range of 85mm – measured using the *BeamScope™-P7* twin-slit beam profiler – as required by applying Equation 8.6. The position of the focusing lens could be adjusted to optimize the spot size and thus Rayleigh range of the beam incident on the mode-converter.

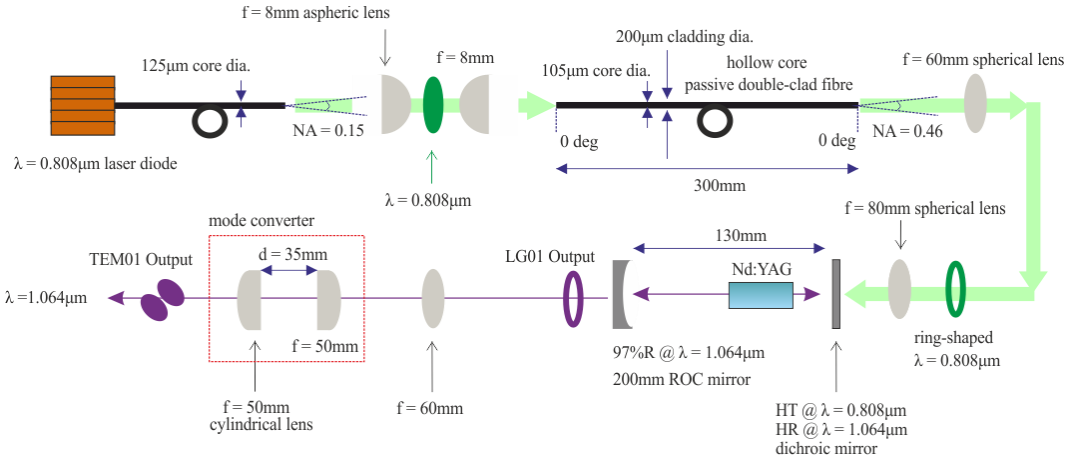

Figure 8.8 – *Schematic for a* $\frac{\pi}{2}$ *mode-converter.*

Placing a slit oriented at 45° to the vertical inside the Nd:YAG resonator (i.e. breaking the cylindrical symmetry of the cavity), TEM_{01} operation at 45° to the *x-y* axes could be selected. Using this well-defined mode as the input beam, the mode-converter could be optimized to give a ring output (Figure 8.9). It was observed that even slight variations in the orientation of the TEM_{01} (i.e. slit) had a significant impact on the mode-converter output. Although not quantified, the importance of correctly aligning the mode converter was highlighted. Comparing the slightly distorted ring mode in Figure 8.9 generated using an astigmatic mode-converter with the clean LG mode in Figure 8.5 generated using a ring-shaped pump beam to selectively excite the LG_{01} mode in a laser resonator, the improved performance of the latter technique in this instance can be seen. The distortions in the mode-converted output could be addressed by further optimization of the properties (i.e. angle, quality, Rayleigh range, spot size) of the input beam and of the mode converter itself (i.e. lens separation, lens alignment). Such improvements could make the outputs from the two techniques comparable, but ring-pumping clearly offers a simpler approach to achieving high quality LG modes.

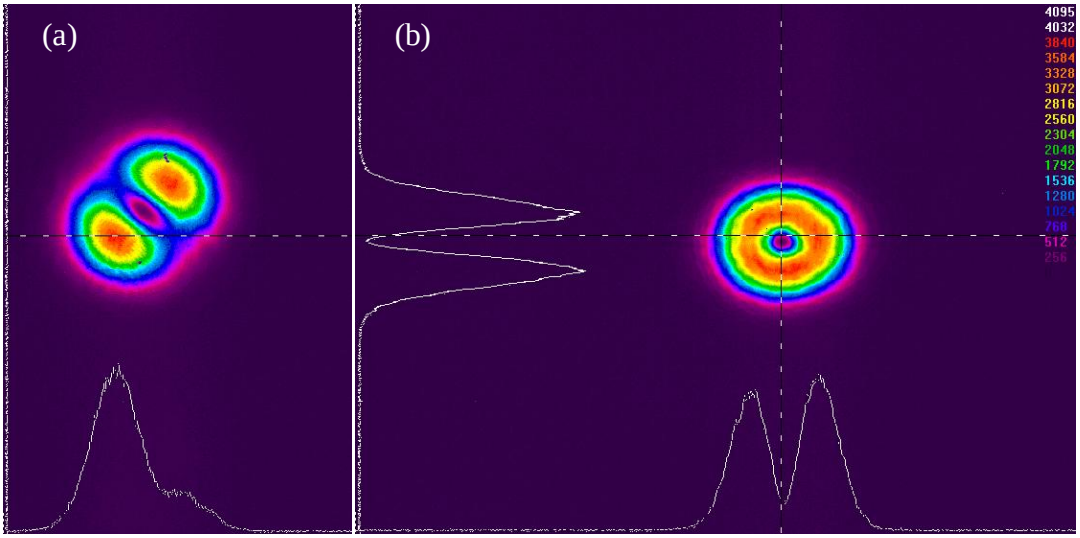

Figure 8.9 – *(a) Incident beam and (b) mode-converter output.*

To further verify the effectiveness of the astigmatic mode-converter, the LG output was retro-reflected through the mode-converter from the output waist position. The transmitted beam through an alignment mirror having 98% reflectivity at 1.064μm and attenuated using a sequence of ND filters was then imaged using the *Spiricon* CCD camera (Figure 8.10). The retro-reflected mode had been split into a TEM_{01} mode at 45^{o} to the axes with the same orientation as the input beam. This is as would be expected for a reversible process. An important point to note from observing the orientation of the TEM_{01} output is that it is in agreement with the theory that it is the orientation of the TEM_{nm} input beam controls the sense of phase of the LG output mode. Thus the astigmatic mode-converter built in this work was validated as a tool for investigating the LG output from a laser pumped using a ring-shaped beam.

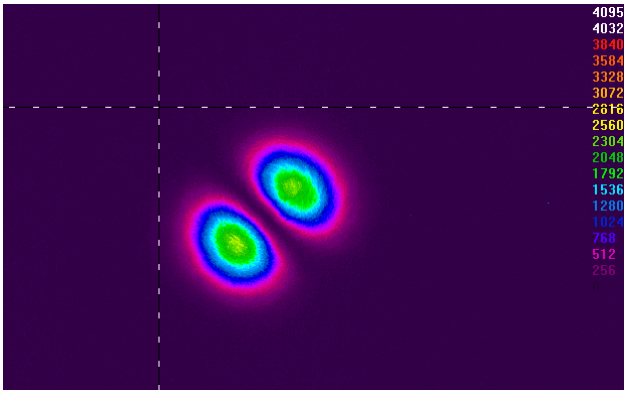

Figure 8.10 – *Mode-converter output for a retro-reflected, mode-converted beam.*

Removing the slit from the Nd:YAG cavity, the single-pass output from the mode-converter for an LG_{01} incident beam was observed (Figure 8.11). As the slit had only been used to select the TEM_{01} mode used to align the mode-converter, no adjustment of the laser resonator was required. Except for a slight vertical distortion that could be explained by a slight azimuthal misalignment of the mode-converter lenses, the output was unchanged compared to the LG input beam (Figure 8.5). Repeating the alignment procedure to ensure that this was the true output from a well aligned mode-converter, it could be concluded that laser output incident on the mode-converter contained multiple LG modes having different senses of phase. In this scenario the superposition of the resultant mode-converted output HG modes rotated by 90^{o} with respect to each other would be a ring, although not a LG mode as the two HG components would be in phase. To confirm that this was the case and that the output was not flipping between orientations over a shorter period than the imaging time of the *Spiricon* CCD camera, one quadrant of the output was selected using an aperture and monitored on the *Tektronix* digital oscilloscope by means of the *Thorlabs* nanosecond rise time silicon photodiode detector. This was repeated for each quadrant of the mode. In all cases the intensity remained constant and the above conclusion that modes having opposite senses of phase were simultaneously present could be reasonably justified.

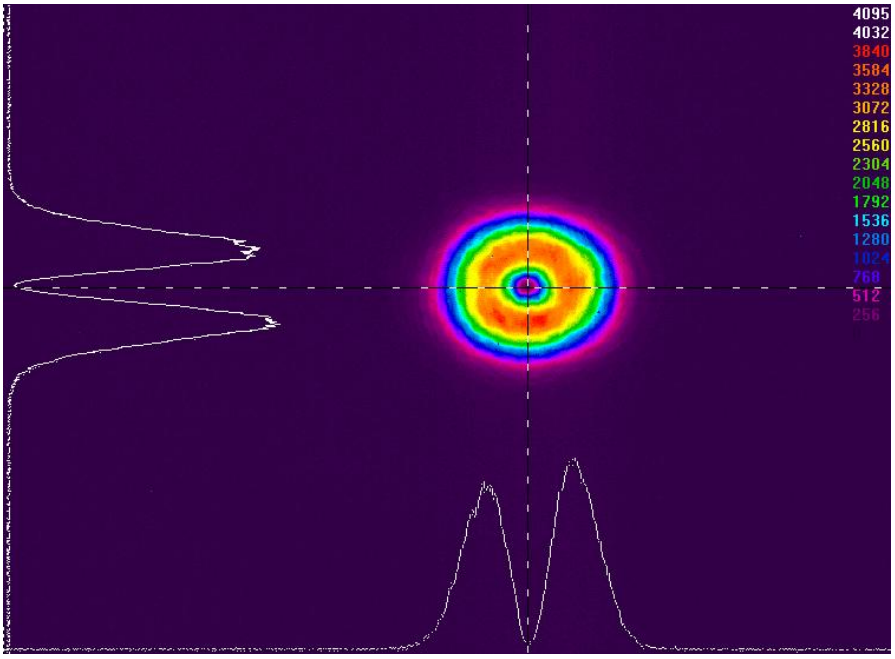

Figure 8.11 – *Output from a π/2 mode-converter for a 1.064μm wavelength LG_{01} mode input beam.*

To test the hypothesis in Section 8.2.1, the *Melles Griot FPI-25* scanning Fabry-Pérot interferometer used in the LMRT experiments was inserted with a mirror spacing of 5mm before the astigmatic mode-converter. Directly monitoring the output from the interferometer on an oscilloscope using a silicon photodiode, five longitudinal modes could be observed across the Nd:YAG laser gain spectrum. Whilst monitoring the oscilloscope trace, the length of the Fabry-Pérot etalon was then adjusted to match a single longitudinal laser mode. Removing the photodiode, the mode-converter output for this incident mode was again observed using the CCD camera. This process was repeated for each of the five longitudinal laser modes (Figure 8.12).

For each longitudinal mode a clear two lobed structure at 45^{o} to the *x-y* axes was observed. The vertical distortion that can be seen in Figure 8.12 is worse than that in the previous observations, but is probably due to poorer mode-matching as required by Equation 8.6 following the inclusion of the Fabry-Pérot etalon or an additional misalignment within the mode converter. The two outermost modes on each side of the gain spectrum had a well-defined, temporally stable sense of phase and thus a temporally stable corresponding HG_{nm} output. The mode at the central maximum, however, flipped between a HG_{01} and HG_{10} mode-converted output. At any one time, however, the central maximum did show a single sense of phase.

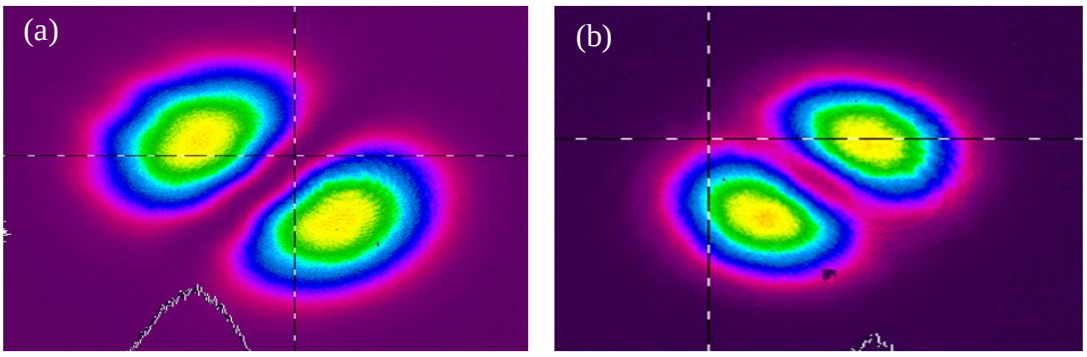

Figure 8.12 – *Mode-converter outputs on opposite sides of the laser spectrum corresponding to (a) left-handed and (b) right-handed senses of phase.*

This evidence supports the hypothesis presented in Section 8.2.1 that each longitudinal mode in a laser resonator cannot simultaneously support LG modes having opposite senses of phase. This evidence is in agreement with the findings of Harris *et al.* [15] who found that for a single-frequency gas laser pumped using a defocused ring-shaped beam the LG output always had a well-defined sense of phase. This work builds upon the findings of Harris *et al.* by demonstrating that their observation is in agreement with theory and is true for each longitudinal mode in a laser resonator. This work also demonstrates that while each frequency must have a well-defined sense of phase, different longitudinal modes may have different senses of phase and that this sense of phase may flip during laser operation.

8.3 Observations and Discussion

In the Nd:YAG laser used in this investigation, on each side of the gain spectrum the modes were observed to have the same sense of phase and this sense flipped around the central maximum. On one side of the gain spectrum all the modes would have a left-handed sense (Figure 8.12a) and on the other side all the modes would have a right-handed sense (Figure 8.12b). In general the central mode did not have a temporally stable sense of phase and continuously flipped between left-handed and right-handed operation. In repeat experiments, however, the central mode was occasionally observed to have a well-defined sense of phase. There is no evidence as to the cause of this, but it may be reasoned that this was due to a perturbation of the laser resonator leading to a given mode depleting the gain close to the centre of the gain spectrum.

To the best of my knowledge, there are two scenarios that could explain the observation that modes on opposite sides of the gain spectrum have different senses of phase:

1. The two senses of phase have slightly different emission cross-sections leading to an asymmetry around the gain peak (Figure 8.13).

2. Each longitudinal mode is in fact frequency split for the two senses of phase meaning that on opposite sides of the gain spectrum different modes are closest to the gain peak (Figure 8.14).

It must be emphasized that this work presents no physical explanation for either of these scenarios, however the effect of each would lead to the reported observations.

There is no theoretical basis for the former scenario, however the latter, although no physical mechanism has been identified, could possibly arise due to some astigmatic effect in the laser gain medium leading to the two senses of phase experiencing slightly different effective cavity lengths. In this event, the longitudinal modes for the left-handed and right-handed senses of phase would be slightly (i.e. much less than the free spectral range) separated. If for each longitudinal left-handed mode there were a right-handed mode of slightly higher frequency, at the lower frequency end of the gain spectrum the right-handed modes will be marginally closer to the gain peak while at higher frequency end the left-handed modes will be marginally closer to the gain peak (Figure 8.14). For each pair the mode closer to the gain peak would experience slightly higher gain. Having greater amplification, this mode would rapidly deplete the gain available to the other mode in the pair. A single longitudinal mode with a well-defined sense of phase would thus be supported by the laser resonator for each frequency-split pair. At the central maximum the left-handed and right-handed frequency-split modes would fall on opposite sides of the gain spectrum and thus experience similar gain. The competition between these modes would then account for mode flipping at the gain peak. As the two modes would have slightly split frequencies, this would not violate the argument in Section 8.2.1 of a single longitudinal mode requiring operation with a single sense of phase. The central laser mode would be switching rather than a single longitudinal LG mode

flipping senses. Although this discussion supports the conclusion that frequency splitting is the most likely cause of the observations reported in this work, no physical mechanism for this effect is being presented and this is therefore only a hypothesis requiring further investigation (see Chapter 9).

8.4 Summary

In this chapter the generation of Laguerre-Gaussian resonator modes by selective ring-pumping using the novel technique of hollow-core-fibre beam shaping has been demonstrated. The improved output achieved using this approach has been compared to that achieved by the more established technique of astigmatic mode-conversion. The sense of phase of individual longitudinal LG modes has been studied using an astigmatic mode-converter and substantive evidence provided that a single longitudinal mode can only operate with one sense of LG phase. An interesting relationship between the sense of phase of the LG modes and the laser gain spectrum has been reported and discussed.

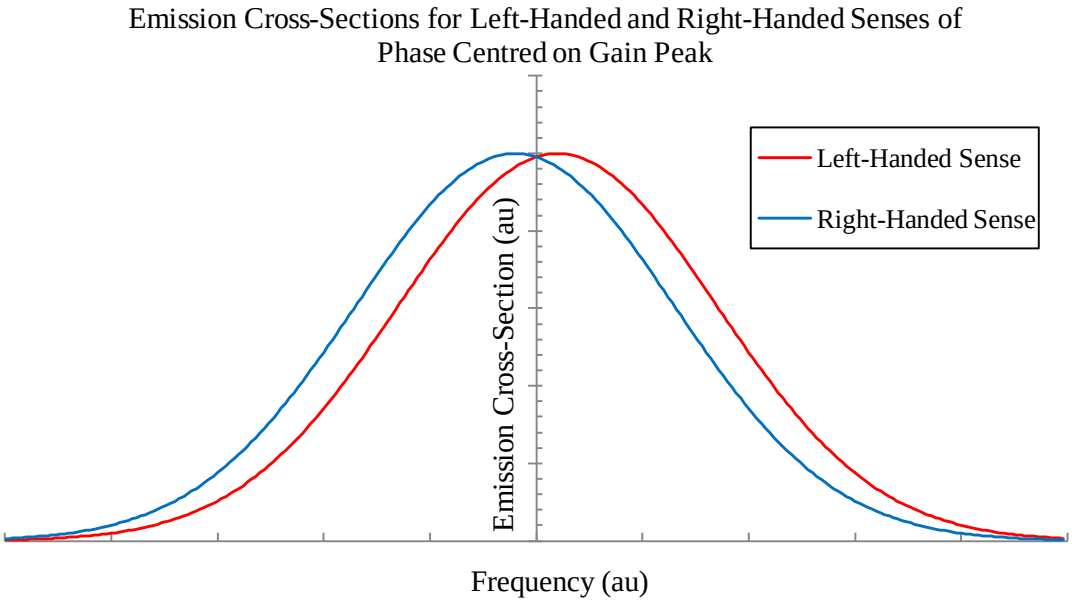

Figure 8.13 – *Mechanism for mode selection by differing cross-section showing higher cross-sections for left-handed and right-handed senses of phase on opposite sides of the gain spectrum.*

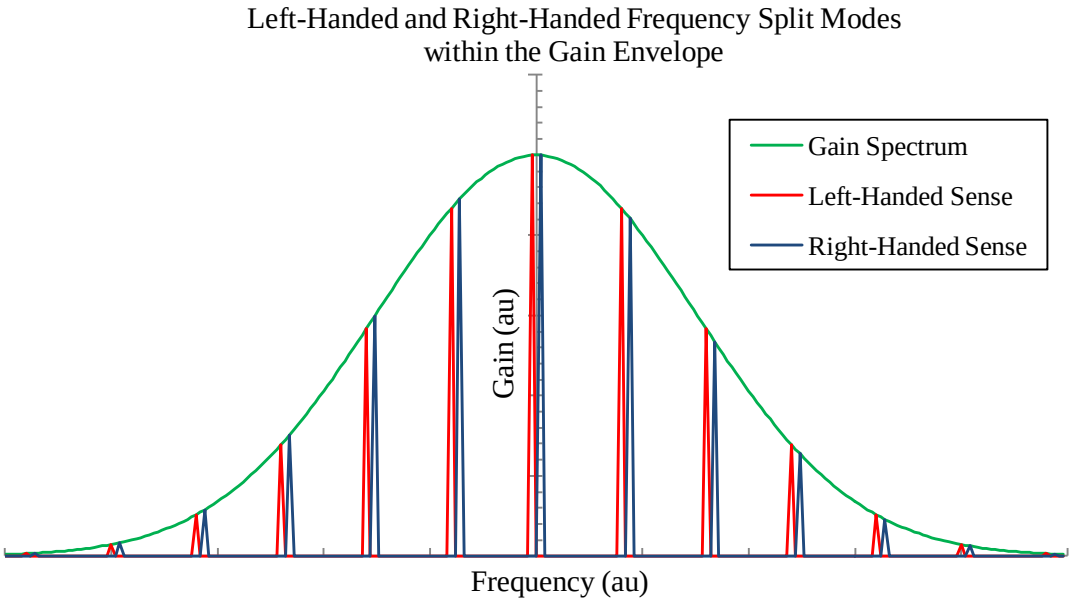

Figure 8.14 – *Mechanism for mode selection by frequency splitting of longitudinal modes showing higher gain for left-handed and right-handed senses of phase on opposite sides of the gain spectrum.*

Chapter 9

Conclusion and Future Work

9.1 Summary

A hollow-core-fibre has been used to generate a ring-shaped pump beam of controlled dimensions within a Nd:YAG bulk laser gain medium. This unique ability to pump a laser with a ring-shaped beam of reasonable quality has enabled pure, low order Laguerre-Gaussian modes to be selectively generated in good agreement with theory.

To investigate the sense of azimuthal phase of the longitudinal LG modes in a laser resonator, detailed analysis of the output beam was performed by using an astigmatic mode-converter to remove the $\pi/2$ phase shift between successive TEM_{nm} components. The form of the resultant Hermite-Gaussian mode then gave information as to the sense of phase of the incident LG modes. Employing a Fabry-Pérot etalon to isolate individual longitudinal modes, the hypothesis that each longitudinal mode can only have one sense of phase was verified.

The experiments to validate the above hypothesis also yielded some unexpected insights into the properties of LG resonator modes. It was observed that the modes on one side of the gain spectrum all had a particular well defined sense of phase whereas the modes on the other side all had the opposite sense of phase. It is hypothesized that this observation may be due to frequency splitting of the left-handed and right-handed LG modes, but no physical explanation for this has been found.

9.2 Future Work

Continuation of the study of LG modes begun in this work falls broadly into two categories: furthering the hollow-core-fibre LG mode generation technique and research that applies the generated modes.

For improving the LG mode generation technique, the first avenue of investigation should be to increase the available beam-shaped pump powers by reducing the hollow-core-fibre loss. This work would centre on extending the taper and improving its quality to ensure that minimal light was coupled into the non-guiding core. The second line of investigation, requiring fibre fabrication facilities, should involve optimizing the core-cladding ratio of the hollow-core-fibre to achieve the ideal mode-matching for higher order (thinner ring) modes. If these proposals were implemented to make the hollow-core-fibre beam-shaping technique more flexible, a wider range of pure LG modes could be investigated in further research. These higher order modes would also be of greater interest in practical applications as they carry more angular momentum.

Apart from applications that use the angular momentum of LG modes to manipulate molecules, the LG mode generation technique opens the possibility of designing a system that overlaps a LG_{0l} mode with a TEM_{00} mode. This could be used to achieve high quality top-hat beam profiles. Such beams would be useful in applications where temperature gradients are deleterious and uniform energy deposition is required.

The mode-conversion techniques and relatively poor quality outputs in published research have not allowed detailed, accurate investigations into the nature of LG modes to be previously performed. The unique ability that has been developed in this work to selectively generate pure resonator LG modes of low order offers wide scope for further study of their fundamental properties. In order to identify and potentially control the mechanism that leads to opposite senses of azimuthal phase being supported on different sides of the gain spectrum, further experiments should initially focus on detecting the frequency separation between the competing modes at the gain

peak. This could be performed using the scanning Fabry-Pérot interferometer for mode selection and a radio frequency spectrum analyzer. If a stable, small frequency difference that is much less than the free spectral range is measured, it would support the hypothesis presented in Section 8.3 that frequency splitting is responsible for the observed effect. Such evidence would not, however, be in itself conclusive nor would it give any insight into the physical mechanism behind this effect. Were frequency splitting of the two senses of phase proven to be the cause of the observations presented in this work and were it able to be controlled, possibilities for a range of novel devices would be raised.

LG modes can be linearly, radially or azimuthally polarized (or a combination of these, i.e. unpolarized). The symmetry in the polarization of radially polarized beams makes them of particular interest in engineering. Thus the development of a selection mechanism for radial or azimuthal polarization in a stable ring-pumped resonator would have many practical applications. The theoretical property that a LG_{01} mode could be focused more tightly than a TEM_{00} beam is both of great scientific and practical interest. Q-switching, mode-locking and frequency conversion are just some of the other areas that could be explored now that a robust method for selective LG mode generation has been developed.

Apart from opening new avenues of research into cavity LG modes, the simple technique that has been developed for their generation will allow LG modes to be used in other fields of scientific discovery as well as for engineering applications. The non-contact trapping and particle manipulation capabilities that LG modes offer could benefit experiments ranging from nuclear fusion to biophysics, while the possibility of usefully employing LG beams for microengineering could advance areas of life from personal computers to medical care.

9.3 Concluding Remarks

Although the scope of the research into Laguerre-Gaussian modes covered in Part 2 of this thesis is in itself limited, the developed beam shaping technique establishes a foundation for further studies. Applying the methods demonstrated in this project not only offers the opportunity to further extend our understanding of Laguerre-Gaussian modes, but also to advance diverse fields of scientific research. Aside from such academic uses, in its potential application to engineering this work could one day form a part of changes that ultimately impact on our day-to-day lives.

Conclusion

This work has covered two distinct areas of laser physics: optical cooling of rare-earth-doped solids by anti-Stokes fluorescence and Laguerre-Gaussian mode generation. A novel laser-based technique for the measurement of temperature along any path within a transparent sample has been developed alongside a new method for selectively generating pure Laguerre-Gaussian laser modes. As discussed in Chapters 6 and 9 of this thesis, the work performed in these two areas will make very different contributions to scientific understanding and potential future research. For completeness, however, it is worth noting the direct links that may be drawn; particularly Laguerre-Gaussian pumping being used for the identification of optical cooling.

The temperature within a cylinder heated evenly at its surface will be uniform. Thus the temperature profile inside the region of an optically cooled sample that is pumped using a Laguerre-Gaussian beam is approximately uniform. This fact could be used to enable temperature measurement in the pumped region without suffering resolution-limiting aberrations. In the simple cooling investigations for which the longitudinal mode-shift relative thermometry technique was designed, such fine optimization is not required. In future optical cooling research or for the investigation of other transparent samples, however, this combination could usefully improve the resolution.

In developing a novel diagnostic for optical cooling, detecting local cooling in Yb^{3+}:CaF_2 and demonstrating a practical technique for the generation of Laguerre-Gaussian modes, this work has made only a limited contribution to our understanding of these two fields. It has, however, laid the groundwork for much future study in diverse areas of research and in this has made a novel and useful contribution to science.

Appendix

A. Holographic and Phaseplate Generation of LG Modes

Holographic Generation of LG Modes

The interference pattern between a LG mode of order *l* and a plane wave will be a chiral pattern (Figure A.1) described by:

$$l \cdot \varphi = \left(\pm n + \frac{1}{2}\right)\pi + \frac{k \cdot r^2}{2R} \tag{A.1}$$

where φ is the azimuthal angle, *k* is the wavenumber, *R* is the radius of curvature of the LG mode and the integer *n* describes the number of vortices in the interference pattern, its sign defining the direction of the vortices.

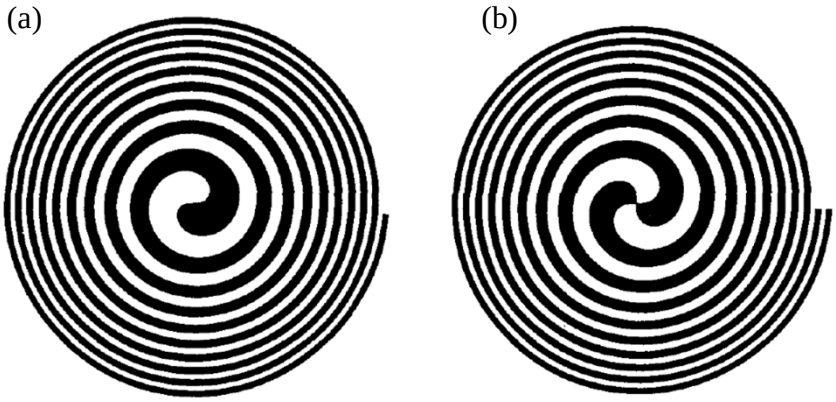

Figure A.1 – *Chiral interference pattern for a LG_{01} mode interfered with a plane wave at normal incidence for the (a) l = 1 and (b) l = 2 modes [132].*

If the two waves do not interfere at normal incidence but with some small offset angle γ, an extra term must be added to the equation for the interference pattern:

$$l \cdot \varphi = \left(\pm n + \frac{1}{2}\right)\pi + \frac{k \cdot r^2}{2R} + kr \sin\gamma \cos\varphi \qquad \text{(A.2)}$$

and the phase singularity will now appear as a fork with l prongs in a more conventional fringe pattern (Figure A.2):

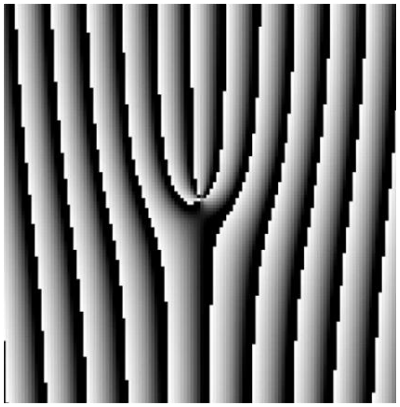

Figure A.2 – *Computer generated interference pattern showing the three 'prongs' of an $l = \pm 3$ LG mode interfered with a plane wave at a slight angle* [143].

If the interference pattern in Figure A.2 is printed onto a Fresnel zone plate and illuminated with a coherent plane wave at normal incidence, the resultant output will be an $l = \pm 3$ LG mode at the angle $\pm\gamma$ (Figure A.3). The direction of the angle will depend on the sense of phase of the output. By using such a hologram the left- and right-handed senses can be separated.

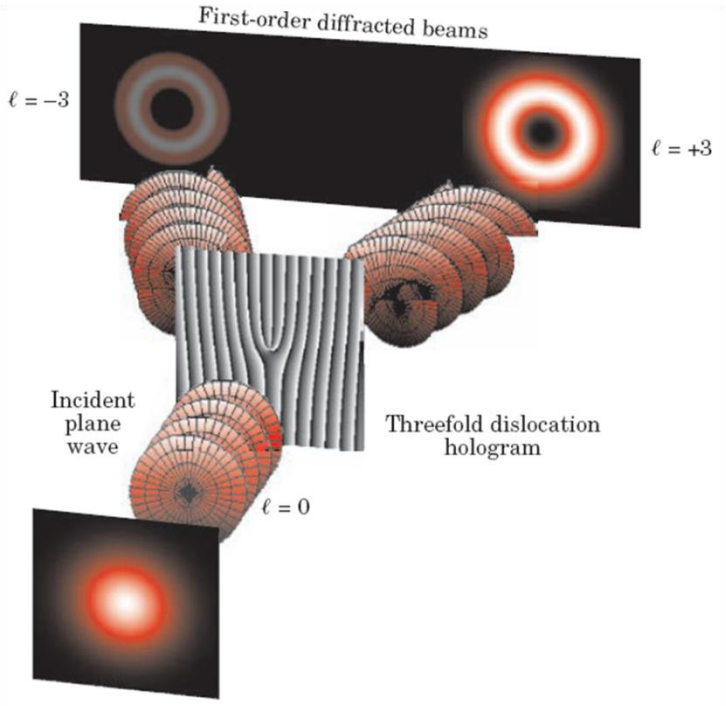

Figure A.3 – *Generation of l = ±3 LG modes using a computer generated hologram [138].*

Spiral Phaseplate Generation of LG Modes

A beam of wavelength λ passing through a medium of thickness h having refractive index n will have its phase ψ retarded by:

$$\Delta\psi = (n-1)h \times \frac{2\pi}{\lambda} \tag{A.3}$$

If the retarder is not of uniform thickness around the beam, then there will be an azimuthal φ dependence of the phase shift:

$$\Delta\psi(\varphi) = (n-1) \times (h - \Delta h(\varphi)) \times \frac{2\pi}{\lambda} \tag{A.4}$$

A phaseplate of smoothly varying thickness that satisfies the equation:

$$\int h(\varphi)\, d\varphi = l\lambda \tag{A.5}$$

where l is an integer will convert a plane phase front into an output that has a $2\pi l$ azimuthal phase shift around the beam. This will be an LG_{0l} mode.

Figure A.4 depicts a segmented spiral phaseplate in the ideal case that the segments combine to give a smoothly varying thickness.

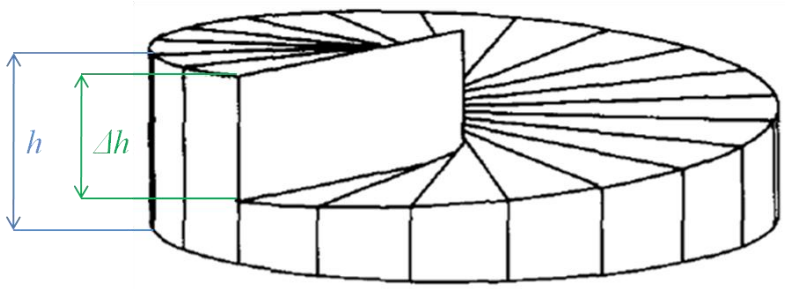

Figure A.4 – *A segmented spiral phaseplate for LG mode generation [129].*

In practice there will be a step change in thickness at each segment introducing aberrations into the LG output beam. The more segments that can be built into the phaseplate the smaller the individual step changes need to be and the closer the output from such a phaseplate will be to the ideal.

Bibliography – Part 1

1. D. V. Seletskiy, S. D. Melgaard, M. Sheik-Bahae, S. Bigotta, A. DiLieto, M. Tonelli, and R. I. Epstein, "Optical refrigeration breaks the Peltier barrier: cooling Yb:YLF to 155K," in *Laser Refrigeration Of Solids III*, (SPIE, 2010),
2. R. W. Wood, "Anti-Stokes radiation of fluorescent liquids," Phil. Mag. **6**(1928).
3. C. V. Raman and K. S. Krishnan, "A New Type of Secondary Radiation," Nature **121**, 501-502 (1928).
4. P. Pringsheim, "Zwei Bemerkungen über den Unterschied von Lumineszenz und Temperaturstrahlung," Z. Phys. **57**, 749-746 (1929).
5. S. Vavilov, "Some remarks on the Stokes law," J. Phys. (Moscow) **9**(1945).
6. P. Pringsheim, "Some remarks concerning the difference between luminescence and temperature radiation: Anti-Stokes fluorescence," J. Phys. (Moscow) **10**(1946).
7. S. Vavilov, "Photoluminescence and thermodynamics," J. Phys. (Moscow) **10**(1946).
8. L. Landau, "On the thermodynamics of photoluminescence.," J. Phys. (Moscow) **10**, 503-506 (1946).
9. A. Kastler, "Some suggestions concerning the production and detection by optical means of inequalities in populations of levels of spatial quantization of atoms," J. Phys. Radium **11**, 255-265 (1950).
10. K. Lehovec, C. A. Accardo, and E. Jamgochian, "Injected ligh emission of silicon-carbide crystals," Phys. Rev. **83**(1951).
11. J. R. Haynes and H. B. Briggs, "Radiation produced in germanium and silicon by electron-hole recombination.," Phys. Rev. **86**(1952).
12. R. Newman, "Optical studies of injected carriers. II: Recombination radiation in germanium," Phys. Rev. **91**(1953).
13. K. Lehovec, C. A. Accardo, and E. Jamgochian, "Light emission produced by current injected into a green silicon-carbide crystal," Phys. Rev. **89**(1953).

14. J. Tauc, "The share of thermal energy taken from the surroundings in the electroluminescent energy radiated from a p-n junction.," Czech. J. Phys. **7**(1957).
15. G. C. Dousmanis, C. W. Mueller, and H. Nelson, "Evidence of refrigerating action by means of photon emission in semiconductor diodes," Phys. Rev. **133**(1964).
16. M. A. Weinstein, "Thermodynamic limitation on the conversion of heat into light," JOSA **50**(1960).
17. S. Yatsiv, ed., *Anti-Stokes Fluorescence as a Cooling Process*, Advances in Quantum Electronics (Columbia University Press, New York, 1961).
18. H. E. D. Scovil and E. O. Schulz-DuBois, "Three-level masers as heat engines," Phys. Rev. Lett. **2**(1959).
19. O. Kafri and R. D. Levine, "Thermodynamics of adiabatic laser processes: Optical heaters and refrigerators," Opt. Comm. **12**(1974).
20. E. Geva and R. Kosloff, "The quantum heat engine and heat pump: An irreversible thermodynamic analysis of the three-level amplifier," J. Chem. Phys. **104**, 7681-7699 (1996).
21. J. P. Palao, R. Kosloff, and J. M. Gordon, "Quantum thermodynamic cooling cycle," Phys. Rev. E **64**, 056130/056131-056138 (2001).
22. C. E. Treanor, J. W. Rich, and R. G. Rehm, "Vibrational relaxation of anharmonic oscillators with exchange-dominated collisions.," J. Chem. Phys. **48**(1967).
23. J. T. Yardley, "Population inversion and energy transfer in CO Lasers," Appl. Opt. **10**(1971).
24. N. Djeu, "Laser cooling of gases by reradiation at higher frequency transitions," Opt. Comm. **26**(1978).
25. T. Kushida and J. E. Geusic, "Optical refrigeration in Nd-doped yttrium aluminium garnet," Phys. Rev. Lett. **21**(1968).
26. N. Djeu and W. T. Whitney, "Laser cooling by spontaneous anti-Stokes scattering," Phys. Rev. Lett. **46**(1981).
27. C. Zander, "Abkühlung einer Farbsofflösung durch Anti-Stokes-Fluoreszenz," (University of Siegen, Siegen, 1991).

28. C. Zander and K. H. Drexhage, *Cooling of a dye solution by anti-Stokes fluorescence.*, Advances in Photochemistry (Wiley, New York, 1995), Vol. 20.

29. R. I. Epstein, M. I. Buchwald, B. C. Edwards, T. R. Gosnell, and C. E. Mungan, "Observation of laser-induced fluorescent cooling of a solid," Nature **377**(1995).

30. B. C. Edwards, J. E. Anderson, R. I. Epstein, G. L. Mills, and A. J. Mord, "Demonstration of a solid-state optical cooler: An approach to cryogenic refrigeration," J. App. Phys. **86**, 6489-6493 (1999).

31. C. E. Mungan, M. I. Buchwald, B. C. Edwards, R. I. Epstein, and T. R. Gosnell, "Laser cooling of a solid by 16K starting from room temperature," Phys. Rev. Lett. **78**, 1030-1033 (1997).

32. X. Luo, M. D. Eisaman, and T. R. Gosnell, "Laser cooling of a solid by 21K starting from room temperature," Opt. Lett. **23**, 639-641 (1998).

33. T. R. Gosnell, "Laser cooling of a solid by 65K starting from room temperature," Opt. Lett. **24**(1999).

34. a. Rayner, N. R. Heckenberg, and H. Rubinsztein-Dunlop, "Condensed-phase optical refrigeration," JOSA B **20**, 1037-1053 (2003).

35. J. Thiede, J. Distel, S. R. Greenfield, and R. I. Epstein, "Cooling to 208K by optical refrigeration," Appl. Phys. Lett. **86**(2005).

36. B. Heeg, M. D. Stone, A. Khizhnyak, G. Rumbles, G. Mills, and P. A. DeBarber, "Experimental demonstration of intracavity solid-state laser cooling of Yb^{3+}:ZrF_4-BaF_2-LaF_3-AlF_3-NaF glass," Phys. Rev. A **70**, 021401(R) (2004).

37. G. L. Mills, W. S. Good, and A. J. Mord, "The Performance of the First Optical Refrigerator," in *4th Earth Science Technology Conference*, 2004),

38. D. V. Seletskiy, M. P. Hasselbeck, M. Sheik-Bahae, R. I. Epstein, S. Bigotta, and M. Tonelli, "Cooling of Yb:YLF using cavity enhanced resonant absorption - art. no. 69070B," in *Conference on Laser Refrigeration*, (SPIE, 2008), B9070.

39. D. V. Seletskiy, S. D. Melgaard, S. Bigotta, A. DiLieto, M. Tonelli, R. I. Epstein, and M. Sheik-Bahae, "Demonstration of an Optical Cryocooler," in *CLEO/QELS*, (IEEE, 2009), 2007-2008.

40. D. V. Seletskiy, S. D. Melgaard, M. Sheik-Bahae, S. Bigotta, A. DiLieto, and M. Tonelli, "Laser Cooling of a Semiconductor Load Using a Yb:YLF Optical Refrigerator," in *Laser Refrigeration Of Solids III*, (SPIE, 2010),
41. S. R. Bowman, "Lasers without internal heat generation," IEEE J. Quantum Electron. **35**, 115-122 (1999).
42. G. Nemova and R. Kashyap, "Yb3+-doped fiber laser with integrated optical cooler," in *Laser Technology For Defense And Security*, (SPIE, 2010),
43. J. Fernandez, A. Mendioroz, A. J. Garcia, R. Balda, and J. L. Adam, "Anti-Stokes laser-induced internal cooling of Yb^{3+}-doped glasses," Phys. Rev. B **62**, 3213-3217 (2000).
44. A. Mendioroz, J. Fernandez, M. Voda, M. Al-Saleh, and R. Balda, "Anti-Stokes cooling in Yb^{3+}-doped KPb_2Cl_5 crystal," Opt. Lett. **27**, 1525-1527 (2002).
45. S. Bigotta, D. Parisi, L. Bonelli, A. Toncelli, M. Tonelli, and A. DiLieto, "Spectroscopic and laser cooling results on Yb3+-doped BaY2F8 single crystal," J. App. Phys. **100**(2006).
46. J. Fernandez, A. Mendioroz, A. J. Garcia, R. Balda, and J. L. Adam, "Laser-induced internal cooling of Yb^{3+}-doped fluoride-based glasses," J. Alloys. Compounds **323-4**, 239-244 (2001).
47. S. R. Bowman and C. E. Mungan, "New materials for optical cooling," Appl. Phys. B **71**, 807-811 (2000).
48. M. T. Murtagh, G. H. Siegel Jr., J. C. Fajardo, B. C. Edwards, and R. I. Epstein, "Laser-induced fluorescent cooling of rare-earth-doped fluoride glasses," J. Non-Cryst. Solids **253**, 50-57 (1999).
49. J. Fernandez, A. Mendioroz, A. J. Garcia, R. Balda, J. L. Adam, and M. A. Arriandiaga, "On the origin of anti-Stokes laser induced cooling of Yb^{3+}-doped glass," Opt. Mater. **16**, 173-179 (2001).
50. J. Fernandez, A. J. Garcia-Advea, and R. Balda, "Anti-Stokes laser cooling in bulk erbium-dooped materials," Phys. Rev. Lett. **97**, 033001/033001-033004 (2006).
51. G. Nemova and R. Kashyap, "Laser cooling of Er3+-doped solids," Opt. Comm. **283**, 3736-3739 (2010).

52. C. W. Hoyt, M. P. Hasselbeck, M. Sheik-Bahae, R. I. Epstein, S. R. Greenfield, J. Thiede, J. Distel, and J. Valencia, "Advances in laser cooling of thulium-doped glass," JOSA B **20**, 1066-1074 (2003).

53. C. W. Hoyt, M. Sheik-Bahae, R. I. Epstein, B. C. Edwards, and J. E. Anderson, "Observation of anti-Stoke fluorescence cooling in thulium-doped glass," Phys. Rev. Lett. **85**, 3600-3603 (2000).

54. S. Bigotta, "Energy transfer and cooling processes in rare-earth doped insulating crystals," (University of Pisa, Pisa, 2004).

55. W. Patterson, S. Bigotta, M. Sheik-Bahae, D. Parisi, M. Tonelli, and R. I. Epstein, "Anti-stokes luminescence cooling of Tm3+ doped BaY2F8," Opt. Express **16**, 1704-1710 (2008).

56. F. Mandl, *Statistical Physics*, 2nd ed. (Wiley, Cichester, 1997).

57. L. N. Vikhor and L. I. Anatychuk, "Theoretical evaluation of maximum temperature difference in segmented thermoelectric coolers," Appl. Therm. Eng. **26**, 1692-1696 (2006).

58. V. S. Letkohov, V. G. Minogin, and B. D. Pavlik, "Cooling And Trapping Of Atoms And Molecules By A Resonant Laser Field," Opt. Comm. **19**, 72-75 (1976).

59. L. E. Erickson, "On anti-stokes luminescence from Rhodamine 6G in ethanol solutions," J. Lumin. **5**, 1-13 (1972).

60. X. Xiaodong, Z. Zhiwei, X. Jun, and D. Peizhen, "Crystal growth and sectral properties of $Yb_3Al_5O_{12}$," J. Cry. Growth **257**, 272-275 (2003).

61. D. E. McCumber, "Einstein Relations Connecting Broadband Emission and Absorption Spectra," Phys. Rev. **136**, A954-A957 (1964).

62. L. DeLoach, S. A. Payne, L. L. Chase, L. K. Smith, W. L. Kway, and W. F. Krupke, "Evaluation of absorption and emission properties of Yb^{3+}-doped laser crystals for laser applications," IEEE J. Quantum Electron. **29**, 1179-1191 (1993).

63. W. Koechner, *Solid-State Laser Engineering*, 5 ed., Springer Series in Optical Sciences (Springer Verlag, Berlin and Heidelberg, 1999), Vol. 1.

64. B. Aull and H. P. Jenssen, "Vibronic interactions in Nd:YAG resulting in nonreciprocity of absorption and stimulated emission cross sections," IEEE J. Quantum Electron. **18**, 925-930 (1982).

65. S. A. Payne, J. A. Caird, L. L. Chase, L. K. Smith, and W. F. Krupke, "Spectroscopy and gain measurements of Nd^{3+} in SrF_2 and other fluoride-structurehosts," JOSA B **8**, 726-740 (1991).

66. W. E. Martin and D. Milam, "Analysis of the optical spectrum of Ho^{3+}in $LiYF_4$," IEEE J. Quantum Electron. **18**, 1155-1163 (1982).

67. K. J. Öberg and H. Lundberg, "Experimental transition probabilties and improved level energies in YbIII," Eur. Phys. J. D **42**, 15-34 (2006).

68. A. Straesser and M. Ostermeyer, "Theoretical investigation of feasibility of Yb:YAG as laser material for nanosecond pulse emission with large energies in the Joule range," Opt. Comm., 442-448 (2007).

69. R. I. Epstein, "Progress On Laser Cooling Of Rare-Earth Doped Solids," (University of New Mexico, Albuquerque, 2007).

70. D. C. Brown, R. L. Cone, Y. C. Sun, and R. W. Equall, "Yb:YAG absorption at ambient and LF cryogenic temperatures," IEEE J. Quantum Electron. **11**, 604-612 (2005).

71. T. Y. Fan, D. J. Ripin, R. L. Aggarwal, J. R. Ochoa, B. Chann, M. Tilleman, and J. Spitzberg, "Cryogenic Yb3+-doped solid-state lasers," IEEE J. Quantum Electron. **13**, 448-459 (2007).

72. V. Petit, P. Camy, J. L. Doualan, X. Portier, and R. Moncorge, "Spectroscopy of Yb^{3+}:CaF_2 : From isolated centers to clusters," Phys. Rev. B **78**(2008).

73. J. M. Baker and W. B. J. Blake, "Endor Of Yb-1733+ On Tetragonal Sites In Calcium Fluoride - Determination Of Crystal Field Parameters," in *R. Soc. London, Ser. A*, 1970),

74. R. W. Olson, R. F. Loring, and M. D. Fayer, "Luminescent solar concentrators and the reabsorption problem," Appl. Opt. **20**, 2934-2940 (1981).

75. J. C. Fajardo, G. H. Siegel Jr., B. C. Edwards, R. I. Epstein, T. R. Gosnell, and C. E. Mungan, "Electrochemical purification of heavy metal fluoride glasses for laser-induced fluorescent cooling applications," J. Non-Cryst. Solids **213-214**, 95-100 (1997).

76. B. Heeg, P. A. DeBarber, and G. Rumbles, "Influence of fluorescence reabsorption and trapping on solid-state optical cooling," Appl. Opt. **44**, 3117-3124 (2005).

77. H. Y. Zhang, R. T. Brundage, and W. M. Yen, "Cooperative Optical-Transitions In CaF2-Yb-3+," J. Lumin. **31-2**, 257-259 (1984).
78. K. M. Dinndorf, "Energy transfer between Thulium and Holmium in laser hosts," (M.I.T., Cambridge, Massachusetts, 1993).
79. D. L. Dexter and H. Schulman, "Theory of Concentration Quenching in Inorganic Phosphors," J. Chem. Phys. **22**, 1063-1070 (1954).
80. D. J. Zalucha, J. C. Wright, and F. K. Fong, "Energy-Transfer Upconversion In LaF3-Pr3+," J. Chem. Phys. **59**, 997-1001 (1973).
81. C. K. Asawa, "Temperature-Dependent Concentration Quenching Of Fluorescence By Cross Relaxation Of Nd3+ In LaF3," Phys. Rev. **141**(1966).
82. T. Y. Fan, "Heat-Generation In Nd-YAG And Yb-YAG," IEEE J. Quantum Electron. **29**, 1457-1459 (1993).
83. D. C. Brown, "Heat, Fluorescence, and Stimulated-Emission Power Densities and Fractions in Nd:YAG," IEEE Trans. Quantum Electron. **34**, 560-572 (1998).
84. W. Koechner, "Thermal Lensing In A Nd-YAG Laser Rod," Appl. Opt. **9**(1970).
85. W. Koechner and D. K. Rice, "Effect Of Birefringence On Performance Of Linearly Polarized YAG-Nd Lasers," IEEE J. Quantum Electron. **6**(1970).
86. W. C. Scott and M. deWit, "Birefringence Compensation and TEM_{00} Mode Enhancement in a Nd:YAG Laser," Appl. Phys. Lett. **18**, 3-4 (1971).
87. W. A. Clarkson, "Thermal effects and their mitigation in end-pumped solid-state lasers," J. Phys. D. Appl. Phys. **34**, 2381-2395 (2001).
88. R. Beach, W. J. Benett, B. L. Freitas, D. Mundinger, B. J. Comaskey, R. W. Solarz, and M. A. Emanuel, "Modular Microchannel Cooled Heatsinks For High Average Power Laser Diode-Arrays," IEEE J. Quantum Electron. **28**, 966-976 (1992).
89. M. Tsunekane and T. Taira, "Design and performance of compact heatsink for high-power diode edge-pumped, microchip lasers," IEEE J. Quantum Electron. **13**, 619-625 (2007).
90. R. B. Chesler and D. A. Draegert, "Miniature Diode-Pumped Nd-YAlG Lasers," Appl. Phys. Lett. **23**, 235-236 (1973).

91. J. Stone and C. A. Burrus, "Neodymium-Doped Silica Lasers In End-Pumped Fiber Geometry," Appl. Phys. Lett. **23**, 388-389 (1973).
92. A. E. Siegman, "Bragg diffraction of a Gaussian beam by a crossed-Gaussian volume grating*," JOSA **67**, 545-550 (1977).
93. P. Jelger and F. Laurell, "Efficient narrow-linewidth volume-Bragg-grating-locked Nd:YAG fiber laser," Opt. Express **15**, 11336-11340 (2007).
94. E. Brinkmeyer, W. Brennecke, M. Zurn, and R. Ulrich, "Fiber Bragg Reflector For Mode Selection And Line-Narrowing Of Injection-Lasers," Electron. Lett. **22**, 134-135 (1986).
95. F. Brunet, Y. Taillon, P. Galarneau, and S. LaRochelle, "A Simple Model Describing Both Self-Mode Locking and Sustained Self-Pulsing in Ytterbium-Doped Ring Fibre Lasers," J. Lightwave Technol. **23**, 2131-2137 (2005).
96. M. Dinand and C. H. Schütte, "Theoretical modelling of relaxation oscillations in Er-doped waveguide lasers.," J. Lightwave Technol. **12**, 14-23 (1995).
97. F. Fontana, M. Begotti, E. M. Pessina, and L. A. Lugiato, "Maxwell-Bloch Modelocking Instabilities in Erbium-Doped Fibre Lasers," Opt. Comm. **114**, 89-94 (1995).
98. W. Guan and J. R. Marciante, "Suppression of Self-Pulsations in Dual-Clad, Ytterbium-Doped Fiber Lasers," in *OSA / CLEO/QELS*, 2008),
99. P. Leboudec, P. L. Francois, E. Delevaque, J. F. Bayon, F. Sanchez, and G. M. Stephan, "Influence of Ion-Pairs on the Dynamical Behaviour of Er-3+-doped Fiber Lasers," Opt. and Quantum Electron. **25**, 501-507 (1993).
100. W. H. Loh and J. P. deSandro, "Suppression of self-pulsing behaviour in erbium-doped fiber lasers with resonant pumping: Experimental results," Opt. Lett. **21**, 1475-1477 (1996).
101. L. G. Luo and P. L. Chu, "Suppression of self-pulsing in an erbium-doped fiber laser," Opt. Lett. **22**, 1174-1176 (1997).
102. S. D. Jackson, "Direct evidence for laser reabsorption as initial cause for self-pulsing in three-level fibre lasers," Electron. Lett. **38**, 1640-1642 (2002).

103. Y. Mizrahi, D. J. Digiovanni, R. M. Atkins, S. G. Grubb, Y. K. Park, and J. M. P. Delavaux, "Stable Single-Mode Erbium Fiber-Grating Laser for Digital Communication," J. Lightwave Technol. **11**, 2021-2025 (1993).

104. H. Chen, G. Zhu, N. K. Dutta, and K. Dreyer, "Suppression of self-pulsing behavior in erbium-doped fiber lasers," Appl. Opt. **41**, 3511-3516 (2002).

105. A. Hideur, T. Chartier, C. Özkul, and F. Sanchez, "Dynamics and stabilization of a high power side-pumped Yb-doped double-clad fiber laser," Opt. Comm. **186**, 311-317 (2000).

106. A. C. Boccara, D. Fournier, W. Jackson, and N. M. Amer, "Sensitive photothermal deflection technique for measuring absorption in optically thin media: erratum," Opt. Lett. **6**, 51 (1981).

107. L. C. Aamodt and J. C. Murphy, "Photothermal measurements using a localized excitation source," J. Appl. Phys. **52**, 4903-4914 (1981).

108. W. B. Jackson, N. M. Amer, A. C. Boccara, and D. Fournier, "Photothermal Deflection Spectroscopy And Detection," Appl. Opt. **20**, 1333-1344 (1981).

109. G. Suber, M. Bertolotti, C. Sibilia, and A. Ferrari, "Test Measurements Of The Photothermal Deflection Method To Determine The Thermal-Diffusivity Of Solids," Appl. Opt. **27**, 1807-1810 (1988).

110. B. C. Li and R. Gupta, "Simultaneous measurement of absorption coefficient, thermal diffusivity, and flow velocity in a gas jet with pulsed photothermal deflection spectroscopy.," J. App. Phys. **89**, 859-868 (2001).

111. F. Sun, H. J. Baker, A. B. Russell, J. D. Valera, and D. R. Hall, "Pump uniformity and temperature profile measurements in a planar waveguide Nd:YAG laser by a beam deflection method," IEEE J. Quantum Electron. **43**, 669-675 (2007).

112. A. Kurtz and J. Mentel, "The Thermal-Conductivity Of Cl-2 and O-2 In The Dissociation Region Measured By Optical Interferometry. 2. Evaluation Of The Thermal-Conductivity From Interferometric Data," J. Phys. D. Appl. Phys. **17**, 1343-1348 (1984).

113. J. M. Jewell, C. Askins, and I. D. Aggarwal, "Interferometric Method For Concurrent Measurement Of Thermooptic And Thermal-Expansion Coefficients," Appl. Opt. **30**, 3656-3660 (1991).

114. P. C. Peng, H.-Y. Tseng, and S. Chi, "High-Resolution Fiber Bragg Grating Sensor System Using Linear-Cavity Fiber Laser Scheme," Microwave and Opt. Technol. Lett. **34**, 323-325 (2002).

115. L.-Y. Shao, X. Y. Dong, A. P. Zhang, H. Y. Tam, and S. L. He, "High-resolution strain and temperature sensor based on distributed Bragg reflector fiber laser," IEEE Photon. Technol. Lett. **19**, 1598-1600 (2007).

116. J. Mandal, S. Pal, T. Sun, K. T. V. Grattan, A. T. Augousti, and S. A. Wade, "Bragg grating-based fiber-optic laser probe for temperature sensing," IEEE Photon. Technol. Lett. **16**, 218-220 (2004).

117. M. Siebold, S. Bock, U. Schramm, B. Xu, J. L. Doualan, P. Camy, and R. Moncorge, "Yb:CaF_2 a new old laser crystal," Appl. Phys. B **97**, 327-338 (2009).

118. R. Cieslak, J. K. Sahu, and W. A. Clarkson, eds., *Efficient Intracavity Frequency Doubling of an Yb-doped Fiber Laser Using an Internal Resonant Enhancement Cavity*, CLEO (IEEE, San Jose, USA, 2010).

Bibliography – Part 2

119. J. Arlt and M. J. Padgett, "Generation of a beam with a dark focus surrounded by regions of higher intensity: the optical bottle beam," Opt. Lett. **25**, 191-193 (2000).
120. N. B. Simpson, K. Dholakia, L. Allen, and M. J. Padgett, "Mechanical equivalence of spin and orbital angular momentum of light: an optical spanner," Opt. Lett. **22**, 52-54 (1997).
121. D. G. Grier, "A revolution in optical manipulation," Nature **424**, 810-816 (2003).
122. M. Kraus, M. A. Ahmed, A. Michalowski, A. Voss, R. Weber, and T. Graf, "Microdrilling in steel using ultrashort pulsed laser beams with radial and azimuthal polarization," Opt. Express **18**(2010).
123. S. Franke-Arnold, L. Allen, and M. J. Padgett, "Advances in optical angular momentum," Laser & Photonics Rev. **2**, 299-313 (2008).
124. C. S. Adams and E. Riis, "Laser cooling and trapping of netural atoms," Prog. Quantum Electron. **21**, 1-79 (1997).
125. C. Tamm and C. O. Weiss, "Bistability And Optical Switching Of Spatial Patterns In A Laser," JOSA B **7**, 1034-1038 (1990).
126. E. Abramochkin and V. Volostnikov, "Beam Transformations And Nontransformed Beams," Opt. Comm. **83**, 123-135 (Opt. Comm.).
127. L. Allen, M. W. Beijersbergen, J. C. Spreeuw, and J. P. Woerdman, "Orbital Angular-Momentum Of Light And The Transformation Of Laguerre-Gaussian Laser Modes," Phys. Rev. A **45**, 8185-8189 (1992).
128. M. W. Beijersbergen, L. Allen, H. VanDerVeen, and J. P. Woerdman, "Astigmatic Laser Mode Converters And Transfer Of Orbital Angular-Momentum," Opt. Comm. **96**, 123-132 (1993).
129. M. W. Beijersbergen, R. P. C. Coerwinkel, M. Kristensen, and J. P. Woerdman, "Helical-Wave-Front Laser-Beams Produced With A Spiral Phaseplate," Opt. Comm. **112**, 321-327 (1994).

130. G. A. Turnbull, D. A. Robertson, G. M. Smith, L. Allen, and M. J. Padgett, "Generation of free-space Laguerre-Gaussian modes at millimetre-wave frequencies by use of a spiral phaseplate," Opt. Comm. **127**, 183-188 (1996).

131. N. Zhang, J. A. Davis, I. Moreno, D. M. Cottrell, and X. C. Yuan, "Analysis of multilevel spiral phase plates using a Dammann vortex sensing grating," Opt. Express **18**, 25987-25992 (2010).

132. N. R. Heckenberg, R. McDuff, C. P. Smith, and A. G. White, "Generation Of Optical-Phase Singularities By Computer-Generated Holograms," Opt. Lett. **17**, 221-223 (1992).

133. M. Harris, C. A. Hill, P. R. Tapster, and J. M. Vaughan, "Laser modes with helical wave fronts," Phys. Rev. A **49**(1994).

134. J. F. Bisson, Y. Senatsky, and K. I. Ueda, "Generation of Laguerre-Gaussian modes in Nd:YAG laser using diffractive optical pumping," Laser Phys. Lett. **2**, 327-333 (2005).

135. V. Peet, "Bixial crystal as a versatile mode converter," J. Opt. **12**(2010).

136. A. Ito, Y. Kozawa, and S. Sato, "Generation of hollow scalar and vector beams using a spot-defect mirror," JOSA A **27**, 2072-2077 (2010).

137. L. Allen and M. J. Padgett, "The Poynting vector in Laguerre-Gaussian beams and the interpretation or their angular momentum density," Opt. Comm. **184**, 67-71 (2000).

138. M. J. Padgett, J. Courtial, and L. Allen, "Light's orbital angular momentum," Phys. Today **57**, 35-40 (2004).

139. F. Pampaloni and J. Enderlein, "Gaussian, Hermite-Gaussian, and Laguerre-Gaussian beams: a primer," in *Am. J. Physics*, (2004).

140. D. C. Hanna, "Astigmatic Gaussian Beams Produced By Axially Symmetric Laser Cavities," IEEE J. Quantum Electron. **5**, 483 (1969).

141. Y. Senatsky, J. F. Bisson, A. Shelobolin, A. Shirakawa, and K. Ueda, "Circular modes selectrion in Yb:YAG laser using an intracavity lens with spherical abberation," Laser Phys. **19**, 911-918 (2009).

142. J. W. Kim, J. I. Mackenzie, and W. A. Clarkson, "Influence of energy-transfer-upconversion on threshold pump power in quasi-three-level solid-state lasers," Opt. Express **17**, 11935-11943 (2009).

143. J. Leach and M. J. Padgett, "Observation of chromatic effects near a white-light vortex," New J. Phys. **5**(2003).